Feedback Cooling of Degenerate Quantum Gases

Kaiwen (Kevin) Zhu

A thesis submitted for the degree of
Bachelor of Science with Honours in Physics of
The Australian National University

October, 2023

Declaration

The research presented in this thesis has been completed on the lands of the Ngunnawal and Ngambri people, the traditional owners of the land of the ANU. I acknowledge that this land was stolen and sovereignty was never ceded, and pay my respects to the elders past, present, and emerging. It always was, and always will be, Aboriginal land.

This thesis is an account of research undertaken between February 2023 and October 2023 at the Department of Quantum Science, Research School of Physics, The Australian National University, Canberra, Australia.

Except where acknowledged in the customary manner, the material presented in this thesis is, to the best of my knowledge, original and has not been submitted in whole or part for a degree in any university.

Kaiwen (Kevin) Zhu
October, 2023

Acknowledgments

I have been patiently waiting to write my acknowledgments for the entire of this year. Now I need to write it before the excitement goes away, and I suppose also before I flap away.

For the parents

The concepts of backaction and complimentarity transcend far beyond the realm of quantum measurement theory. Simon is perhaps the best sample of this. Your patience for both repetitively explaining physics to me, as well as dealing with my many indescribable problem (often also at late hours of the night) is appreciated. Though I would never admit this to your face, I could not have asked for a ~~better~~ more suitable supervisor, and I look forward to you being stuck with me for at least another three years. Of course, you are not all quacks and meows. The backaction you caused me has been intense, in both the sense that I could not have foreseen how absolutely cursed you are, and also the numerous table-tennis balls you have whacked into me.

Every Bert needs his Ernie. For Slimey, this Ernie is Joe. Your seemingly endless range of interests and knowledge is inspiring, even for someone of your age. When asked about my supervisors, I always reply that my ultimate goal is to become the amalgamation of you and Slimey. I apologise for the many times I have accidentally called you not smart, not handsome, or old, and appreciate the amount of time you have been willing to invest in me, even at late hours of the night when you are cozy in bed in an oodie. My honours experience would not have been the same without your often helpful, sometimes rabbit-hole inducing involvement, and I intend on continuing to pursue my goal during a PhD (pronounced 'puh-tch-d'). See in you in Torn, anomalousman.

For my siblings and estranged relatives

Zain, one day I shall be able to pronounce your name properly. Your return and presence during the second half of the year was a blessing from Joe Pope, and I can safely say I would not have achieved as much as I did if it weren't for constant incursions next door. Also, I appreciate the fact that we bonded over our mutual *redacted*.

To Yosri, my love, my world, my sweetie pumpkin pie. Thank you for keeping me company and checking up on me at early hours of the morning, especially near the completion of this thesis. Your loud grunts and lucious locks provided me tremendous enjoyment, and I genuinely appreciate your continued care for me. As promised, I will write your papers for you such that you may graduate. Love you buddy! (Also, love you too Hui!)

Moving on to my estranged relatives: Giri, I appreciate the brief but many exchanges we have everytime we run into each other, and am glad that we both have lots of love for Wigner. Reuben, thanks for the ~~slightly incorrect~~ QND derivations. Rhys, Ryan ginger, and Jordan ginger, thanks for the mutual bullying of Yosri and the occasional game of pong. Sam (not ginger), knowing that you also share my love of drinking plain milk and eating buttered toast fills me with hope. And also Josh, thanks for visiting me at random times I suppose. The quantum quackles (No. 1 and No. 4). Your company in semester two served as an excellent replacement for the company of other honours students, and I look forward to further shenanigans next year.

Ozlem, I know I always call you a hater, but deep down, I know you do not actually hate me. Thanks for the muffins you always bring me, and our mutual bullying of Yosri. Dige, Chenyue, thank you for being excellent 学姐 Siobhan, Belinda, and Petra of the south: Thank you for being such incredible admin staff: Physics (north would completely collapse without the magic you all work.

Compatriots (those who fed me)

Though I was abandoned by all the honours students, a few of you came and visited me. Thank you to my first husband Rob, for the all the times you fed me and the absolutely bizzare memes and messages you would send at ungodly hours. My sugardaddy Tony, thank you for feeding me and providing me with red bull. Most importantly, thank you for your company in thesis writing. Neither of our theses would probably have been completed otherwise. Sherry and Josh, thanks for your occasional visits, memes, and laughs.

The Quackles

I think this justifies a subsection of its own. SORRY PLANE TAKING OFF HAVE TO SUBMIT NOW.

最后，我得感谢我的外婆。阿婆，你一身对我的爱，关心，尽力，我都体会着呢。我知道其实我不需要说太多。如果没有内，我的一身不可能有现在。我爱你。

Abstract

In recent years, the field of ultra-cold atomic gases has rapidly evolved into a cornerstone of experimental quantum mechanics, with promising applications in precision sensing, quantum computing, and as platforms for tests of fundamental physics. Currently, ultra-cold quantum gases are prepared via the two-step process of laser and evaporative cooling. However, the latter an inherently lossy process, resulting in the lost of almost all (99.9%) of the initial atoms. Recently, advances in optical control technology have lead to considerable interest in an alternative, number-conserving procedure based upon principles of feedback cooling [1]. Previous attempts to model feedback cooling of atomic gases have struggled to capture the complex quantum correlations induced by the measurement process, as well as finite temperature effects associated with thermal fluctuations. To this end, the applicability of feedback cooling to complex, multi-mode systems such as quantum gases is still an open question. In this thesis, a new field-theoretic technique based upon existing phase-space methods is developed for scalable numerical simulations of controlled quantum systems, and used to model feedback cooling of a Bose gas subject to periodic, non-destructive measurements via phase-contrast imaging. We check the validity of our approach in a two-mode system, which permits an exact solution due to its low-dimensional nature, and observe exceptional agreement across various moments of pseudo-spin operators. In addition, we discuss potential limitations of our approach, and propose comparisons with existing techniques such as the Number-Phase Wigner particle filter, which has been the leading choice for existing simulations of controlled quantum systems [2] undergoing number-like measurements. Finally, we present preliminary results demonstrating successful cooling of a thermal state with low condensate fraction in a quasi-1D geometry, where we observe an increase of the condensate fraction from $f_{\text{frac}} = 4.4 \pm 0.2\%$ to $f_{\text{frac}} = 98.0 \pm 0.2\%$ over forty trap periods. To our knowledge, this is the first demonstration of successful cooling for a finite-temperature quantum field with particle numbers on the order of $N \approx 10^6$ and low initial condensate fraction. We conclude with a discussion of the restrictions imposed by the dimensional reduction, and propose avenues for further investigations such as the incorporation of spontaneous emission effects, exotic feedback schemes, and simulation of experimentally realistic geometries.

Contents

List of Figures

Chapter 1

Introduction

First predicted by Satyendra Bose and Einstein in 1924, experimental realisation of the first Bose-Einstein Condensate (BEC) 71 years later by Cornell *et al.* marked the dawn of a new era for experimental quantum mechanics [3, 4]. As a macroscopic[1] occupation of the quantum mechanical ground-state, their ability to exhibit phenomena such as quantum superposition and entanglement, have lead to growing interest in fields such as quantum metrology and precision sensing [5, 6], non-equilibrium many-body dynamics [7], as well as proposals for tests of fundamental physical theories such as semi-classical and quantum gravity [8].

Current methods used in the preparation of BECs discard almost all atoms in the original ensemble. Feedback cooling has been proposed as an alternative, and is in principle number conserving. However, previous attempts to model feedback cooling of atomic gases have struggled to capture the complex quantum correlations induced by the measurement process, as well as finite temperature effects associated with thermal fluctuations [2, 9, 10]. To this end, the efficacy of feedback cooling to complex, multi-mode systems such as quantum gases is still an open question. It is the goal of this thesis to develop and test a new simulation technique capable of capturing the complexities above when scaled to multi-mode systems with large particle numbers.

The structure of this introduction is as follows: In Section 1.1, we introduce the key properties of ultra-cold atoms and BECs, with a focus on experimentally relevant thermodynamic quantities. In Section 1.2, we review evaporative cooling, which is currently the standard procedure for preparation of BECs. Subsequently, we introduce the concept of feedback control and cooling, which is the alternative method we study in this thesis. Section 1.3 provides a detailed overview on the existing feedback cooling literature, as well as the key difficulties associated with simulating feedback cooling. Finally, Section 1.4 contains a detailed synopsis of the structure of this thesis, as well as the key objectives of each chapter.

[1] As a rough rule of thumb, 'macroscopic' has historically referred to objects observable to the naked eye, hundreds of microns ($\sim 100\ \mu$m).

1.1 A Macroscopic Platform for Quantum Phenomena: BECs

A Bose-Einstein Condensate (BEC) is a macroscopic population of the quantum mechanical ground state, existing only below a critical condensation temperature (T_c). Let us consider the case of a Bose gas trapped in a harmonic potential of the form:

$$V_{\text{trap}}(\boldsymbol{x}) = \frac{1}{2}m(\omega_x^2 x^2 + \omega_y^2 y^2 + \omega_z^2 z^2) \tag{1.1}$$

In the thermodynamic limit, where the volume of the system is taken to infinity[2] assuming fixed particle number density, the critical temperature may be expressed as [11]:

$$T_c \approx \frac{\hbar\bar{\omega}}{k_b}\left(\frac{N}{\zeta(3)}\right)^{\frac{1}{3}} \tag{1.2}$$

where N denotes the total particle number of the system, $\bar{\omega} = (\omega_x\omega_y\omega_z)^{1/3}$ is the geometric mean of the trapping frequencies, k_b is the Boltzmann constant, and ζ is the Riemann zeta function. The critical temperature is also the temperature for which the thermal de Broglie wavelength of the atomic gas is roughly equal to the average inter-particle spacing. For perspective, typical transition temperatures for an ensemble of $N \approx 10^6$ ^{87}Rb atoms are of the order of $\mathcal{O}(100\ nK)$[12]. Below the critical temperature, the atoms start to condense and begin to macroscopically populate the ground state, where the number of condensed atoms (N_0) is given by the following expression [12]:

$$\frac{N_0}{N} = 1 - \left(\frac{T}{T_c}\right)^3 \tag{1.3}$$

One can also define a *condensate fraction* as $f_{\text{frac}} = N_0/N$. Importantly, the transition between zero and a finite condensate fraction is only discontinuous in the thermodynamic limit. In reality, the phase transition is always smooth due to finite size effects.

1.2 The Production of Ultra-Cold Atoms

1.2.1 Standard Procedure: Evaporative Cooling

Remarkably, the production of BECs has remained virtually unchanged since its inception 28 years ago: A two-stage process of laser and evaporative cooling [13, 14]. In the latter process, the confining potential is reduced to allow energetic atoms to escape, while the remaining atoms rethermalise to a lower average temperature [15]. Evaporative cooling is essential in order to reduce the temperature below the critical formation temperature[3] ($T_c \sim 100$ nK) of BECs [12, 16]. However, it also leads to the loss of almost *all* (99.9%) initial atoms, while the final atomic density (size of the BEC) is further constrained by collisional loss processes which compete with the rethermalisaton rate [15]. Combined, these limitations pose an upper bound on the achievable atom number ($\sim 10^7$) of current BECs [17].

Larger BECs are desirable for a multitude of reasons: They allow us to study a wider range of physics, such as superconductivity and other collective phenomena which would not be

[2] This corresponds to the limit where the trapping frequencies limit to zero.

[3] The specific critical temperature is geometry and species dependent, though almost always in the micro-Kelvin range.

possible with smaller ensembles [18]. In atomic interferometers used for inertial sensing, the achievable precision scales inversely with particle number[4]. Hence, we are motivated to look for an alternative cooling procedure that is both number conserving and scalable to greater atom numbers.

1.2.2 Alternative Procedure: Feedback Cooling

The advent of advances in optical control [19, 20] and imaging methods [21, 22] lead to the proposal of an alternative, number-conserving procedure based upon principles of quantum control [23] and feedback cooling, where non-destructive measurements of the quantum system are made in real time and used to drive the state towards a desired state. In the case of feedback cooling, the desired state is the many-body ground state of the trapping potential. In the past, single-ion and opto-mechanical oscillator systems have been successfully cooled to their motional ground states [24, 25]. However, its application to atomic gases remains stagnant, as theoretical investigations have yet to succeed at modeling experimentally realistic geometries.

Feedback cooling is subject to entirely different limitations to those of evaporative cooling: It is not limited by rethermalisation. Rather, the atomic state is unavoidably modified by the measurement process in an undesirable manner. This mechanism is called *measurement backaction*, and in the case of feedback cooling, leads to heating of the atomic gas. Hence, the feasibility of feedback cooling is contingent on the balance between the rate at which feedback is able to extract energy from the system and heating due to measurement backaction.

1.3 An Honest Review of Feedback Cooling Literature

The study of quantum control theory is an extensive field; a comprehensive review is given by Zhang *et al.* in [1]. Here, we provide an overview of the feedback cooling literature specific to multi-mode ultra-cold atomic gases with spatial structure. A timeline is presented in Fig. 1.1 below.

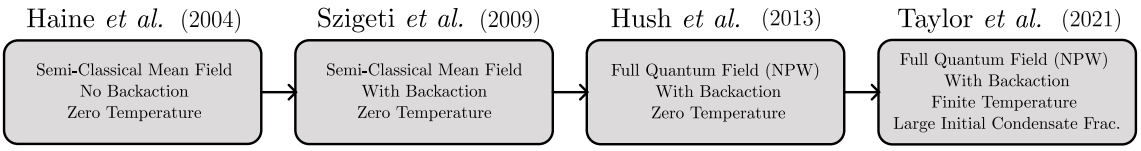

Figure 1.1: A timeline of the feedback cooling literature specific to ultra-cold atomic gases.

The terminology in Fig. 1.1 appear frequently in this thesis, so we start by explicitly defining them:

- A semi-classical approximation refers to any treatment in which quantum correlations arising from entanglement between particles are neglected. Under this approximation, the dynamics of the full quantum field may be reduced to those of a 'mean-field', which has the same dimensionality as a single-particle wavefunction. The topic is further discussed in Section 2.2.1.

[4]The Standard Quantum Limit scales as $\propto N^{-1/2}$, while the Heisenberg limit scales with $\propto N^{-1}$.

- Measurement backaction refers to unwanted changes of the atomic state due to the measurement process. It is a fundamental process which must be included in any realistic description of feedback cooling.
- Atomic gases exist at finite temperature. Hence, they must be described as a thermal mixture represented with a density matrix, rather than a pure state represented by a single ket. We refer to studies which assume the latter as a 'zero-temperature' description, as the assumption is only true at $T = 0$.
- Prior to feedback cooling, atomic ensembles are at thermal equilibrium with temperature $T \gtrsim T_c$, where the fraction of atoms occupying the condensate mode is effectively zero.

The first study of feedback cooling applied to atomic (Bose) gases may be traced back to Haine *et al.* [26], who demonstrated that a time-dependent control potential informed by perfect measurements of atomic density moments was able to drive the atomic ensemble towards its ground state. However, the studies employed a mean-field approximation and neglected the effects of measurement backaction. Subsequent work by Szigeti *et al.* correctly accounted for backaction; however, simulations still employed a mean field approach, and were performed only in the single-particle limit. Hush *et al.* performed the first simulation for a full quantum field using the Number-Phase Wigner (NPW) particle filter [2], and demonstrated that an atomic state initially below the transition temperature could successfully be cooled. Finally, subsequent unpublished work by Taylor *et al.* extended the results of Hush *et al.* to finite temperature mixtures [27]. However, their simulations were limited to temperature regimes in which the thermal mixtures *initially* contained appreciable condensate fraction ($f_{\text{cond}} \approx 0.70$).

In terms of experimental progress, the closest analogue to feedback cooling is the work of Gakdacz *et al.* , who employed measurement based feedback to stabilise number fluctuations in a thermal cloud, enabling the preparation of atomic gases with sub-shot noise number uncertainties [28]. Measurements were made via phase-contrast imaging (PCI): A non-destructive measurement technique which provides an estimate of the atomic density profile. The same method is used in feedback cooling.

1.4 Thesis Goals and Structure

Like those who came before it, the underlying goal of this thesis is to simulate feedback cooling of atomic gases to quantum degeneracy where we expect the the formation of a BEC. In order to avoid the obstacles encountered by previous studies, we first develop a new approach for the simulation of conditioned quantum systems. Roughly speaking, this thesis comprises alternating chapters of theory and results, and may be grouped into two sections: In the first half, we focus on establishing the validity of our approach. In the second half, we apply our method to the pedagogical example of a quasi-1D atomic gas undergoing feedback cooling. A more detailed synopsis is as follows:

In Chapter 2, we introduce the background relevant to this thesis. In particular, we introduce the key concepts of quantum measurement and the phase-space approach to quantum mechanics. The latter provides us with a powerful simulation procedure known as the Truncated Wigner Approximation (TWA), which we extensively use throughout

this thesis. In Chapter 3, we introduce our approach and benchmark it against a direct integration of the Schrodinger equation in a low-dimensional system: A two-mode analogue to feedback cooling. Chapter 4 extends our model of measurement as presented in Chapter 3 to the multi-mode case, where we derive equations describing an atomic gas undergoing phase-contrast imaging. These equations are simulated in Chapter 5, where we present preliminary results of a quasi-1D atomic gas undergoing feedback cooling. We demonstrate successful cooling of a thermal mixture with low initial condensate fraction to a condensed mode. We note that the low initial condensate fraction is an inherent limitation of the 1D geometry, rather than a limitation of our approach. Finally, we discuss avenues for future work in Chapter 6. These include extending our simulations to 2D and 3D geometries which resemble realistic experimental geometries, the effects of spontaneous emission, as well as more exotic feedback schemes which may lead to improved cooling efficiency.

Chapter 2

Background Theory

This chapter introduces most of the technical background encountered in this thesis. In Section 2.1, we start by discussing statistical properties of indistinguishable particles, which naturally motivates the concept of second quantisation. In Section 2.2, we introduce the cold-atom Hamiltonian and discuss its general properties, before deriving the Gross-Pitaevskii Equation (GPE) through the coherent-state approximation. In Section 2.3, we introduce the idea of quantum measurement as entanglement, as well as the notion of weak measurement, both of which are at the very heart of this thesis. Section 2.4 provides an overview of the conditional master equation, which is the starting point of previous studies of feedback cooling. Finally, Section 2.5 introduces the phase-space formulation of quantum mechanics, which opens the door to a wide range of scalable simulation methods heavily employed in this thesis.

2.1 Bosons, Fermions, and Many-Particles

2.1.1 A Boring Necessity: Indistinguishability and Symmetry

In classical mechanics, identical particles are typically distinguishable due to our ability to observe, track, and hence 'label' each particle. This is no longer true in quantum mechanics, where identical particles are treated as indistinguishable. Fundamentally, this is a consequence of identical particles being excitations of the *same* quantum-field [29]. Indistinguishability imposes constraints on the statistical properties of many-particle quantum states. For example, consider the following N-particle state in the position basis:

$$\begin{aligned} |\Psi\rangle = \bigotimes_{n=1}^{N} |\psi\rangle_n = \bigotimes_{n=1}^{N} \left(\int d\boldsymbol{x}_n \, \psi(\boldsymbol{x}_n) \, |\boldsymbol{x}_n\rangle \right) \\ = \int d\boldsymbol{x}_1 \, d\boldsymbol{x}_2 \ldots \boldsymbol{x}_N \, \Psi(\boldsymbol{x}_1, \boldsymbol{x}_2, \ldots, \boldsymbol{x}_N) \, |\boldsymbol{x}_1, \boldsymbol{x}_2, \ldots, \boldsymbol{x}_N\rangle \end{aligned} \tag{2.1}$$

Where the combined many-body state $|\Psi\rangle$ is equal to the tensor product of N identical single-particle states which we denote by $|\psi\rangle$, and has combined wavefunction $\Psi(\boldsymbol{x}_1, \boldsymbol{x}_2, \ldots, \boldsymbol{x}_N)$. As the particles are identical, physical observables must remain invariant under permutation of one (or many) particle (co-ordinates). That is:

$$|\Psi(\ldots, \boldsymbol{x}_j, \boldsymbol{x}_k, \ldots)|^2 = |\Psi(\ldots, \boldsymbol{x}_k, \boldsymbol{x}_j, \ldots)|^2 \tag{2.2}$$

There are only two ways the wavefunction may transform under permutation for which the condition above is satisfied:

$$\Psi(\boldsymbol{x}_j, \boldsymbol{x}_k) = \Psi(\boldsymbol{x}_k, \boldsymbol{x}_j) \qquad \text{or} \qquad \Psi(\boldsymbol{x}_j, \boldsymbol{x}_k) = -\Psi(\boldsymbol{x}_k, \boldsymbol{x}_j) \tag{2.3}$$

Co-ordinates of other particles have been omitted for clarity. Particles that obey the first of Eq. 2.3 are called *Bosons* and are *symmetric* under exchange, while those obeying the latter are *Fermions* and are *anti-symmetric* under exchange[1]. This small difference in sign leads to profoundly different physical behaviours: Consider a two particle state, where each particle may occupy one of two modes, which we denote $|a\rangle$ and $|b\rangle$. Now consider a general superposition where both particles occupy the same state:

$$|\Psi\rangle = \frac{1}{\sqrt{2}}(|a\rangle_1 |a\rangle_2 + |b\rangle_1 |b\rangle_2) \tag{2.4}$$

Roman subscript denotes the particle number. As the particles are identical, swapping the particles leaves the quantum state unchanged. Per Eq. 2.3, however, this may only be true for bosons and not for fermions[2], so we conclude that two identical fermions may not simultaneously occupy the same quantum state. This is the famous *Pauli Exclusion Principle* [30], and is responsible for phenomena such as degeneracy pressure in neutron stars [31] and superconductivity in cuprates [32]. On the other hand, bosons occupying the same mode leads to the phenomenon of Bose-Einstein Condensation [33], the production of which is the focus of this thesis.

These properties are also apparent from statistical distributions of both types of particles, which may be derived simply from thermodynamic arguments of allowed occupation numbers of different microstates. A derivation may be found in [31]. The upshot is that the mean occupancy for Bosons and Fermions follow Bose-Einstein and Fermi-Dirac distributions, respectively:

$$\overline{n}_i^B = \frac{1}{e^{(\epsilon_i - \mu)/k_b T} - 1} \qquad\qquad \overline{n}_i^F = \frac{1}{e^{(\epsilon_i - \mu)/k_b T} + 1} \tag{2.5}$$

In the above, $\overline{n}_i$ and ϵ_i are the mean occupation and energies of the i'th energy level, T is the temperature, and μ is the chemical potential of the system.

[1] Note this generalises to permutations of the entire quantum state of identical particles.

[2] The only way for a fermionic wavefunction remain unchanged under particle exchange is if it is zero everywhere, but this is just vacuum.

2.1.2 Second Quantisation and Many Body Operators

The symmetry condition of Eq. 2.3 must be satisfied for all many-body quantum states. For example, consider a three-particle state, where each particle occupies a different mode, and swap two of the particles. The following is *not* a valid bosonic many-body state:

$$|\Psi\rangle = |a\rangle_1 |b\rangle_2 |c\rangle_3 \qquad \neq \qquad |\Psi'\rangle = |a\rangle_2 |b\rangle_1 |c\rangle_3 \tag{2.6}$$

As the state $|\Psi'\rangle \neq |\Psi\rangle$. In order to satisfy the symmeterisation condition, we may only have the superposition:

$$|\Psi\rangle = \frac{1}{\sqrt{6}}(|a\rangle_1 |b\rangle_2 |c\rangle_3 + |a\rangle_2 |b\rangle_1 |c\rangle_3 + \ldots + |a\rangle_3 |b\rangle_2 |c\rangle_1) \tag{2.7}$$

All many-body wavefunctions must be symmetrised in an analogous way, which quickly leads to tedious coefficients and normalisation factors for multi-mode systems containing large numbers of particles [34]. As we work with identical particles, we generally do not care about the behaviour of specific individual particles: The collective dynamics such as the number of particles occupying a specific mode is far more important. This motivates the concept of *second quantisation*, where only the particle number distribution across different modes are specified, removing the redundancy associated with keeping track of individual identical particles.

A state can only be represented in second quantisation after the underlying *single-particle basis* is specified. For example, let us consider the eigenstates of the harmonic oscillator potential in the *position* basis. These are known as the Hermite-Gauss (HG) functions, and form a complete orthonormal basis. For a system with N-particles, we may express the many-body state as:

$$|\Psi\rangle = |n_0, n_1, \ldots, n_k, \ldots\rangle \qquad \text{where} \qquad \sum_{i=0} n_i = N \tag{2.8}$$

Here, each n_k denotes the number of particles in the k'th HG mode $\phi_k(x)$, which may be expressed as:

$$\phi_k(x) = \frac{1}{\sqrt{2^k k!}} \pi^{-1/4} \exp\left(-x^2/2\right) H_k(x), \qquad \int dx\, \phi_j^*(x)\phi_k(x) = \delta_{jk} \tag{2.9}$$

where $H_k(x)$ is the k'th Hermite polynomial. Importantly, the distribution of particles in each mode would change if we chose a different single-particle basis: The eigenfunctions[3] in k-space, for example. The underlying algebraic space for second quantisation is the *Fock space*. For a bosonic system which comprises a *finite* number (N) of identical particles, it is described as the symmetrised tensor product of N copies of the single-particle Hilbert space ($\mathcal{H}$). For a system with *indefinite* particle number, the Fock space generalises in the expected way, as the direct sum of Fock spaces with (different) definite particle numbers:

$$\mathcal{F}^N(\mathcal{H}) = \mathcal{S}\left(\bigotimes_{n=0}^{N} \mathcal{H}\right), \qquad \mathcal{F}(\mathcal{H}) = \bigotimes_{m=0}^{\infty} \mathcal{F}^m(\mathcal{H}) \tag{2.10}$$

[3] In this case, this is arguably not the best example, as the (position) space HG modes are eigenfunctions of the Fourier transform, i.e $\tilde{\phi}_j(k) = \mathcal{F}\{\phi_j(x)\} = (-i)^k \phi_j(k)$.

Where $\mathcal{S}$ denotes the symmeterisation operator [34]. A convenient basis choice for the Fock space is that of the Fock states, which are the many-body states with definite particle number. Multi-mode Fock states generalise in the expected way; as the tensor product of single-mode Fock states in each mode. In order to work in the Fock space, we must first transform single-particle operators into their many-body analogue. We will not show it here, but it is generally true that all single-particle operators may equivalently be expressed as strings of annihilation and creation operators. These are defined by their action on the Fock states, annihilating or creating particles in different modes:

$$\begin{aligned}\hat{a}_j^\dagger \left|n_0,\ldots,n_j,\ldots\right\rangle &= \sqrt{n_j+1}\left|n_0,\ldots,n_j+1,\ldots\right\rangle \\ \hat{a}_j \left|n_0,\ldots,n_j,\ldots\right\rangle &= \sqrt{n_j}\left|n_0,\ldots,n_j-1,\ldots\right\rangle\end{aligned} \tag{2.11}$$

Here, $\hat{a}_j^\dagger$ and $\hat{a}_j$ are the creation and annihilation operators corresponding to the j'th mode, respectively. They obey the standard bosonic commutation relations:

$$\left[\hat{a}_j, \hat{a}_k^\dagger\right] = \delta_{jk}, \qquad \left[\hat{a}_j, \hat{a}_k\right] = \left[\hat{a}_j^\dagger, \hat{a}_k^\dagger\right] = 0 \tag{2.12}$$

Without going into lines of algebra, the claim above may be intuitively verified by considering the action of an arbitrary single-particle operator on a quantum state as an operation which changes the state of the system. For example, consider the translation operator acting on a single-particle position eigenstate:

$$\hat{T}(\boldsymbol{x}_0)\left|\boldsymbol{x}\right\rangle = \left|\boldsymbol{x}+\boldsymbol{x}_0\right\rangle, \qquad \text{where} \quad \hat{T}(\boldsymbol{x}_0) = \exp\left(-\frac{i}{\hbar}\boldsymbol{x}_0\cdot\hat{\boldsymbol{p}}\right) \tag{2.13}$$

Clearly, the particle has gone from the mode $\left|\boldsymbol{x}\right\rangle \to \left|\boldsymbol{x}+\boldsymbol{x}_0\right\rangle$. This is equivalent to the annihilation of a particle in $\left|\boldsymbol{x}\right\rangle$ immediately followed by the creation of a particle in $\left|\boldsymbol{x}+\boldsymbol{x}_0\right\rangle$. The logic generalises to all operators, and may be succinctly expressed in the following way:

$$\sum_p^N \left|\phi_j\right\rangle_{pp}\left\langle\phi_k\right| \equiv \hat{a}_j^\dagger \hat{a}_k \tag{2.14}$$

where the p sums over a discrete particle number index. For a rigorous proof, we refer the reader to [34].

2.1.3 Second Quantisation in a Continuous Basis: Field Operators

Analogous to how $\hat{a}_j^\dagger$ and $\hat{a}_j$ are creation and annihilation operators for the j'th mode ($|\phi_j\rangle$), their generalisation to a continuous basis takes the form of field operators $\hat{\psi}^\dagger(\boldsymbol{x})$ and $\hat{\psi}(\boldsymbol{x})$ which create and annihilate particles at the spatial mode $\boldsymbol{x}$. They are expressed as a sum over the discrete operators:

$$\hat{\psi}(\boldsymbol{x}) = \sum_{j=0}^{\infty} \langle \boldsymbol{x}|\phi_j\rangle\, \hat{a}_j = \sum_{j=0}^{\infty} \phi_j^*(\boldsymbol{x})\hat{a}_j, \qquad \hat{\psi}^\dagger(\boldsymbol{x}) = \sum_{j=0}^{\infty} \langle \phi_j|\boldsymbol{x}\rangle\, \hat{a}_j^\dagger = \sum_{j=0}^{\infty} \phi_j(\boldsymbol{x})\hat{a}_j^\dagger \tag{2.15}$$

The Heisenberg equations of motion for the field operators furnish a complete description for the dynamics of the quantum field. They obey similar commutation relations:

$$\left[\hat{\psi}(\boldsymbol{x}), \hat{\psi}^\dagger(\boldsymbol{x}')\right] = \delta^3(\boldsymbol{x}-\boldsymbol{x}'), \quad \left[\hat{\psi}(\boldsymbol{x}), \hat{\psi}(\boldsymbol{x}')\right] = \left[\hat{\psi}^\dagger(\boldsymbol{x}), \hat{\psi}^\dagger(\boldsymbol{x}')\right] = 0 \tag{2.16}$$

Of course, the field operators may also carry additional discrete indices referring to internal degrees of freedom. For example, in Chapter 4, we encounter separate field operators for the ground and excited states of an atomic field. Single-mode operators may be recovered by projecting the field operator onto the basis functions of each mode, and integrating over the entire spatial extent:

$$\hat{a}_j = \int d\boldsymbol{x}\; \phi_j(\boldsymbol{x})\hat{\psi}(\boldsymbol{x}), \qquad \hat{a}_j^\dagger = \int d\boldsymbol{x}\; \phi_j^*(\boldsymbol{x})\hat{\psi}^\dagger(\boldsymbol{x}) \tag{2.17}$$

Just as annihilation and creation operators for different single particle bases $\{|\phi_k\rangle\}$ and $\{|\psi_j\rangle\}$ are related by the standard change of basis transformation:

$$\hat{a}_j = \sum_{k=1}^{\infty} \langle \phi_k|\psi_j\rangle\, \hat{a}_k, \qquad \hat{a}_j^\dagger = \sum_{k=1}^{\infty} \langle \psi_j|\phi_k\rangle\, \hat{a}_k^\dagger \tag{2.18}$$

Field operators are mapped between different continuous bases using the relevant Fourier transforms:

$$\hat{\psi}(\boldsymbol{k}) = \frac{1}{(2\pi)^{3/2}} \int d^3\boldsymbol{x}\; \hat{\psi}(\boldsymbol{x}) e^{-i\boldsymbol{k}\cdot\boldsymbol{x}}, \qquad \hat{\psi}(\boldsymbol{x}) = \frac{1}{(2\pi)^{3/2}} \int d^3\boldsymbol{k}\; \hat{\psi}(\boldsymbol{k}) e^{i\boldsymbol{k}\cdot\boldsymbol{x}} \tag{2.19}$$

We conclude this section with a useful trick: Many-body generalisations of operators which act on single-particle position space wavefunctions may be obtained in the following way:

$$h(\boldsymbol{x}, \Lambda) \to \hat{h}_{\text{many-body}} = \int d^3\boldsymbol{x}\; \hat{\psi}^\dagger(\boldsymbol{x}) h(\boldsymbol{x}, \Lambda)\hat{\psi}(\boldsymbol{x}) \tag{2.20}$$

Where we have used Λ to denote functional operators which act on the wavefunction. We will see an application Eq. 2.20 in the following section, where we introduce the cold-atom Hamiltonian.

2.2 The Cold-Atom Hamiltonian

We now introduce the Cold-Atom Hamiltonian which generates almost all the dynamics investigated in this thesis:

$$\hat{H}_{\text{CA}} = \int d^3\boldsymbol{x}\ \hat{\psi}^\dagger(\boldsymbol{x}) h(\boldsymbol{x}) \hat{\psi}(\boldsymbol{x}) + \frac{g}{2} \int d^3\boldsymbol{x}\ \hat{\psi}^\dagger(\boldsymbol{x}) \hat{\psi}^\dagger(\boldsymbol{x}) \hat{\psi}(\boldsymbol{x}) \hat{\psi}(\boldsymbol{x}) \tag{2.21}$$

where we we refer to the following as the single-particle Hamiltonian:

$$h(\boldsymbol{x}) = -\frac{1}{2}\boldsymbol{\nabla}^2 + \frac{1}{2}\boldsymbol{x}^2 + V_{\text{fb}}(\boldsymbol{x}, t) \tag{2.22}$$

The first term contains the contribution from the kinetic and potential energies for a particle trapped in a harmonic potential, as well as an arbitrary time-dependent control potential ($V_{\text{fb}}(\boldsymbol{x}, t)$), through which we implement feedback. We have adopted harmonic oscillator units, where dimensions of length are scaled by $x_0^i = \sqrt{\hbar\omega_i/m}$, time by $1/\omega_i$, and energies by $\hbar\omega_i$, where m and ω_i are the atomic mass and trapping frequency along different dimensions, respectively[4].

The second term in Eq. 2.21 describes repulsive interactions between pairwise atoms through s-wave scattering events. This is a valid approximation to the true interaction potential in the limit that the mean inter-particle separation within the gas is significantly greater than the s-wave scattering length (α_s) [12]. In this case, the two-body interactions are perfectly elastic and local and may be described by a contact potential. The dimensionless interaction strength (g) is proportional to the scattering length, and given by:

$$g = \frac{4\pi\alpha_s}{\alpha_0} \tag{2.23}$$

where α_0 is the Bohr radius. The scattering length is a species dependent parameter. For alkali atoms, its typical value lies between $\alpha_s \approx 10\alpha_0 - 100\alpha_0$ [35]. Experimentally, the scattering length may be further adjusted through magnetic fields utilising Fano-Feshbach resonances. As such, we will consider g as a tunable parameter.

In practice, the interaction strength is also dependent on the atomic density. This is easily seen by applying the commutation relations of Eq. 2.16 to the interaction term of Eq. 2.21, whereby it may written as:

$$\hat{H}_{\text{int}} = \frac{g}{2} \int d^3\boldsymbol{x}\ \hat{n}(\boldsymbol{x})(\hat{n}(\boldsymbol{x}) - 1) \tag{2.24}$$

where $\hat{n}(\boldsymbol{x}) = \hat{\psi}^\dagger(\boldsymbol{x})\hat{\psi}(\boldsymbol{x})$ is the atomic density. As the kinetic and potential terms are proportional to $\hat{n}(\boldsymbol{x})$ as opposed to $\hat{n}(\boldsymbol{x})^2$, the dynamics generated by the interaction terms dominate in regions of large atomic density.

[4] ω_i is typically anisotropic. In which case, one may define an average length scale, $\tilde{x} = (x_0^x x_0^y x_0^z)^{1/3}$. For our purposes, we only perform one-dimensional simulations, so x_0 automatically refers to the trapping frequency along this dimension.

2.2.1 Mean-Field Theory

In theory, computing Heisenberg's equation of motion for the field operator ($\hat{\psi}(\boldsymbol{x})$) under the cold-atom Hamiltonian (Eq. 2.21) produces exact dynamics for the full quantum field. However, full quantum field simulations are numerically intractable due to exponential scaling of the Hilbert space with particle number. Hence, we often seek approximations which reduce the dimensionality of the problem to tractable levels. A common approach is *mean-field* theory, where the equation of motion for the full quantum field is reduced to an equation for an *order-parameter*, an object with the same dimensionality as that of a single-particle wavefunction. Denoting the order-parameter as $\phi(\boldsymbol{x})$, its equation of motion is known as the Gross-Pitaevskii Equation (GPE) [36] or Non-Linear Schrodinger equation (NLSE):

$$\partial_t \phi(\boldsymbol{x}) = -i\Big(h(\boldsymbol{x})\phi(\boldsymbol{x}) + g|\phi(\boldsymbol{x})|^2\phi(\boldsymbol{x})\Big) \tag{2.25}$$

It was first written down by Gross and Pitaevskii in the study of atomic vortices, and may be derived by assuming a particular ansatz for the quantum state. We provide a brief derivation here assuming the coherent state approximation. That is, we write the state as the tensor product of a coherent state in each spatial mode with amplitude given by the order parameter:

$$|\Psi\rangle = \bigotimes_{\boldsymbol{x}} |\phi(\boldsymbol{x})\rangle \qquad \text{such that} \qquad \hat{\psi}(\boldsymbol{x})\,|\Psi\rangle = \phi(\boldsymbol{x})\,|\Psi\rangle \tag{2.26}$$

Expectation values are easy to compute under this form. Consider the most general operator:

$$\hat{O} = \int d\boldsymbol{x}\ (\hat{\psi}^\dagger(\boldsymbol{x}))^m h(\boldsymbol{x},\Lambda)(\hat{\psi}(\boldsymbol{x}))^n \tag{2.27}$$

Using the eigenstate property of Eq. 2.26, we find:

$$\langle\hat{O}\rangle = \langle\Psi|(\hat{\psi}^\dagger(\boldsymbol{x}))^m h(\boldsymbol{x},\Lambda)(\hat{\psi}(\boldsymbol{x}))^n|\Psi\rangle = \int d\boldsymbol{x}\ (\phi^*(\boldsymbol{x}))^m h(\boldsymbol{x},\Lambda)(\phi(\boldsymbol{x}))^n$$

We use the above to compute the evolution of $\langle\hat{\psi}(\boldsymbol{x})\rangle$ from Heisenberg's equation of motion:

$$\begin{aligned}
\partial_t \langle\hat{\psi}(\boldsymbol{x})\rangle &= i\left\langle\left[\hat{H},\hat{\psi}(\boldsymbol{x})\right]\right\rangle \\
&= i\left\langle\int d\boldsymbol{x}'\ \hat{\psi}^\dagger(\boldsymbol{x}')h(\boldsymbol{x})\left[\hat{\psi}(\boldsymbol{x}'),\hat{\psi}(\boldsymbol{x})\right] + \left[\hat{\psi}^\dagger(\boldsymbol{x}'),\hat{\psi}(\boldsymbol{x})\right]h(\boldsymbol{x})\hat{\psi}(\boldsymbol{x}')\right\rangle \\
&+ \frac{ig}{2}\Bigg[\left\langle\int d\boldsymbol{x}'\ \hat{\psi}^\dagger(\boldsymbol{x}')\hat{\psi}^\dagger(\boldsymbol{x}')\hat{\psi}(\boldsymbol{x}')\left[\hat{\psi}^\dagger(\boldsymbol{x}'),\hat{\psi}(\boldsymbol{x})\right]\right\rangle \\
&+ \left\langle\int d\boldsymbol{x}'\ \left[\hat{\psi}^\dagger(\boldsymbol{x}')\hat{\psi}^\dagger(\boldsymbol{x}')\hat{\psi}(\boldsymbol{x}'),\hat{\psi}(\boldsymbol{x})\right]\hat{\psi}(\boldsymbol{x}')\right\rangle\Bigg]
\end{aligned} \tag{2.28}$$

where have repeatedly used linearity of commutators to rearrange the products of field operators. Developing with the bosonic commutation relations, we arrive at:

$$\begin{aligned}
\partial_t\phi(\boldsymbol{x}) = \partial_t\langle\hat{\psi}(\boldsymbol{x})\rangle &= -i\left\langle h(\boldsymbol{x})\hat{\psi}(\boldsymbol{x})\right\rangle - ig\left\langle\hat{\psi}^\dagger(\boldsymbol{x})\hat{\psi}^\dagger(\boldsymbol{x})\hat{\psi}(\boldsymbol{x})\right\rangle \\
\partial_t\phi(\boldsymbol{x}) &= -i\Big(h(\boldsymbol{x})\phi(\boldsymbol{x}) + g|\phi(\boldsymbol{x})|^2\phi(\boldsymbol{x})\Big)
\end{aligned} \tag{2.29}$$

which is precisely the GPE. The coherent state approximation is ultimately a semi-classical approximation: By specifying the form of $\hat{\psi}(\boldsymbol{x})$ as a tensor product state, we enforced the state to be completely separable. As a result, the GPE is unable to capture quantum correlations. Furthermore, it is a zero-temperature formalism as the state was assumed to be pure. Nevertheless, as the order parameter retains the wave-like behaviour of a BEC, the GPE has seen remarkable success in modeling a variety of cold-atom experiments as it is able to model phenomenon such as matter-wave interference [37] and quantum tunneling [38]. In addition, due to the presence of the interaction term, it is also able to model non-linear phenomena such as the formation of solitons [39] and vortices [40].

We note there was nothing special about the coherent state assumption for the form of the state: A BEC does not necessarily have to be in a coherent state, and we could have chosen a completely different ansatz. For example, if we instead let the ansatz be the many-body ground state (i.e $|\Psi\rangle = |N, 0, 0, \ldots\rangle$), we would have arrived at a slightly different equation of motion for a *different* order parameter ($\chi(\boldsymbol{x})$). This is called the Hartree-Fock approximation [41], and leads to the following equation:

$$\partial_t \chi(\boldsymbol{x}) = -i\Big(h(\boldsymbol{x})\chi(\boldsymbol{x}) + g(N-1)|\chi(\boldsymbol{x})|^2\chi(\boldsymbol{x})\Big) \tag{2.30}$$

Eq. 2.30 only differs from Eq. 2.29 in its normalisation: The latter is normalised to $N-1$, and the former to N. In the limit of large N where the semi-classical approximation is most valid, both equations produce the same predictions, reaffirming our claim that there is nothing about the coherent state assumption.

2.3 Quantum Measurement I: General Measurement Theory

2.3.1 Measurement as Entanglement, and also Decoherence

Recall the second postulate of quantum mechanics, which states that measurement of quantum system induces an irrevocable collapse into the eigenstate corresponding to the measured observable [34]. This type of measurement is referred to as a *projective* measurement, and is a subcategory of a broader class of measurements known as Projective Operator Valued Measures (POVM) [42]. In this thesis, we focus primarily on *weak* measurements, which naturally arise if one considers that physical measurements are always made with another device[5].

Let us consider the following scenario: A quantum system ($|S\rangle$) to be measured initially in a superposition of the measured eigenbasis which we denote $|s_1\rangle$ and $|s_2\rangle$, and the measurement device which makes the measurement ($|M\rangle_{\text{ready}}$). Prior to the measurement, the combined state is separable, and may be expressed as:

$$|\Psi_0\rangle = |S\rangle \otimes |M_{\text{ready}}\rangle = \frac{1}{\sqrt{2}}(|s_1\rangle + |s_2\rangle) \otimes |M_{\text{ready}}\rangle \tag{2.31}$$

[5]We generally refer to this as the 'probe' or 'meter' state.

Now, let us consider a unitary operation ($\hat{U}_{\text{ent}}$) which entangles the system in such a way to produce the following state:

$$|\Psi_{\text{ent}}\rangle = \hat{U}_{\text{ent}}|\Psi_0\rangle = \frac{1}{\sqrt{2}}(|s_1\rangle|m_1\rangle + |s_2\rangle|m_2\rangle) \tag{2.32}$$

Here, $|m_1\rangle$ and $|m_2\rangle$ are the possible pointer states of the probe: That is, if the probe measures s_1, it jumps to the state $|m_1\rangle$, and vice versa for s_2. Note the subtlety here: The system and probe states are entangled, **however**, no 'selection' process has been implemented. The combined state specified by $|\Psi_{\text{ent}}\rangle$ is a superposition of *both* measurement results, where each system eigenstate is entangled with a specific probe state which reflects that result.

In practice, we know that the state of the system post measurement must be in either $|s_1\rangle$ or $|s_2\rangle$ (in the classical sense). However, if we *do not* look at the measurement result, we may only describe the state via the density matrix:

$$\hat{\rho}^S_{\text{meas}} = \frac{1}{2}(|s_1\rangle\langle s_1| + |s_2\rangle\langle s_2|) \tag{2.33}$$

This is often called an *ignorance* mixture. Let us now consider what the entangled state $|\Psi_{\text{ent}}\rangle$ looks like if we *only* look at the state of the system: This process is described taking a reduced trace (over the Hilbert space of the probe) of the combined density matrix $\hat{\rho}_{\text{ent}}$:

$$\begin{aligned}\hat{\rho}_{\text{ent}} &= |\Psi_{\text{ent}}\rangle\langle\Psi_{\text{ent}}| \\ &= \frac{1}{2}(|s_1, m_1\rangle\langle m_1, s_1| + |s_2, m_2\rangle\langle m_2, s_2| + |s_1, m_1\rangle\langle m_2, s_2| + |s_2, m_2\rangle\langle m_1, s_1|)\end{aligned} \tag{2.34}$$

Taking the reduced trace over the probe state:

$$\begin{aligned}\hat{\rho}^S_{\text{ent}} &= \text{Tr}_M\{\hat{\rho}_{\text{ent}}\} \\ &= \sum_{i=\{1,2\}} \langle :, m_i|\hat{\rho}_{\text{meas}}|m_i, :\rangle \\ &\equiv \hat{\rho}^S_{\text{meas}}\end{aligned} \tag{2.35}$$

We have arrived at a profound conclusion: A quantum system being measured by an ancillary probe looks *exactly* the same as an entanglement between the system and the probe[6], provided we *only* look at the subspace of the quantum system. This equivalence is very useful, as the state of the probe post measurement is often irrelevant. Next, recall that as entanglement is a unitary process, one would expect the phase coherence of the initial state $|S\rangle$ to be preserved. However, Eq. 2.35 suggests that this is not the case, as the density matrix of the system is now mixed. So where has the coherence gone?

The answer is deceptively simple: Coherence has been transferred to the *combined* superposition state of the system and probe described by $|\Psi_{\text{ent}}\rangle$, and decoherence appears *only* if we look at the subspace of the system. In other words, the measurement by the probe has *decohered* the system. As we see in Chapter 3, this is also the mechanism for measurement backaction.

[6]Specifically, an entanglement between different observables of the system and probe, determined by the form of the entangling Hamiltonian.

2.3.2 Strong and Weak Entanglement

In the example above, we made no assumptions on the form of the pointer states $|m_1\rangle$ and $|m_2\rangle$. Reprinting the entangled state for convenience:

$$|\Psi_{\text{ent}}\rangle = \frac{1}{\sqrt{2}}(|s_1\rangle\,|m_1\rangle + |s_2\rangle\,|m_2\rangle) \tag{2.36}$$

Consider the scenario where the pointer states are *not* orthogonal, and let their overlap be defined as $\langle m_1|m_2\rangle = \lambda$ where $0 \leq \lambda \leq 1$. Now, assume that we observe the probe in state $|m_2\rangle$. Projecting $|\Psi_{\text{ent}}\rangle$ onto $|m_2\rangle$ and renormalising, we find:

$$|\Psi^S_{\text{ent}}\rangle_{m_2} = \sqrt{\frac{1}{1+\lambda^2}}(\lambda\,|s_1\rangle + |s_2\rangle) \tag{2.37}$$

If $\lambda = 1$, then $|m_1\rangle = |m_2\rangle$, and the system is unchanged from its initial state ($|S\rangle$). This is simply a reflection of the fact that a 'measurement' with a single possible result is not a measurement at all! On the contrary, if $\lambda = 0$, the system collapses entirely into $|s_2\rangle$, and this is a precisely a projective measurement of the system[7]. Finally, for intermediate values of λ, the system collapses into some superposition of $|s_1\rangle$ and $|s_2\rangle$. For small λ, the superposition state comprises predominantly of $|s_2\rangle$. We refer to this as a **strong** measurement, as the pointer state $|m_2\rangle$ is strongly correlated with the system existing in $|s_2\rangle$ (and vice versa for $|m_1\rangle$ and $|s_1\rangle$). The case where λ is large is referred to as a **weak** measurement; he state of the system *partially* collapses and is poorly correlated with the measurement result. Projective measurement and no measurement correspond to the infinitely strong and weak measurement regimes, respectively. In practice, the degree of correlation between the system and probe depends on the form of the interaction Hamiltonian: Stronger interaction leads to stronger entanglement, and so forth.

We conclude this section with a further discussion on decoherence. The 'purity' characterises the extent to which a quantum state is mixed [34], and is defined as:

$$\gamma = \text{Tr}\left\{\hat{\rho}^2\right\}, \qquad \frac{1}{d} \leq \gamma \leq 1 \tag{2.38}$$

where d is the dimension of the system's Hilbert space[8]. The purity of the initial system ($|S\rangle$) is maximal. To compute the purity post measurement $|\Psi^S_{\text{ent}}\rangle$, we again write out the combined density matrix for $|\Psi_{\text{ent}}\rangle$ and trace out the probe. In the general case where $\langle m_1|m_2\rangle = \lambda$, we find:

$$\begin{aligned}\hat{\rho}^S_{\text{ent}} &= \text{Tr}_M\{|\Psi_{\text{ent}}\rangle\langle\Psi_{\text{ent}}|\} \\ &= \frac{1}{2}(|s_1\rangle\langle s_1| + |s_2\rangle\langle s_2| + \lambda(|s_1\rangle\langle s_2| + |s_2\rangle\langle s_1|))\end{aligned} \tag{2.39}$$

And the purity is given by:

$$\gamma^S_{\text{ent}}(\lambda) = \text{Tr}\left\{(\hat{\rho}^S_{\text{ent}})^2\right\} = \frac{1}{2}(1+\lambda^2) \tag{2.40}$$

[7]Note: Though the type of measurement made on the system is dependent on the measurement strength, the measurement probe is always measured projectively.

[8]For our example above, $d = 2$.

Clearly, the 'no-measurement' scenario where $\lambda = 1$ leads to maximal purity[9], while the state is maximally mixed for a projective measurement ($\lambda = 0$). In general, the system is decohered by an amount proportional to the measurement strength.

2.3.3 Conditional and Unconditional States

We conclude this section with a discussion on the differences between conditional and unconditional quantum states. Consider an experiment where a quantum state subject to repeated measurement:

- The *conditional* quantum state refers to a single experimental realisation. As measurement collapse is stochastic, the trajectory of the system in time is *conditioned* on the specific measurement record for that trajectory. Any feedback applied to the system is derived from the measurement record.
- The *unconditional* quantum state is obtained by averaging over many different conditional state (many different experimental realisations). Hence, its evolution is not conditioned on any specific measurement record, and describes the mean dynamics of the state over many experimental runs. For feedback cooling, we only care about the unconditional dynamics, as it tells us how effective our feedback is on average.

The distinction between conditional and unconditional dynamics is crucial. The starting point for previous studies of feedback cooling [2, 43] was to derive and simulate an equation of motion for the *conditional* quantum state, before recovering unconditional dynamics in the standard manner. The failures of previous studies largely arose from difficulties in representing the conditional quantum state. As we will see in Section 3.1, a key aspect of our new approach is that it completely bypasses the conditional state and directly simulates the unconditional dynamics instead.

Finally, note that measurement induced decoherence appears *only* in the unconditional state; that is, if we average over *all* possible measurement results[10]. Conditioned states are always pure [11], as one has access to the measurement result. However, this does *not* imply that conditioned states are immune to measurement backaction.

[9] As expected, as the initial state has not changed.

[10] This is equivalent to not looking at the measurement result, i.e tracing over the subspace of the measurement probe.

[11] The obvious exception being if the initial state was mixed to begin with.

2.4 Quantum Measurement II: Open Quantum Systems

We have included this section in the hope that it proves useful in highlighting the differences between the methods used in previous studies and our new approach. We start by defining some assumptions and terminology used in the remainder of this thesis:

- In the context of feedback cooling, the system always refers to the atomic gas, while the measurement probe is generally light which is shone incident on the atoms. In this thesis, the entangling Hamiltonians we encounter in Chapters 3 and 4 generate correlations between a desired atomic observable and the phase quadrature of the light. Hence, a projective measurement of the (phase quadrature of the) light at the detector produces an estimate of the corresponding atomic observable.
- In both the single and multi-mode cases, the light is always treated as a coherent state (in each mode) with a sufficiently large coherent state amplitude (i.e optical intensity). In previous studies, this assumption justified treating the light via semi-classical reservoir approximations [44, 45].

Previous studies of feedback cooling sought an equation of motion for the conditioned quantum stat and modeled continuous weak measurements. When the measurement probe is significantly larger than the measured, system, the measurement may be described using tools from the theory open quantum systems [45], which treats the light as an environment coupled to the system. Eventually, one arrives at the following master equation governing evolution of the conditioned quantum state ($\hat{\rho}_c$):

$$\partial_t \hat{\rho}_c = -i[\hat{H}(t), \hat{\rho}_c] + \gamma \mathcal{D}[\hat{L}_i]\hat{\rho}_c dt + \sqrt{\gamma}\mathcal{H}[\hat{L}_i]\hat{\rho}_c dW(t) \tag{2.41}$$

where γ is the measurement strength, $\hat{L}_i$ is the measured observable, and $\mathcal{D}[\hat{L}_i]$ and $\mathcal{H}[\hat{L}_i]$ are the decoherence and innovations Lindblad *superoperators*, respectively [46]. The former implements measurement backaction, and the latter incorporates information gained from the measurement, conditioning the state to be consistent with the measurement result. The stochasticity of measurement collapse is encoded in the real *Wiener* process ($dW(t)$). We refer to [42, 47] for an excellent introduction to stochastic noise processes in the context of quantum measurement. For our purposes, it is sufficient to note that the Wiener noise is a continuous real Gaussian noise with unit variance, and generates the measurement record for a *single* simulation[12] of Eq. 2.41. Specifically, it drives the measurement signal:

$$dy = \sqrt{\gamma}\,\langle \hat{L}_i^\dagger + \hat{L}_i \rangle\, dt + dW(t) \tag{2.42}$$

where y is typically the measured phase quadrature of the light. Crucially, note that Eq. 2.41 is a *reduced* master equation, as it only governs the evolution of the atomic system. The light has been traced out, and its quantum statistics has been transferred to the Wiener noise. Averaging multiple realisations of Eq. 2.41 recovers the *unconditional* master equation:

$$\partial_t \hat{\rho} = -i[\hat{H}(t), \hat{\rho}] + \gamma \mathcal{D}[\hat{L}_i]\hat{\rho} dt \tag{2.43}$$

Naturally, one might ask why it is not possible to directly simulate Eq. 2.43. The answer lies in the fact that feedback is always *conditioned* on a specific measurement record, which exists only for Eq. 2.41. Indeed, it is essentially impossible to write out an analytical form for the *unconditioned* feedback Hamiltonian.

[12] Physically, this corresponds to a single realisation of the experiment.

2.5 The Elegance of Phase-Space

2.5.1 Quantum Phase-Space: The Wigner Function

Originally written down by Eugene Wigner as a quantum correction to thermodynamic equilibrium [48], the Wigner function maps a general quantum state into a real-valued distribution function defined on a quantum phase space. We first present Wigner's original definition in terms of the conjugate position and momentum variables for a single particle quantum state:

$$\mathcal{W}(x,p) = \frac{1}{2\pi\hbar}\int dy\, \langle x-y|\hat{\rho}|x+y\rangle\, e^{-iyp/\hbar} \tag{2.44}$$

where $\hat{\rho}$ is the density matrix of the quantum state. On first encounter, one may interpret the Wigner function as a joint probability distribution for the position and momentum of a particle. However, the Wigner function is not a true probability distribution is may take on negative values. Furthermore, the notion of a 'joint' probability for a pair of co-ordinates (x,p) is ill-defined for a quantum due to the uncertainty principle. Hence, the Wigner function is a *quasi-probability* distribution. Nevertheless, in some ways, it behaves remarkably similar to a classical joint probability distribution function. Namely, its marginals recover the position and momentum wavefunctions, and it obeys the correct normalisation:

$$\int dp\, \mathcal{W}(x,p) = \psi(x), \qquad \int d\, \mathcal{W}(x,p) = \psi(p), \qquad \int dp \int dx\, \mathcal{W}(x,p) = 1 \tag{2.45}$$

The single-particle Wigner function in Eq. 2.44 may be generalised to the many-body case. We shall see the formalism to do so in the following section, where we briefly review the general class of phase-space methods. For now, the many-body Wigner function for a single mode is easily obtained simply by replacing the position and momentum variables with the coherent state amplitudes (α,α^*) [44]. The Wigner functions for some various quantum states are plotted in Fig. 2.1 below.

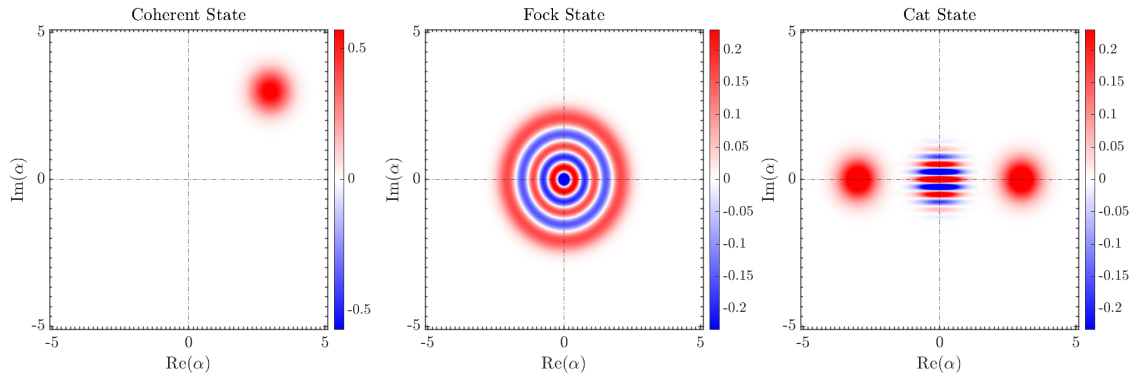

Figure 2.1: Single Mode Wigner functions for different quantum states. The coherent state has amplitude $\alpha_0 = 3+3i$, the Fock state is of $n=5$, and the cat state is of the form $|\text{meow}\rangle = (|\alpha_0\rangle + |-\alpha_0\rangle)/\sqrt{2}$. The Wigner functions of both the Fock and Cat states can not be sampled in terms of Wigner trajectories as they contain negativity.

2.5.2 A Generalised Quantum Phase-Space

Wigner was motivated to develop a formalism in which the probabilistic methods of classical statistical mechanics could be adapted and applied to quantum problems. Much progress has been made since his original paper in 1932, and the study of quantum phase-space methods has lead to the development of tractable computational techniques for many-body quantum systems, particularly in the areas of quantum optics and ultra-cold atomic gases [49, 50].

Phase-space methods map operators[13] which act on the Hilbert space of the quantum state to an equivalent quantum phase-space distribution function defined in terms of complex, scalar-valued phase-space variables. The mapping is determined by choosing an association rule which specifies the ordering of non-commuting operators when mapped onto commuting phase-space variables. Different association rules lead to different phase-space distribution functions. We refer to the excellent review by Lee *et al.* in [50] for further discussion. Under this formalism of operator orderings, the single-mode Wigner function may alternatively be expressed as the Fourier transform of its characteristic function ($\chi_{\mathcal{W}}(\lambda,\lambda^*)$) [51]:

$$\mathcal{W}(\alpha,\alpha^*) = \frac{1}{\pi^2}\int d^2\lambda\, e^{\lambda^*\alpha-\lambda\alpha^*}\chi_{\mathcal{W}}(\lambda,\lambda^*), \qquad \chi_{\mathcal{W}}(\lambda,\lambda^*) = \mathrm{Tr}\left\{\hat{\rho}e^{\lambda\hat{a}^\dagger-\lambda^*\hat{a}}\right\} \tag{2.46}$$

where $\hat{a}^\dagger$ and $\hat{a}$ are the creation and annihilation operators for the single quantum mode. The Wigner function obeys the *symmetrically ordered* association rule, is reflected in the exponential of the characteristic function. In contrast, the Sudharshan-Glauber P-function and Husimi Q-functions obey normal and anti-normal orderings, respectively, and have characteristic functions:

$$\chi_{\mathcal{P}}(\lambda,\lambda^*) = \mathrm{Tr}\left\{\hat{\rho}e^{\lambda\hat{a}^\dagger}e^{-\lambda^*\hat{a}}\right\} \qquad \chi_{\mathcal{Q}}(\lambda,\lambda^*) = \mathrm{Tr}\left\{\hat{\rho}e^{-\lambda^*\hat{a}}e^{\lambda\hat{a}^\dagger}\right\} \tag{2.47}$$

In thesis, we restrict our attention to the Wigner function, but note that extensions of the P-representation has seen great success in modeling a variety of problems in quantum optics [52, 53], while the Q-function is commonly used for visualisation of quantum states. The Wigner function in Eq. 2.46 generalises to multi-mode cases in the expected manner: For a system with M modes, denote the vector of coherent state amplitudes as $\boldsymbol{\alpha} = [\alpha_1, \alpha_2, \ldots, \alpha_M]^\dagger$. The multi-mode Wigner function is now given by:

$$\mathcal{W}(\boldsymbol{\alpha},\boldsymbol{\alpha}^*) = \int \frac{d^{2M}\boldsymbol{\lambda}}{\pi^{2M}}\left(\prod_{n=1}^{M} e^{\lambda_n^*\alpha_n-\lambda_n\alpha_n^*}\right)\mathrm{Tr}\left\{\hat{\rho}\prod_{n=1}^{M} e^{\lambda_n\hat{a}_n^\dagger-\lambda_n^*\hat{a}_n}\right\} \tag{2.48}$$

where we have adopted the notation:

$$\int d^2\boldsymbol{\lambda} = \prod_n \int d^2\lambda_n \tag{2.49}$$

In the next section, we shall see how one may derive a functional Wigner representation, which is required in the case that the quantum field is represented in terms of a continuous spatial basis.

[13] Note that the mapping may be performed for *arbitrary* operators, However, we generally seek a representation of the quantum state, so the relevant operator is the density operator.

2.5.3 Simulations in Phase-Space: Operator Correspondences

Phase-space representations allow Von-Neumann and master equations for the density matrix to be equivalently mapped into an equation of motion for the Wigner[14] function. The mapping is performed using operator correspondences which may be derived from the characteristic function [49]:

$$\hat{a}\hat{\rho} \leftrightarrow \left(\alpha + \frac{1}{2}\frac{\partial}{\partial\alpha^*}\right)\mathcal{W}(\alpha,\alpha^*) \qquad \hat{a}^\dagger\hat{\rho} \leftrightarrow \left(\alpha^* - \frac{1}{2}\frac{\partial}{\partial\alpha}\right)\mathcal{W}(\alpha,\alpha^*)$$
$$\hat{\rho}\hat{a} \leftrightarrow \left(\alpha - \frac{1}{2}\frac{\partial}{\partial\alpha^*}\right)\mathcal{W}(\alpha,\alpha^*) \qquad \hat{\rho}\hat{a}^\dagger \leftrightarrow \left(\alpha^* + \frac{1}{2}\frac{\partial}{\partial\alpha}\right)\mathcal{W}(\alpha,\alpha^*) \tag{2.50}$$

We will explicitly demonstrate an application of these correspondences in Chapter 3 for the quantum coupled anharmonic oscillator. In the multi-mode case, we instead seek operator correspondences for the quantum field operator ($\hat{\psi}(\boldsymbol{x})$). A straightforward way to derive these is to first introduce the functional Wigner distribution ($\mathcal{W}[\psi(\boldsymbol{x}),\psi^*(\boldsymbol{x})]$), and assert that the phase-space representation of the field-operator (i.e $\hat{\psi}(\boldsymbol{x}) \leftrightarrow \psi(\boldsymbol{x})$) obey correspondences analogue to those of Eq. 2.50. This yields the following correspondences:

$$\hat{\psi}(\boldsymbol{x})\hat{\rho} \leftrightarrow \left(\psi(\boldsymbol{x}) + \frac{1}{2}\frac{\delta}{\delta\psi^*(\boldsymbol{x})}\right)\mathcal{W}[\psi,\psi^*] \quad \hat{\psi}^\dagger(\boldsymbol{x})\hat{\rho} \leftrightarrow \left(\psi^*(\boldsymbol{x}) - \frac{1}{2}\frac{\delta}{\delta\psi(\boldsymbol{x})}\right)\mathcal{W}[\psi,\psi^*]$$
$$\hat{\rho}\hat{\psi}(\boldsymbol{x}) \leftrightarrow \left(\psi(\boldsymbol{x}) - \frac{1}{2}\frac{\delta}{\delta\psi^*(\boldsymbol{x})}\right)\mathcal{W}[\psi,\psi^*] \quad \hat{\rho}\hat{\psi}^\dagger(\boldsymbol{x}) \leftrightarrow \left(\psi^*(\boldsymbol{x}) + \frac{1}{2}\frac{\delta}{\delta\psi(\boldsymbol{x})}\right)\mathcal{W}[\psi,\psi^*] \tag{2.51}$$

Note that the partial derivatives of Eq. 2.50 have been replaced with functional derivatives. In practice, the field operator is represented as a finite sum of discrete single-particle basis annihilation operators, i.e $\hat{\psi}(\boldsymbol{x}) = \sum_{n=0}^{M-1}\hat{a}_n\phi_n(\boldsymbol{x})$. Hence, the functional derivatives in Eq. 2.51 may similarly be recast into a finite basis expansion:

$$\frac{\delta}{\delta\psi(\boldsymbol{x})} = \sum_{n=0}^{M-1}\phi_n^*(\boldsymbol{x})\frac{\partial}{\partial\alpha_n} \tag{2.52}$$

where α_n are the discrete phase-space variable for different modes as defined in Eq. 2.48. In summary, applying the operator correspondences to the master equation ($\partial_t\hat{\rho}$) produces an equivalent equation of motion for the quasi-probability phase-space function ($d\mathcal{W}$). For a N-mode quantum system, the simulation complexity is reduced from $\mathcal{O}(N^2)$ to $\mathcal{O}(N)$[15]. However, solving a PDE with $2N$ dimensions is still a challenging task, even for N of order unity. Hence, we are motivated to further reduce the dimensionality of the problem.

[14] Or in general, any quasi-probability phase-space distribution.

[15] The density matrix contains N^2 components, while the equation of motion for $\mathcal{W}(\boldsymbol{\alpha},\boldsymbol{\alpha}^*)$ is a PDE with dimension $2N$.

2.5.4 The Fokker-Planck Equation and Truncated Wigner Approximation

The Fokker-Planck Equation (FPE) is the general equation of motion for an arbitrary probability density function, and takes the following form:

$$\partial_t \mathcal{P}(\boldsymbol{x},t) = -\sum_{j=1}^{N} \partial_j [A_j(\boldsymbol{x})\mathcal{P}(\boldsymbol{x},t)] + \sum_{j=1}^{N}\sum_{k=1}^{N} \partial_i \partial_j [D_{jk}(\boldsymbol{x})\mathcal{P}(\boldsymbol{x},t)] \tag{2.53}$$

where $\boldsymbol{A}(\boldsymbol{x})$ is the deterministic drift vector, and D_{jk} are entries of the diffusion tensor:

$$D_{jk}(\boldsymbol{x},t) = \frac{1}{2}\sum_{l=1}^{M} B_{jl}(\boldsymbol{x},t)B_{lk}(\boldsymbol{x},t) \tag{2.54}$$

The matrix $\boldsymbol{B}$ need only have dimensions $N \times M$ in order to guarantee a square diffusion matrix [44]. All FPEs may be stochastically *unraveled* into a set of Stochastic Differential Equations (SDE) for the variables $\boldsymbol{x}$. In Itô[16] form, the SDEs are of the form:

$$dx_j = A_j(\boldsymbol{x})dt + \sum_k B_{jk}(\boldsymbol{x})dW_k \tag{2.55}$$

where dW_k is a Wiener process in Itô form. This is a key result, as it essentially states that the evolution of a system with N-modes may be equivalently simulated via an *ensemble* of trajectories, where each trajectory comprises a set of N coupled SDE. However, in practice, the resulting PDE obtained for the Wigner function generally contains higher-order derivative terms ($n \geq 3$), and is hence not of FPE form. However, if one were to *truncate* all higher order derivative times, the remaining equation may now be mapped onto a set of N SDEs for the phase-space variables, whose initial conditions are sampled from the initial Wigner function. Time evolution of the Wigner function (and hence, of the quantum state) may now be obtained by evolving an ensemble of phase-space trajectories. In the literature, this approach is referred to as the *Truncated Wigner Approximation* (TWA) [54].

In summary, the TWA produces a first-order quantum correction to mean-field predictions [55] and is hence (partially) able to capture dynamics associated with correlations of a full quantum field. In Chapter 3, we will discuss the validity of the TWA in more detail. For now, we look at the equation of motion for the functional Wigner distribution by applying the correspondences in Eqs. 2.51 to the master equation generated by the cold-atom Hamiltonian in Eq. 2.21. We will simply write out the result, referring to [49] for more detailed derivation:

$$\begin{aligned}\partial_t \mathcal{W}[\psi,\psi^*] = \frac{i}{\hbar}\int d^3\boldsymbol{x}\Bigg\{ &\frac{g}{4}\frac{\delta}{\delta\psi(\boldsymbol{x})\delta\psi^*(\boldsymbol{x})}\psi^*(\boldsymbol{x})\frac{\delta}{\delta\psi^*(\boldsymbol{x})} + \text{h.c} \\ &+ \frac{\delta}{\delta\psi(\boldsymbol{x})}\Big(h(\boldsymbol{x}) + g\Big(|\psi(\boldsymbol{x})|^2 - \delta^3(\boldsymbol{x},\boldsymbol{x})\Big)\Big) + \text{h.c}\Bigg\}\mathcal{W}[\psi(\boldsymbol{x}),\psi^*(\boldsymbol{x})]\end{aligned} \tag{2.56}$$

Where $h(\boldsymbol{x})$ is the single-particle Hamiltonian defined in Eq. 2.22, and h.c denotes the Hermitian conjugate of the previous term. We see that the first line of Eq. 2.56 contains

[16] There are two commonly used definitions of the stochastic integral: The Itô and Stratonovich integrals. See [47] for more details.

third order function derivatives. If we apply the TWA and truncate these terms, the resulting equation of motion looks like:

$$\partial_t \mathcal{W}[\psi,\psi^*] \approx \frac{i}{\hbar}\int d^3\boldsymbol{x}\,\frac{\delta}{\delta\psi(\boldsymbol{x})}\Big(h(\boldsymbol{x})+g\Big(|\psi(\boldsymbol{x})|^2-\delta^3(\boldsymbol{x},\boldsymbol{x})\Big)\Big)+\text{h.c}\Big\}\mathcal{W}[\psi,\psi^*] \tag{2.57}$$

Eq. 2.57 is a *functional* FPE defined in terms of the phase-space functional $\psi(\boldsymbol{x})$, and may be analogously unravelled into into the following SDE for $\psi(\boldsymbol{x})$

$$i\hbar\partial_t\psi(\boldsymbol{x}) = \Big(h(\boldsymbol{x})+g\Big(|\psi(\boldsymbol{x})|^2-\delta^3(\boldsymbol{x},\boldsymbol{x})\Big)\Big)\psi(\boldsymbol{x}) \tag{2.58}$$

On inspection of Eq. 2.58, we see that it is exactly the GPE[17] which describes mean-field dynamics of the cold-atom Hamiltonian. This is a fundamental point: In the absence of diffusion terms in the master equation[18], the unraveled SDEs for *single* trajectories of the Wigner phase-space variables are identical to mean-field dynamics. Hence, we emphasise that the power of the TWA lies in its ability to capture the quantum statistics of the initial state by sampling its Wigner function.

2.5.5 Simulations in Phase-Space: Initial State Sampling and Ordered Moments

Aside from the truncation error, TWA simulations are limited by initial state sampling. Wigner functions which contain negativity may not be accurately sampled in terms of Wigner trajectories. In fact, Hudson's theorem guarantees that only Gaussian quantum states have completely positive Wigner functions [56], severely limiting the range of samplable states to coherent, thermal, and a restricted set of squeezed states [57]. A single-mode coherent state with amplitude α_0, that is $\hat{\rho} = |\alpha_0\rangle\langle\alpha_0|$ may be sampled in the following way:

$$\alpha(0) = \alpha_0 + \frac{1}{\sqrt{2}}(\eta_1 + i\eta_2) \tag{2.59}$$

where η_1 and η_2 are real, independent random Gaussian variables with with zero mean and unit variance. In the absence of noise, the initial conditions of individual phase-space trajectories are identical and equal to α_0, resembling the behaviour of a state in classical phase space.

Finally, we discuss how expectations of observables may be extracted from the phase-space variables. Moments computed from the Wigner function correspond to symmetrically ordered operator[19] averages [49] and may be computed from the Wigner function in the way one would treat a classical probability distribution. That is, for the multi-mode Wigner function, we have:

$$\langle\{(\hat{a}_j^\dagger)^n(\hat{a}_k)^m\}_{\text{sym}}\rangle = \overline{(\alpha_j^*)^n(\alpha_k)^m} \equiv \int d^{2M}\boldsymbol{\alpha}\,(\alpha_j^*)^n(\alpha_k)^m\mathcal{W}(\boldsymbol{\alpha},\boldsymbol{\alpha}^*) \tag{2.60}$$

Where the notation $\overline{f(\boldsymbol{\alpha},\boldsymbol{\alpha}^*)}$ refers to ensemble averages of the quantity $f(\boldsymbol{\alpha},\boldsymbol{\alpha}^*)$ computed across all Wigner trajectories. Similarly, moments computed from the P and Q-

[17] If the delta function is discarded, which we are allowed to do as corresponds to a global phase rotation.
[18] In other words, the master equation is of Von-Neumann form.
[19] Recall previously that the Wigner function obeys the symmetrically ordered association rule.

functions correspond to normally and anti-normally ordered operator averages, respectively:

$$\langle\{(\hat{a}_j^\dagger)^n(\hat{a}_k)^m\}_{\text{norm}}\rangle = \overline{(\alpha_j^*)^n(\alpha_k)^m} \equiv \int d^{2M}\boldsymbol{\alpha}\,(\alpha_j^*)^n(\alpha_k)^m\mathcal{P}(\boldsymbol{\alpha},\boldsymbol{\alpha}^*)$$
$$\langle\{(\hat{a}_j^\dagger)^n(\hat{a}_k)^m\}_{\text{anti-norm}}\rangle = \overline{(\alpha_j^*)^n(\alpha_k)^m} \equiv \int d^{2M}\boldsymbol{\alpha}\,(\alpha_j^*)^n(\alpha_k)^m\mathcal{Q}(\boldsymbol{\alpha},\boldsymbol{\alpha}^*) \tag{2.61}$$

Let us consider the simplest example of a single-mode number operator. As we have:

$$\langle\{\hat{a}^\dagger\hat{a}\}\rangle_{\text{sym}} = \frac{1}{2}\langle\{\hat{a}^\dagger\hat{a}+\hat{a}\hat{a}^\dagger\}\rangle \equiv \langle\hat{a}^\dagger\hat{a}\rangle + \frac{1}{2} \tag{2.62}$$

The *real* expectation value for the mean number is given by:

$$\langle\hat{a}^\dagger\hat{a}\rangle = \overline{|\alpha|}^2 - \frac{1}{2} \tag{2.63}$$

The factor of a half is generally referred to as the *Wigner correction*, and may be interpreted as a quantum correction arising from treating the Wigner function as a classical probability distribution (in Eq. 2.61). Of course, the Wigner correction varies for different operators, and typically become more complex for higher order moments. For low order moments of number, the Wigner correction is often negligible for highly populated modes, though computing the correction is still the safest choice. We refer to [49, 58] for a list of Wigner corrections commonly used in this thesis. This concludes both our discussion on quantum phase-space, as well as the entirety of the background chapter.

Chapter 3

Quantum Feedback: Two-Modes

As described in Chapter 1, previous attempts to model feedback cooling employed methods from the theory of open quantum systems, where measurement effects are explicitly encoded via Linbladian superoperator terms in the conditional master equation (CME). Simulation of the CME required development of a new technique [59], as did the simulation of number-like density measurements [60]. Unfortunately, these methods have proven to be unscalable to large quantum systems (large N), plagued by numerical instabilities arising from sampling technicalities [10].

Our eventual goal is to simulate feedback cooling of Bose gases to quantum degeneracy using our new approach. In order to establish its validity, we first apply it to a two-mode system, whose low-dimensionality permits an exact solution against which we may benchmark our method.

This chapter contains new work as well as the background required to understand it. In Section 3.1, we first describe an existing method known as Number-Phase Wigner (NPW), which is currently the leading method of choice for the simulation of controlled quantum systems. Next, we introduce our approach for the first time, and point out the key differences between the two methods. Section 3.2 introduces the framework for describing two-mode systems, followed by our system of interest (Coupled Anharmonic Oscillators) in Section 3.3. Section 3.4 investigates the accuracy of the TWA in the absence of feedback dynamics, while Sections 3.5-3.6 explain the implementation of measurement and feedback for TWA using our approach as well the exact Stochastic Schrodinger Equation (SSE). Sections 3.7-3.8 contain the bulk of our simulation results and comparisons. Finally, we conclude with a discussion on the generalisation of our approach to multiple modes, and present ideas towards establishing the correspondence between our approach and NPW. Preliminary simulations were performed using MATLAB, and scaled up using the GADI Supercomputer at the National Computational Infrastructure (NCI).

3.1 A New and Old Approach

3.1.1 A History Lesson: Number Phase Wigner (NPW) and Particle Filters

The simulation of conditioned quantum systems has historically been bottle-necked by the difficulties in accurate sampling and numerical representation of the quantum state [61]. We have developed an alternative approach which may alleviate the sampling obstacle in its entirety.

To understand how our approach differs to existing methods, we first review the Number-Phase Wigner (NPW) particle filter [60], which at the time of writing is the leading tool for simulation of conditioned quantum systems subject to number-like measurement. It aims to unravel the conditional master equation introduced in Section 2.4 into an equivalent set of stochastic phase-space equations, analogous to those of Section 2.5.4. However, standard unraveling procedures may not be used as the 'conditioning' of the quantum state due to measurement leads to additional stochastic terms in the FPE[1]. To overcome this limitation, Hush *et al.* developed a new set of unraveling techniques [59] inspired by a class of filtering theory techniques called *particle-filters* [62, 63]. Let us consider an unraveling of the conditional master equation of Eq. 2.54 into the following set of SDEs for the N phase-space variables $\boldsymbol{x} = \{x_1, \ldots, x_j, \ldots, x_N\}$:

$$\begin{aligned} dx_j &= A_j(\boldsymbol{x})dt + \sum_k B_{jk}(\boldsymbol{x})dW_k + \sum_k C_{jk}(\boldsymbol{x})dV_k \\ d\omega &= \alpha(\boldsymbol{x})\omega dt + \sum_j \omega\beta_j(\boldsymbol{x})dW_j \end{aligned} \tag{3.1}$$

The resulting SDEs closely resemble the equations of section 2.5.4, with additional terms we now address:

- The unraveling has introduced an additional set of *fictitious* noises which we denote dV_k. In contrast to the 'real' noises dW_k which correspond to a single stochastic measurement record obtained in a single experimental realisation, the fictitious noises are an artefact of the unraveling process, and are necessary to capture the phase diffusion and quantum statistics of the conditioned state. For a simulation of a single conditional measurement record dW, one makes M copies of the initial vector $\boldsymbol{x}$, and evolves *each* of them under Eqs. 3.1 with a **different** fictitious noise dV_k for $k \in 1, \ldots, M$, leading to a set of M fictitious trajectories. Crucially, all fictitious trajectories evolve under the *same* dW, while different fictitious trajectories may be coupled together via the sum in Eqs. 3.1. This 'crosstalk' between fictitious trajectories allows non-local quantum correlations to be captured. The ensemble of fictitious trajectories may be interpreted as the phase-space representation of the conditioned quantum state.

- The additional scalar 'weights' variable ω. Each fictitious trajectory is assigned its **own** weight: The state vector for each trajectory now contains $M + 1$ variables. Physically, each weight reflects the confidence that a certain fictitious trajectory is consistent with the measurement record, i.e our knowledge of the system. For example, consider a quantum system undergoing continuous measurement of an observable $\hat{O}$, with corresponding phase-space variable $\mathcal{O} = f(\boldsymbol{x})$. We expect the long-term behaviour of the state to approach an eigenstate of $\hat{O}$ corresponding to a specific eigenvalue. Hence, fictitious trajectories for which $\mathcal{O}$ differs greatly from the eigenvalue must be a smaller component of the state. It is then natural for expectation values of observables to be given by the *weighted average* over all fictitious trajectories:

$$\langle \hat{O} \rangle_c = \mathbb{E}_c[f(\boldsymbol{x})] = \frac{\mathbb{E}[\omega f(\boldsymbol{x})]}{\mathbb{E}[\omega]} \tag{3.2}$$

  where we have used $\langle \hat{O} \rangle_c$ and $\mathbb{E}_c[f(\boldsymbol{x})]$ to denote the *conditional* average correspond-

[1]The innovations term in $d\hat{\rho}_c$ introduces additional stochastic terms, so it is no longer in FPE form.

ing to a single real noise dW. This implies that feedback terms are conditioned on weighted averages derived from all fictitious trajectories, so the same feedback is applied to all fictitious trajectories. To obtain the *unconditioned* average, another round of averaging over many different real noises dW must be performed.

Recall that expectation values computed from stochastic phase-space variables correspond to moments of the underlying quasi-probability distribution:

$$d\overline{f} = \int d\boldsymbol{x}\, d\mathcal{P}(\boldsymbol{x},t) f(\boldsymbol{x}) \tag{3.3}$$

where $\mathcal{P}(\boldsymbol{x},t)$ is a phase-space quasi-probability distribution. Using rules from stochastic calculus, it may be shown that the corresponding evolution equation for $\mathcal{P}(\boldsymbol{x},t)$ is given by the following expression:

$$\begin{aligned} d\mathcal{P}(\boldsymbol{x},t) = \Bigg\{ \Bigg((\alpha - \overline{\alpha}) + \sum_k \beta_k(\beta_k - \overline{\beta_k}) - \sum_k \partial_k A_k - \sum_{jk} \partial_j (B_{jk}(\beta_k - \overline{\beta_k})) \\ + \frac{1}{2} \sum_{ijk} \partial_i \partial_j (B_{ik}B_{jk} + C_{ik}C_{jk}) \Bigg) dt \\ + \sum_k (\beta_k - \overline{\beta_k}) dW_k - \sum_{jk} \partial_j B_{jk} dW_k \Bigg\} \mathcal{P}(\boldsymbol{x},t) \end{aligned} \tag{3.4}$$

Equation 3.4 is referred to as the *conditional* FPE (CFPE). Its derivation is quite involved, so we refer the reader to [64] for further detail. The upshot is that conditional master equations such as Eq. 2.41 may be unraveled using the recipe above and simulated using Eqs. 3.1. These methods are not entirely new: the form of Eq. 3.4 is similar to the Kushner-Stratonovich equations [61, 65], a classical filtering equation for stochastic simulation, while applications to quantum systems have also been proposed in [66, 67].

In Section 2.5 we saw that traditional phase-space representations such as the Wigner, Q, and P-functions are constructed using a coherent state basis[2]. However, feedback cooling, amongst other controlled cold-atom experiments commonly employ number-like (e.g density) measurements, rendering the underlying coherent state basis inappropriate for the physical problem. The Number-Phase Wigner (NPW) is a phase-space representation constructed in terms of the number and phase quadrature [60]. Hence, it is in 'harmony' with number-like measurements, and unravels into the form of the CFPE. Historically, it has been the method of choice for investigations of continuous feedback cooling [2, 10].

[2]This is why the operator correspondences map annihilation operators to coherent state amplitudes.

3.1.2 A Lesson From History: Undersampling and Feedback

Particle-filter methods are prone to what is known in the literature as sample impoverishment [62]. Consider a naive integration[3] of the weights variable in Eq. 3.1. The weights evolve at an exponential rate, so a few trajectories with larger weights rapidly grow and dominate the contribution to expectation values in a timescale significantly shorter than that of natural dynamics. Physically, this phenomenon corresponds to the rapid narrowing of the conditional phase-space function quickly as it approaches an eigenstate. If there are only a few trajectories with non-negligible weights, the quantum state is no longer well represented: It is significantly undersampled.

Numerous algorithms to address sample impoverishment exist in the particle-filter literature. One example is the sequential importance resampling method [68], where trajectories with negligible weights are continuously replaced with copies of those with dominant weights. This approach was employed in previous studies of feedback cooling [2, 10] to partial success, where their simulations remained convergent for temperatures $T < T_c$. However, they were performed with extremely low ($N \sim 1000$) particle numbers as resampling is not scalable to greater particle numbers[4].

3.1.3 The Present: Our New Approach

We are now in a position to introduce our new approach and how it differs from particle-filter methods derived from the CFPE. We first present the key points:

- We do not distinguish between 'real' and 'fictitious' trajectories. In other words, we do not make multiple copies of the Wigner function for the initial unconditional quantum state.

- Each Wigner trajectory is evolved independently; they are not coupled together via either fictitious noises or feedback. Each trajectory is measured independently and receives its **own** feedback. Hence, at no point do we have a conditional state; unconditional dynamics are recovered by averaging over all independent trajectories.

The advantages of our method are clear: We have completely sidestepped the obstacle of undersampling simply by disregarding the conditional state, and hence require far fewer trajectories for convergence. There are some further technicalities of interest, which we will provide for completeness:

- The 'trick' of our approach is quite subtle: By treating (and measuring) trajectories independently, each trajectory is effectively an 'infinitely undersampled' representation of a conditional quantum state. However, as the aim of feedback is to drive towards a steady state (attractor), we predict that the mean, unconditional dynamics reproduce the correct statistics. Furthermore, we hypothesise that the quantum noise associated with each conditioned state is well mimicked by the quantum noise of the initial state sampling and measurement backaction.

[3] By 'naive', we mean forget about the stochastic term.

[4] In general, larger particle numbers lead to larger **absolute** numbers (e.g greater normalisation of wavefunction) in the equations. Hence, any differences in the weights are also amplified, leading to faster weight divergence.

- **In previous methods, the light is treated with a series of reservoir approximations and traced out at the level of the CME: The CME is a *reduced* master equation describing only the dynamics of the atomic state [44, 69]. In our approach, the light is only projected *post* measurement[5]. Hence, we are able to implicitly model backaction through the entangling dynamics between the atomic state and (noisy) light, in contrast to requiring an explicit decoherence superoperator, as is present in the CME. Though both approaches are equivalent, we believe ours is easier to implement numerically.**

A summary of the key differences between existing methods and our method is presented below, in Fig. 3.1.

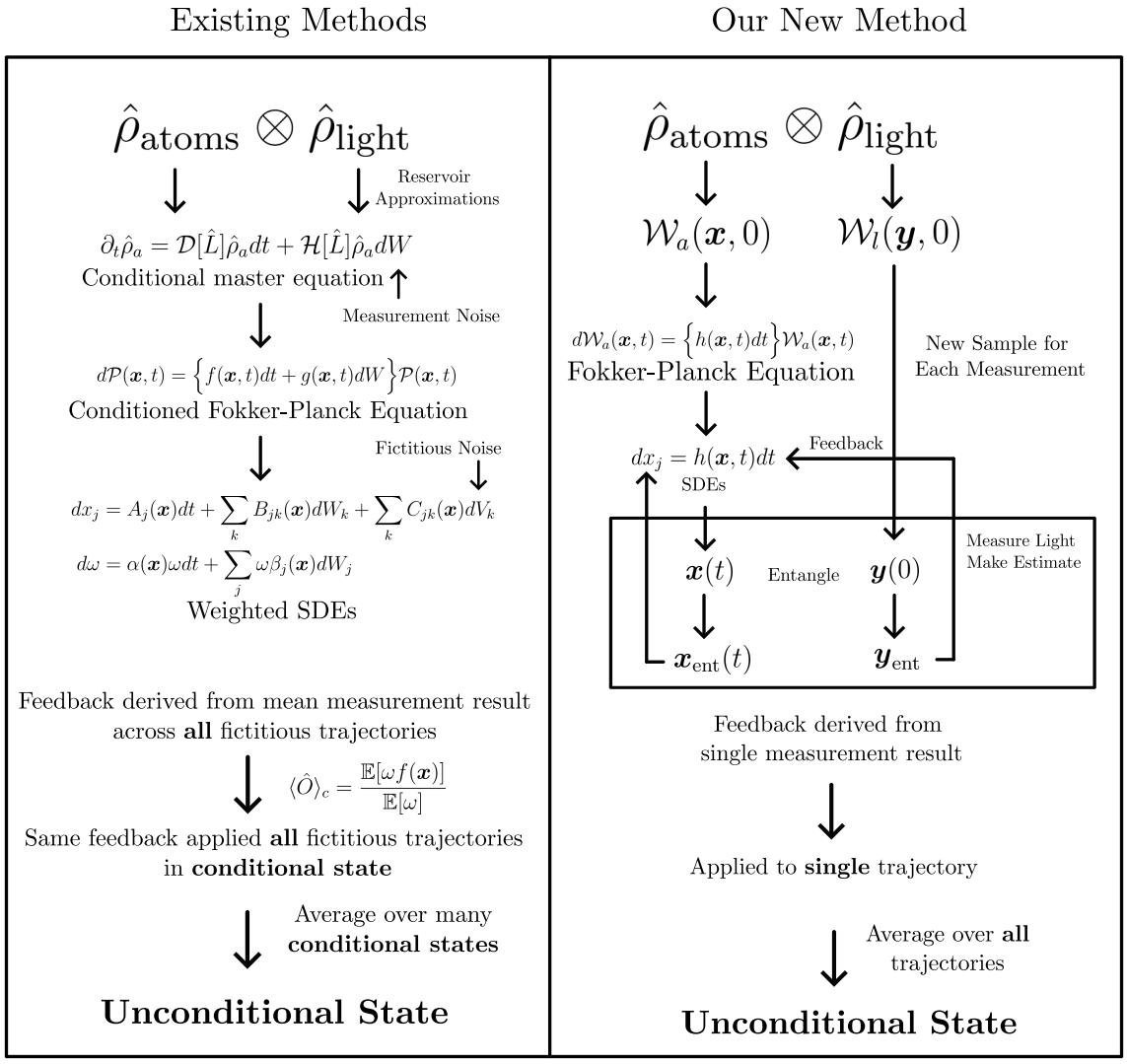

Figure 3.1: **A flowchart depicting the simulation process of conditioned quantum. There are two key distinctions: Existing methods modeled continuous measurements, and the light is traced out at the level of the master equation, leading to a reduced conditional master equation for the atomic state. In our method, the light is explicitly kept in. Secondly, existing methods simulate evolution of conditional states and recover unconditional dynamics by averaging over all conditional states, while our method simulates the unconditional state directly.**

[5] In other words, once the photon hits our detector and is destroyed.

3.1.4 Questions To Be Answered

The entire purpose of this chapter is to determine the regime of validity of our new approach. Specifically, whether the individual treatment of Wigner trajectories reproduces the correct quantum statistics when averaged over realisations of the experiment. Here are some questions:

1. Experimentally, a single measurement conditions an *entire* quantum state. In NPW, each result is applied to an ensemble of fictitious trajectories representing the conditioned state. In our method, only *single* trajectories are conditioned. By themselves, they are not valid representations of any conditional state. Does the mean behaviour across all trajectories correctly represent an unconditioned state?

2. For what regimes and scenarios is the conclusion to the first question valid? Specifically, feedback cooling takes a incoherent thermal mixture to a phase-coherent condensed state. Is our method able to capture this phase-transition?

3. What is the correspondence between our method and NPW?

We will revisit these questions at the end of the chapter.

3.2 Two-Mode Many-Body Systems

3.2.1 The SU(2) Subspace

As described in Chapter 2, the underlying algebraic space for a many-body system with variable particle number is the Fock space. For a system with *fixed* total number M, the Fock space reduces to the tensor product of M single-particle Hilbert spaces. Furthermore, if the number of accessible modes is finite and denoted N, then the structure of the (sub)space is characterised by the SU(N) group and corresponding Lie algebra. An excellent discussion of the topic is provided in [70].

For a two-mode system, let us denote the annihilation operators for each mode as $\hat{a}_1$ and $\hat{a}_2$. These satisfy the standard bosonic commutation relations:

$$[\hat{a}_i, \hat{a}_j] = \left[\hat{a}_i^\dagger, \hat{a}_j^\dagger\right] = 0, \quad \left[\hat{a}_i, \hat{a}_j^\dagger\right] = \delta_{ij} \tag{3.5}$$

where $i, j \in \{1, 2\}$. Analogous to the angular momentum operators for a spin-$1/2$ particle, we may equivalently define a set of Hermitian 'pseudo-spin' operators:

$$\hat{J}_x = \frac{1}{2}\left(\hat{a}_1^\dagger \hat{a}_2 + \hat{a}_2^\dagger \hat{a}_1\right), \quad \hat{J}_y = \frac{i}{2}\left(\hat{a}_2^\dagger \hat{a}_1 - \hat{a}_1^\dagger \hat{a}_2\right), \quad \hat{J}_z = \frac{1}{2}\left(\hat{a}_1^\dagger \hat{a}_1 - \hat{a}_2^\dagger \hat{a}_2\right) \tag{3.6}$$

These operators satisfy the commutation relations for the Lie algebra of SU(2):

$$\left[\hat{J}_i, \hat{J}_j\right] = i\epsilon^{ijk}\hat{J}_k \qquad \text{where} \qquad i, j, k \in \{x, y, z\} \tag{3.7}$$

where ϵ^{ijk} is the anti-symmetric Levi-Civata symbol. Physically, the pseudo-spin operators may be interpreted as 'collective' spin operators[6]: For an ensemble of N spin $1/2$ particles, they act as the overall angular momentum operators of the ensemble. Dropping the spin analogy and considering an arbitrary two-mode system, the operators $\hat{J}_x$ and $\hat{J}_y$ now encode the phase coherences between the two modes, while $\hat{J}_z$ is the relative number difference. An arbitrary state in this space is conveniently represented on a Bloch sphere, where the axes are the pseudo-spin variables.

3.2.2 The Dicke Basis and Useful Quantum States

For N particles, the SU(2) subspace is spanned by $N + 1$ basis states. This is clear from the eigenvalues of $\hat{J}_z$, which span $-N/2$ to $N/2$ in integer increments. The eigenstates of $\hat{J}_z$ are known as *Dicke* states [5] and furnish a convenient basis choice. We denote the n'th Dicke state as:

$$|n\rangle \equiv \left|\frac{N}{2} - n, \frac{N}{2} + n\right\rangle \quad -\frac{N}{2} \leq n \leq \frac{N}{2} \tag{3.8}$$

The second ket above is written in second quantised notation, and denotes the state with $N/2 - n$ and $N/2 + n$ particles in each mode. Now we introduce the two quantum states we will use in our comparisons, starting with the *Coherent Spin State* (CSS). Consider the state of a single two-mode particle ($|\psi\rangle$), parameterised by the Bloch sphere angles θ and

[6] Mathematically, they are the generators of the $\mathfrak{su}(2)$ algebra in the adjoint representation. The exponential map takes us to $SU(2)$, group of rotations etc.

ϕ. The most general form for $|\psi\rangle$ is given by[7]:

$$\begin{aligned}|\psi\rangle &= \sin\left(\frac{\theta}{2}\right)|1,0\rangle + \cos\left(\frac{\theta}{2}\right)e^{i\phi}|0,1\rangle \\ &= \left[\sin\left(\frac{\theta}{2}\right)\hat{a}_1^\dagger + \cos\left(\frac{\theta}{2}\right)e^{i\phi}\hat{a}_2^\dagger\right]\{|0\rangle\}\end{aligned} \tag{3.9}$$

The CSS is simply the tensor product of N copies of $|\psi\rangle$:

$$\begin{aligned}|\alpha(\theta,\phi)\rangle &= \frac{1}{\sqrt{N!}}|\psi\rangle^{\otimes N} \\ &= \sum_{n=-N/2}^{N/2}\binom{N}{N/2+n}\sin\left(\frac{\theta}{2}\right)^{\frac{N}{2}-n}\cos\left(\frac{\theta}{2}\right)^{\frac{N}{2}+n}e^{-i(\frac{N}{2}-n)\phi}|n\rangle \\ &\equiv \exp\left(i\phi\hat{J}_z\right)\exp\left(i\theta\hat{J}_x\right)|n=N/2\rangle\end{aligned} \tag{3.10}$$

Where the final line may be derived by representing 2.9 in terms of rotation operators generated by the pseud-ospin operator [5]. The CSS is the SU(2) analogue of a coherent state: It is a completely separable state and hence exhibits no entanglement, and we may interpret it as an extremely 'classical' state.

The CSS is a pure state. In the language of feedback cooling, pure states may only describe systems at zero temperature. Realistically, atomic ensembles always begin as finite-temperature incoherent thermal mixtures, undergoing a phase transition at the critical temperature during the condensation/cooling process [31]. Hence, we wish to also check whether our method is able to capture such transitions. However, Wigner negativity [71] constrains the choice of initial state, as only quantum states with positive Wigner functions may be accurately sampled. As the Wigner function of a thermal state is Hamiltonian dependent[8], the simplest choice for an incoherent state is the 'infinite temperature' limit, represented by the density matrix:

$$\hat{\rho} = \frac{\hat{\mathbb{1}}_D}{D} \tag{3.11}$$

where $\hat{\mathbb{1}}_D$ is the $D = N+1$'th dimensional identity operator. This is a maximal mixture of all possible (energy) eigenstates with no phase-coherence, aptly reflected in the zero off-diagonal elements. Its Wigner function has constant amplitude equal to $1/D$, and may be sampled as an ensemble of trajectories with fixed amplitude and completely random phases.

Wigner functions of other quantum states that exhibit negativity (e.g Fock states or Kerr crescent states) may be sampled with approximate methods that recover correct statistical moments in the limit of large N [49, 57]. We will not consider these, as in practice, dynamics of the atomic state under T_c are well described using a coherent state approximation, and we will use the Stochastic Projected Gross-Pitaevskii equation to generate samples of a thermal state.

[7]The notation $\{|0\rangle\}$ refers to the vacuum state.

[8]Hudson's theorem [56] guarantees that the Wigner function for a thermal state is always of Gaussian form. However, (moments of) the Wigner function will depend on the specific choice of Hamiltonian, which may very well be non-trivial to construct or sample.

3.3 The Coupled Quantum Anharmonic Oscillator

We now introduce the two-mode system we investigate: The Coupled Quantum Anharmonic Oscillator (CA). We stress that we are not overly concerned with the physics itself, as dynamics of very similar systems have been extensively studied in the past; in fact, the same Hamiltonian models the dynamics of atoms confined to a double-well potential [72, 73]. We have simply chosen this model as its Hamiltonian is similar to that of the multi-mode cold atom Hamiltonian, and yet it is sufficiently low-dimensional to allow an exact calculation. The Hamiltonian and master equation are presented below:

$$\begin{aligned}\partial_t\hat{\rho} &= -i\Big[\frac{\chi}{2}\Big((\hat{a}^\dagger\hat{a})^2 + (\hat{b}^\dagger\hat{b})^2\Big) + \kappa\Big(\hat{a}^\dagger\hat{b} + \hat{b}^\dagger\hat{a}\Big), \hat{\rho}\Big] \\ &\equiv -i\Big[\chi\Big(2\hat{J}_z^2 + \hat{N}_a\hat{N}_b\Big) + 2\kappa\hat{J}_x, \hat{\rho}\Big]\end{aligned} \tag{3.12}$$

where χ and κ are the (nonlinear) atom-atom interaction and coupling parameters, respectively, and $\hat{N}_i$ is the number operator for the i'th mode. To see the analogy, consider the cold-atom Hamiltonian of Eq. 2.21 in the discrete position basis:

$$\hat{H} = \sum_{\langle i,j\rangle}(c_{ij}\hat{a}_i^\dagger\hat{a}_j + c_{ij}^*\hat{a}_j^\dagger\hat{a}_i) + \frac{g}{2}\sum_i \hat{a}_i^\dagger\hat{a}_i^\dagger\hat{a}_i\hat{a}_i \tag{3.13}$$

Note that we have used $\hat{a}_i$ to refer to the operator that annihilates a particle at the position x_i. We see that the local interaction corresponds exactly to the nonlinear term, while the kinetic and potential energies transform into nearest-neighbour coupling terms analogous to the $\hat{J}_x$ term in 3.8. In fact, the CA system is just the two-mode truncation of the Bose-Hubbard model, which has also been studied in depth [74]. We explicitly note that the multi-mode Bose-Hubbard is not *physically* equivalent to the cold-atom system; the former is defined on a discrete lattice, while the latter is continuous in space. However, on a finite simulation basis, the two systems look identical.

We will now apply operator correspondences to first map Eq. 3.12 into a FPE, followed by a set of SDEs for the corresponding phase-space variables. Reprinting the operator correspondences for convenience:

$$\begin{aligned}\hat{a}\hat{\rho} &\leftrightarrow \Big(\alpha + \frac{1}{2}\frac{\partial}{\partial\alpha^*}\Big)\mathcal{W}(\alpha,\alpha^*) & \hat{a}^\dagger\hat{\rho} &\leftrightarrow \Big(\alpha^* - \frac{1}{2}\frac{\partial}{\partial\alpha}\Big)\mathcal{W}(\alpha,\alpha^*) \\ \hat{\rho}\hat{a} &\leftrightarrow \Big(\alpha - \frac{1}{2}\frac{\partial}{\partial\alpha^*}\Big)\mathcal{W}(\alpha,\alpha^*) & \hat{\rho}\hat{a}^\dagger &\leftrightarrow \Big(\alpha^* + \frac{1}{2}\frac{\partial}{\partial\alpha}\Big)\mathcal{W}(\alpha,\alpha^*)\end{aligned} \tag{3.14}$$

For instructional purposes, we demonstrate one correspondence explicitly. Consider the term $\hat{a}^\dagger\hat{a}$:

$$\begin{aligned}\hat{a}^\dagger(\hat{a}\hat{\rho}) &\leftrightarrow \hat{a}^\dagger\Big(\alpha + \frac{1}{2}\frac{\partial}{\partial\alpha^*}\Big)\mathcal{W}(\alpha,\alpha^*) \\ &\leftrightarrow \Big(\alpha^* - \frac{1}{2}\frac{\partial}{\partial\alpha}\Big)\Big[\Big(\alpha + \frac{1}{2}\frac{\partial}{\partial\alpha^*}\Big)\mathcal{W}(\alpha,\alpha^*)\Big] \\ &\leftrightarrow \Big(|\alpha|^2 - \frac{1}{2}(\partial_\alpha\alpha - \alpha^*\partial_{\alpha^*}) - \frac{1}{4}\partial_\alpha\partial_{\alpha^*}\Big)\mathcal{W}(\alpha,\alpha^*)\end{aligned} \tag{3.15}$$

Eq. 3.12 produces the following equation of motion for the Wigner function:

$$\begin{aligned}\partial_t \mathcal{W}(\boldsymbol{\alpha},\boldsymbol{\beta}) = &\left(i\partial_\alpha\left(\frac{\chi}{2}(2|\alpha|^2-1)\alpha+\kappa\beta\right) - i\partial_{\alpha^*}\left(\frac{\chi}{2}(2|\alpha|^2-1)\alpha^*+\kappa\beta^*\right)\right.\\ &+ i\partial_\beta\left(\frac{\chi}{2}(2|\beta|^2-1)\beta+\kappa\alpha\right) - i\partial_{\beta^*}\left(\frac{\chi}{2}(2|\beta|^2-1)\beta^*+\kappa\alpha^*\right)\\ &- i\frac{\chi}{4}(\partial_\alpha\partial_\alpha\partial_{\alpha^*}\alpha - \partial_{\alpha^*}\partial_{\alpha^*}\partial_\alpha\alpha^*)\\ &\left.- i\frac{\chi}{4}(\partial_\beta\partial_\beta\partial_{\beta^*}\beta - \partial_{\beta^*}\partial_{\beta^*}\partial_\beta\beta^*)\right)\mathcal{W}(\boldsymbol{\alpha},\boldsymbol{\beta})\end{aligned} \tag{3.16}$$

Next, we apply the Truncated Wigner Approximation (TWA) and discard higher order ($n \geq 3$) derivative terms. The equation is now of Fokker-Planck form, and may be further mapped to the following set of SDEs:

$$\begin{aligned}\partial_t\alpha &= -i\left(\frac{\chi}{2}(2|\alpha|^2-1)\alpha+\kappa\beta\right)\\ \partial_t\beta &= -i\left(\frac{\chi}{2}(2|\beta|^2-1)\beta+\kappa\alpha\right)\end{aligned} \tag{3.17}$$

where the phase-space variables α and β correspond to the operator averages $\alpha = \langle\hat{a}\rangle_\rho$ and $\beta = \langle\hat{b}\rangle_\rho$, respectively. We make two observations: Firstly, Eq. 3.12 is of Von-Neumann form; it contains only Hamiltonian evolution and no Lindblad superoperators. Hence, second-order derivative terms are absent in the resulting FPE, and the SDEs evolve deterministically with stochastically sampled initial conditions. Secondly, let us write out Heisenberg's equations of motion for the annihilation operators $\hat{a}$ and $\hat{b}$:

$$\begin{aligned}\partial_t\hat{a} &= -i\left(\frac{\chi}{2}(2\hat{a}\hat{a}^\dagger-1)\hat{a}+\kappa\hat{b}\right) \equiv -i\left(\frac{\chi}{2}(2\hat{a}^\dagger\hat{a}+1)\hat{a}+\kappa\hat{b}\right)\\ \partial_t\hat{b} &= -i\left(\frac{\chi}{2}(2\hat{b}\hat{b}^\dagger-1)\hat{b}+\kappa\hat{a}\right) \equiv -i\left(\frac{\chi}{2}(2\hat{b}^\dagger\hat{b}+1)\hat{b}+\kappa\hat{a}\right)\end{aligned} \tag{3.18}$$

Comparison of Eq. 3.17 and Eq. 3.18 reveals much about the truncated terms: The equations are identical under the replacement of $\hat{a} \to \alpha$ and $\hat{b} \to \beta$. In other words, in the absence of decoherence, single trajectories of the TWA simply follow mean-field dynamics[9]. Furthermore, we may also assign physical meaning to the truncated terms: They correspond to the 'quantumness' arising from operator non-commutativity encoded in the Heisenberg equations.

The TWA is an *uncontrolled* approximation. In general, it is not possible to quantify its regime of validity, as this would require a benchmark obtained from either from integrating the *entire* FPE, which is impossible in many-body multi-mode systems where one would employ the TWA in the first place. Regardless, there are are heuristic guidelines: The TWA generally performs well for modes with large occupations (i.e the semi-classical limit), where half-quanta quantum fluctuations are negligible compared to the (coherent state) amplitude of each mode [75]. Much work has gone into establishing more quantitative bounds; we refer the reader to [55, 76] for further discussion.

[9] If this is unclear, apply the coherent state approximation to Eq. 3.18 in the same way we did in Section 2.2.1

3.4 Dynamics: Absence of Measurement and Feedback

We first investigate the free dynamics of the coupled oscillator system. This allows us to identify parameter ranges for which the TWA produces accurate predictions via comparison with a direct integration of the master equation (Eq. 3.12). Figure 3.2 shows the first two moments of $\hat{J}_z$ over time for an initial coherent state with $\langle \hat{a}^\dagger \hat{a} \rangle = 40$ and $\langle \hat{b}^\dagger \hat{b} \rangle = 60$ across a range of couplings and nonlinearities.

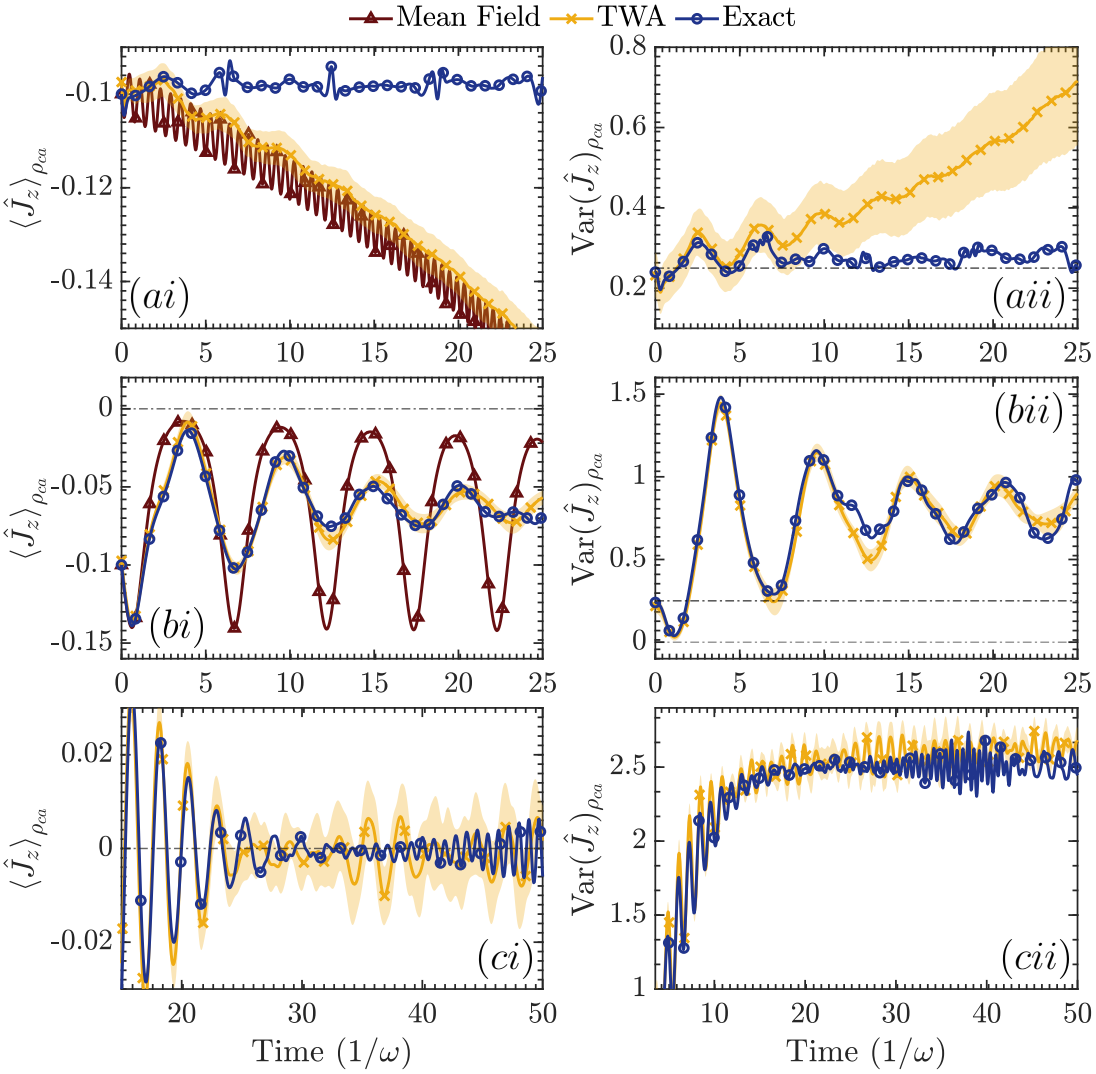

Figure 3.2: Evolution of the mean and variance of the pseudo-spin observable $\langle \hat{J}_z \rangle$ for the coupled quantum anharmonic oscillator over a range of different nonlinearities (χ) and coupling strengths (κ). The initial state was chosen to be a coherent state in both modes with $\langle \hat{a}^\dagger \hat{a} \rangle = 40$ and $\langle \hat{b}^\dagger \hat{b} \rangle = 60$. The TWA (4.12) is plotted with (yellow) crosses, a direct integration of the master equation (4.8) is plotted with (blue) circles, and when informative, the mean-field solution is plotted with (red) triangles. TWA solutions are bounded by a bootstrapped 2σ confidence interval shaded in yellow. Plots (a), (b), and (c) show simulations with $\chi/\kappa = 10$ (strong non-linearity), $\chi/\kappa = 1$ (balanced), and $\chi/\kappa = 0.2$ (strong coupling), respectively. The variance in $\hat{J}_z$ for a CSS on the equator ($N/4$) is plotted with dashed lines in (aii) and (bii). TWA simulations were performed with 1000 trajectories, and $\langle \hat{J}_z \rangle$ has been normalised by its maximal value of $N/2$.

We see that the TWA solution[10] agrees with the exact integration for the longest interval in the regime where coupling and nonlinearities are balanced (bi, bii). This is true for both moments, and there is no notable difference for the timescale in which the solutions match. We checked the accuracy of our results by consecutively lowering the simulation timestep until no further discrepancy was observed in the moments for successive timesteps. Clearly, the predictions of the mean-field solutions are generally poor, but most notably in the strongly nonlinear regime. This is expected due to complete neglect of quantum correlations generated by the nonlinear interactions. The TWA solution performs marginally better in short timescales, redeemed by its superior initial state sampling, but ultimately succumbs to the same fate due to the truncation of higher order terms.

In the strong coupling limit (ci, cii), the TWA once again performs well throughout the transient period where $\hat{J}_z$ oscillations are quickly damped. However, it is unable to quantitatively predict the coherent rephasing of the long-term behaviour which leads to a revival in $\hat{J}_z$ oscillation. For the purposes of feedback, the breakdown of TWA for long-term coherence induced dynamics should not be an issue, as they should be suppressed by our feedback anyways.

In summary, the accuracy of the TWA degrades most rapidly for strong nonlinearities which rapidly evolve the state towards highly exotic entangled regimes where the Wigner function almost certainty exhibits negativity, and can not be accurately represented by trajectories. In addition, TWA is unable to predict dynamics such as quantum revivals, which arise from coherent rephasing of the state; during which time, the Wigner function passes through negativity, which can not be captured by trajectories [72]. For our purposes of benchmarking, we simply choose parameters which lead to non-trivial dynamics, yet still remain in the regime of validity of TWA, such that the application of feedback should not lead to any exotic or badly represented quantum state.

3.5 Measurement as Entanglement

3.5.1 Implementing Measurement: Truncated Wigner

Our system is an ensemble of N two-mode atoms, and our measurement probe is a single-mode optical field in a coherent state. We make estimates of $\hat{J}_z$ by first entangling the light and atomic system, producing correlations between the $\hat{J}_z$ observable and phase quadrature of the light $(\hat{Y})$. We make a projective measurement of $\hat{Y}$ which destroys the light, but provides information about $\hat{J}_z$ and collapses (projects) the atomic system towards a $\hat{J}_z$ eigenstate. Stronger measurement (i.e optical intensity) produces more accurate estimates at the expense of stronger backaction.

For clarity, we relabel the two atomic modes as $\hat{a}_1$ and $\hat{a}_2$ and denote the bosonic operator for the light as $\hat{b}(t)$. This is a 'flux'-like operator, in the sense that the total photon number

[10] Important Note: A coherent state exhibits number fluctuations, whereas a CSS has fixed particle number. In order to make fair comparisons, the phase-space variables are manually normalised post-sampling such that $|\alpha|^2 + |\beta|^2 = N$. The consequence is that particular moments will always differ slightly between the TWA and SU(2). In fact, this is true for *all* initial states, and is an unavoidable consequence of trying to make comparisons between the SU(2) subspace and the entire Fock space. Fortunately, this discrepancy is minimal, systematic (so remains roughly constant), and decreases for larger N.

operator over a period of time is given by its time integral. The interaction Hamiltonian and post-interaction state may be expressed as:

$$\hat{H}_I(t) = \frac{\hbar\lambda}{t_p}\left(\hat{J}_z \otimes \hat{b}^\dagger(t)\hat{b}(t)\right) \qquad |\Psi(t+t_p)\rangle = \underbrace{\exp\left(-\frac{i}{\hbar}\int_t^{t_p} dt'\, \hat{H}_I(t')\right)}_{\hat{U}_I(t_p)} |\Psi(t)\rangle \tag{3.19}$$

where λ and t_p are the measurement strength and duration of the laser pulse, respectively. In practice, the measurement timescale is significantly shorter than that of the natural atomic dynamics, so it is justified to model the measurement pulse independently of Hamiltonian evolution. Furthermore, it has been shown in [77–79] that the atomic state after the application of $\hat{U}_I(t_p)$ is well approximated as an instantaneous measurement process, which transforms $\hat{b}(t) \to \hat{b}$. As we are not particularly concerned with the atomic dynamics during the measurement sequence, we will adopt this treatment for the remainder of this thesis. Writing out Heisenberg's equations of motion under $\hat{H}_I$ produces the following expressions:

$$\begin{aligned}
\partial_t \hat{a}_1 &= i\frac{\lambda}{4t_p}\left(1 - 2\hat{b}^\dagger\hat{b}\right)\hat{a}_1 \\
\partial_t \hat{a}_2 &= -i\frac{\lambda}{4t_p}\left(1 - 2\hat{b}^\dagger\hat{b}\right)\hat{a}_2 \\
\partial_t \hat{b} &= -i\frac{\lambda}{2t_p}\left(\hat{a}_1^\dagger\hat{a}_1 - \hat{a}_2^\dagger\hat{a}_2\right)\hat{b} \equiv -i\frac{\lambda}{t_p}\hat{J}_z \otimes \hat{b}
\end{aligned} \tag{3.20}$$

By construction, the operators are constant under the instantaneous measurement. Hence, Eq. 3.20 may be directly integrated to obtain input-output relations for the operators[11]. In addition, as entanglement only generates unitary dynamics, we may replace the operators with their phase-space counterparts directly to obtain:

$$\begin{aligned}
\alpha_{1_{\text{out}}} &= \exp\left(i\frac{\lambda}{4}\left(1 - 2|\beta_{\text{in}}^2|\right)\right)\alpha_{1_{\text{in}}} \\
\alpha_{2_{\text{out}}} &= \exp\left(-i\frac{\lambda}{4}\left(1 - 2|\beta_{\text{in}}^2|\right)\right)\alpha_{2_{\text{in}}} \\
\beta_{\text{out}} &= \exp\left(-i\lambda\mathcal{J}_z\right)\beta_{\text{in}}
\end{aligned} \tag{3.21}$$

where $\mathcal{J}_z = (|\alpha_{1_{\text{in}}}|^2 - |\alpha_{2_{\text{in}}}|^2)/2$, and the subscripts 'in' and 'out' refer to prior and post measurement, respectively. Eq. 3.21 clearly show the effects of measurement backaction: The (noise in the) light (β_{in}) appears in the phase of the atoms (α_1, α_2), while the number difference ($\mathcal{J}_z$) is imprinted onto the phase of the light. For strong intensities, the light is well-described as a coherent state with amplitude $\langle\hat{b}^\dagger\hat{b}\rangle = \langle N_b\rangle = \beta_0$, where $\langle N_b\rangle$ is the average total number of photons contained in each measurement pulse. In terms of Wigner trajectories, we may set β_0 to be real without loss of generality and sample $\beta_{\text{in}} = \beta_0 + \eta$, where η is a complex Gaussian noise with mean correlations $\overline{\eta^*\eta} = 1/2$ [57].

Note that the *entirety* of $|\beta_{\text{in}}|^2$ is included in the backaction phase applied to the atomic variables in Eq. 3.17. As $|\beta_0| \gg |\eta|$, this amounts to applying a large, constant phase shift upon every measurement. Experimentally, we may easily account for this phase

[11] See that the t_p has vanished in the following set of expressions; by treating measurement as instantaneous, we have essentially integrated over the measurement duration.

shift by including a global phase rotation in the atomic Hamiltonian. Henceforth, we use 'backaction phase' to explicitly refer to the phase associated with the quantum noise in the light. The entanglement process is visualised in terms of Wigner trajectories in Fig. 3.3 below.

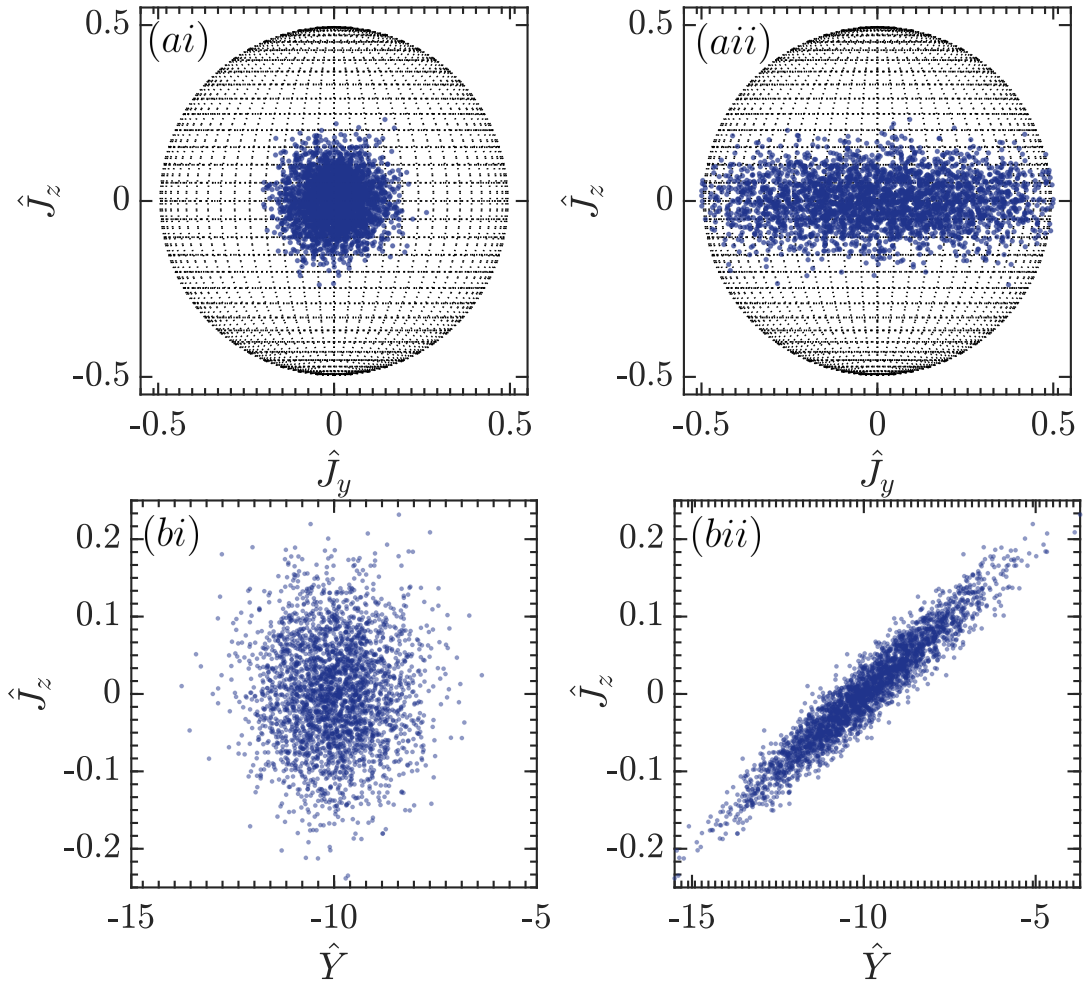

Figure 3.3: Measurement backaction visualised with Wigner trajectories for a coherent spin state with $\langle \hat{a}_1^\dagger \hat{a}_1 + \hat{a}_2^\dagger \hat{a}_2 \rangle = 50$. In (ai) (prior to measurement) and (aii) (unconditional post measurement state), each (blue) scatter point represents a *single* Wigner trajectory with (α_1, α_2) stochastically sampled (a total of 5000 times). Each pair of (α_1, α_2) have been mapped into pseudo-spin observables and represented on the Bloch sphere. In (aii), a measurement of $\hat{J}_z$ has been made. Each trajectory is 'measured' with a stochastic light variable, (β_{in}), and transformed according to Eqs. 3.20. The effects of backaction are clear: The phase of each atomic trajectory has been scrambled, so the variances of the conjugate observables ($\hat{J}_x$ and $\hat{J}_y$) have increased, but the variance of $\hat{J}_z$ remains unchanged. The correlations between $\hat{J}_z$ and the (measured) phase quadrature of the light are shown in (bi) and (bii). See that correlations only exist *post*-measurement, as the atomic and light variables are now entangled. Crucially, note that the noise in the light ensures that a single measurement result of $\hat{Y}$ may correspond to multiple atomic trajectories ($\hat{J}_z$) and vice versa, such that the unconditional post measurement state (aii) has correct statistics.

3.5.2 The Measurement Signal, the Continuous Limit, and Filtering Theory

The measurement signal is always the phase quadrature of the output light field, defined as $\hat{Y}_{\text{out}} = i(\hat{b}_{\text{out}} - \hat{b}^\dagger_{\text{out}})$. These measurements are commonly performed through methods such as homodyne detection [80, 81], where the output field is mixed with a large, coherent local oscillator in order to observe interference information. In practice, the local field is generally derived from the same source as the probing light in order to realise a coherent phase reference. We refer the reader to [82] for more details on experimental implementation. Recasting $\hat{Y}$ into phase-space variables and using Eqs. 3.21, we find:

$$\begin{aligned}\mathcal{Y} &= i(\beta_{\text{out}} - \beta^*_{\text{out}}) \\ &= i\left(e^{-i\lambda\mathcal{J}_z}\beta_{\text{in}} - e^{i\lambda\mathcal{J}_z}\beta^*_{\text{in}}\right) \\ &\approx 2\beta_0\lambda\mathcal{J}_z + 2\,\text{Im}\,\{\eta\}\end{aligned} \tag{3.22}$$

where we have assumed the small $\lambda\mathcal{J}_z$ limit, which is true in the weak measurement regime. We choose our estimate for $\mathcal{J}_z$ as $\mathcal{J}_{z_{\text{est}}} = \mathcal{Y}/2\beta_0\lambda$ though we are free to pick the functional form of $\mathcal{J}_{z_{\text{est}}}$ based on our choice of measurement signal.

In order to implement energy damping, our feedback is conditioned on the *derivative* of $\mathcal{J}_z$ (or in general, the measurement signal $\mathcal{Y}$). For discrete measurements, we may simply take finite differences:

$$V_{\text{fb}} \propto \frac{\mathcal{Y}(t+\Delta t) - \mathcal{Y}(t)}{\Delta t} = 2\beta_0\lambda\frac{\Delta\mathcal{J}_z}{\Delta t} + \frac{\Delta 2\,\text{Im}\{\eta\}}{\Delta t} \tag{3.23}$$

The first term on the RHS of Eq. 3.23 is our desired feedback signal. As we expect, it is larger for stronger measurement (λ). The second term is a real noise in our measurement signal derived from the quantum noise of the light, and is associated with stochastic measurement collapse. Let us consider the continuous measurement limit, where $\Delta t \to dt$. The noise $\text{Im}\,\{\eta\}$ transforms into a real Wiener noise[12] process dW. The second term of Eq. 3.23 becomes $\partial_t dW$. However, as the Wigner noise is differentiable nowhere[13], this term grows unbounded for smaller measurement intervals in numerical implementation.

The upshot is that the signal-to-noise ratio (SNR) of the feedback signal rapidly degrades for increasingly frequent measurements until it is entirely dominated by the measurement noise in the limit of continuous measurement. In practice, one must integrate the signal over a finite bandwidth and extract an estimate of the derivative through a polynomial fit of the resulting time series.

[12] Recall that η is a complex Gaussian noise with variance $1/2$ in both the real and imaginary quadratures, so $2\,\text{Im}\{\eta\}$ is a real Wiener noise with unit variance.

[13] Recall that the Wiener noise is continuous but *nowhere* smooth, so the derivative is formally ill-defined.

3.5.3 Implementing Measurement: Stochastic Schrödinger Equation

Now we describe the measurement process for an arbitrary quantum state represented by the density matrix $\hat{\rho}_A$. For a two-mode system, the dimensions of $\hat{\rho}_A$ scale as $\mathcal{O}(N^2)$, so a direct integration of the Schrödinger equation is tractable for small particle number ($N \sim 200$). This provides an exact solution against which we will benchmark our new approach. We start with the arbitrary mixed state:

$$\begin{aligned}\hat{\rho}_0 &= \hat{\rho}_A \otimes \hat{\rho}_L \\ &= \sum_{n,m=-N/2}^{N/2} \rho_{nm} \left|n\right\rangle\!\left\langle m\right| \otimes \left|\beta_0\right\rangle\!\left\langle\beta_0\right|\end{aligned} \tag{3.24}$$

where the light is initially in a pure coherent state with amplitude β_0, and we have expressed $\hat{\rho}_\mathrm{A}$ in the number basis. The combined density matrix of the atom-light system after the entanglement is no longer separable, and is given by:

$$\begin{aligned}\hat{\rho}' &= \hat{U}_I \hat{\rho} \hat{U}_I^\dagger \\ &= \sum_{n,m} \rho_{nm} e^{-i\lambda \hat{J}_z \hat{b}^\dagger \hat{b}} \left|n\right\rangle\!\left\langle m\right| \left|\beta_0\right\rangle\!\left\langle\beta_0\right| e^{i\lambda \hat{J}_z \hat{b}^\dagger \hat{b}} \\ &= \sum_{n,m} \rho_{nm} \left|n\right\rangle\!\left\langle m\right| \left|\beta_0 e^{i\lambda n}\right\rangle\!\left\langle\beta_0 e^{i\lambda m}\right|\end{aligned} \tag{3.25}$$

where $\hat{U}_I$ is the unitary operator generated by the interaction Hamiltonian in Eq. 3.19. The light is now in a superposition of coherent states $|\beta_0 e^{-i\lambda n}\rangle$[14], each correlated with a specific $|n\rangle$. The dependence on measurement strength is clear if one considers a 'stick-and-ball' phase-space diagram for each coherent state within the superposition: The entanglement has rotated each state by an angle λn. For strong entanglement (λ), different states in the superposition are separated by a larger angle such that their overlap is minimal. In this case, each coherent state[15] is strongly correlated with a specific $\hat{J}_z$ state.

At this stage, the combined quantum state $\hat{\rho}'$ is still unconditional as it has not been informed of the measurement result. To condition the state on a specific measurement result of the phase quadrature $\hat{Y}$, we project onto the corresponding $|y\rangle$ eigenstate:

$$\hat{\rho}_y = \frac{\hat{\Pi}(y)\hat{\rho}'\hat{\Pi}(y)}{\mathrm{Tr}\left\{\hat{\rho}'\hat{\Pi}(y)\right\}} \qquad \text{where} \qquad \hat{\Pi}(y) = \left|y\right\rangle\!\left\langle y\right| \tag{3.26}$$

The trace in the denominator is the likelihood of measuring a specific value of y and ensures normalisation of the conditional state. Explicitly computing the overlap between a coherent state and phase-quadrature eigenstate, we arrive at the following expression for conditioned state:

$$\hat{\rho}_y = \sum_{n,m} \rho_{nm} \left|n\right\rangle\!\left\langle m\right| \left|y\right\rangle\!\left\langle y\right| \left\langle y|\beta_0 e^{i\lambda n}\right\rangle \left\langle\beta_0 e^{i\lambda m}|y\right\rangle = \sum_{n,m} \rho'_{nm}(y) \left|n\right\rangle\!\left\langle m\right| \left|y\right\rangle\!\left\langle y\right| \tag{3.27}$$

[14] To see how this is true, first note that $e^{-i\lambda \hat{J}_z \hat{b}^\dagger \hat{b}} |n\rangle |\beta\rangle = |n\rangle e^{-in\lambda \hat{b}^\dagger \hat{b}} |\beta\rangle$. Expanding out $|\beta\rangle$ in terms of number states, we get: $e^{-|\beta|^2/2} \sum_m \beta^m/m! e^{-in\lambda \hat{b}^\dagger \hat{b}} |m\rangle = e^{-|\beta e^{-in\lambda}|^2} \sum_m (\beta e^{-in\lambda})^m/m! |m\rangle \equiv |\beta e^{-in\lambda}\rangle$.

[15] A small technicality: The correlations are developed between $\hat{J}_z$ and $\hat{Y}$. However, the logic still holds if one instead considers the projection of each coherent state onto the phase quadrature y-axis.

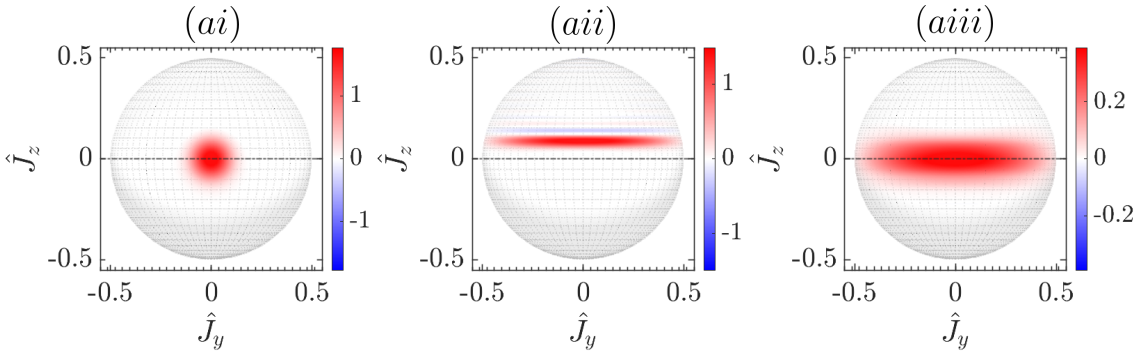

Figure 3.4: The Wigner function plotted on the surface of the Bloch sphere. (ai) A **pure** coherent spin state on the equator. (aii) The **pure** conditioned state following a *single* measurement of $\hat{J}_z$, which has been projected towards a $\hat{J}_z$ eigenstate. The measurement is relatively weak, so the resulting state is not a Fock state (which exhibits clear Wigner negativity) (aiii) The **mixed** unconditional state post measurement, obtained from averaging over an ensemble of different measurement results. See that the variance in $\hat{J}_x$ and $\hat{J}_y$ have increased due to backaction induced decoherence, but remains the same in $\hat{J}_z$. This is the hallmark of a QND measurement of $\hat{J}_z$.

where the new density matrix coefficients for the conditioned atomic state are given by:

$$\rho'_{nm}(y) = \frac{1}{\sqrt{\pi}}\rho_{nm}\exp\left(-\frac{1}{4}(y-2\beta_0\sin(\lambda n))^2\right)\exp\left(-\frac{1}{4}(y-2\beta_0\sin(\lambda m))^2\right) \tag{3.28}$$

In an experiment, we have now made a measurement of the light quadrature at the detector, and the photon is **destroyed**, so the light is no longer in the state $|y\rangle$. The probability of a specific measurement result is simply the sum over diagonal entries of $\hat{\rho}_y$:

$$P(y,t) = \mathrm{Tr}\left\{\hat{\rho}'\hat{\Pi}(y)\right\} = \sum_{n=-N/2}^{N/2}\frac{\rho_{nn}(t)}{\sqrt{\pi}}\exp\left(-\frac{1}{2}(y-2\beta_0\sin(\lambda n))^2\right) \tag{3.29}$$

As the probability distribution is time-dependent, it must be constructed prior to each measurement. In simulations, measurement results are obtained via stochastic sampling of $P(y)$. The Wigner functions of a CSS prior and post a weak measurement of $\hat{J}_z$ are shown in Fig. 3.4 above. See that the variances of both the conjugate pseudo-spin variables have increased in both the conditional (aii) and unconditional (aii) states due to backaction, though the unconditional state is centered on the mean measurement result of $\langle\hat{J}_z\rangle = 0$, much like the state represented by Wigner trajectories in Fig. 3.3 (aii). In addition, the unconditional variance of $\hat{J}_z$ remains unchanged, despite it being measured. These types of measurements are called Quantum Non-Demolition (QND) measurements [83], and are characterised entirely by the fact that no backaction is imparted on the the measured observable.

The interpretation of a 'trajectory' of the SSE is different to that of a sample of the Wigner trajectory. A single SSE trajectory is completely physical and corresponds to a single realisation of the experiment. Each trajectory is conditioned on a *different* measurement record, and the conditional quantum state is always well represented. In contrast, individual Wigner trajectories represent single samples of the Wigner function; they are single-valued, and hence physically ill-defined.

3.6 Implementing Feedback: Moment and Energy Damping

3.6.1 Choice of feedback control: Moment Control

Historically, studies of feedback cooling have primarily employed two choices for the control potential. The first is *moment-control*, where the feedback potential opposes and damps out oscillations in moments of observables such as the centre-of-mass position. Moment control was employed in the seminal study of feedback cooling by Haine *et al.* [26], where it was demonstrated that a control potential of the form:

$$V_C(\hat{x},t) = \left(c_1 \frac{d\langle\hat{x}\rangle}{dt}\right)\hat{x} + \left(c_2 \frac{d\langle\hat{x}^2\rangle}{dt}\right)\hat{x}^2 \tag{3.30}$$

where c_1 and c_2 are parameters to be optimised over, successfully extracted energy from the system. However, the system was also prone to reaching 'dark-states': These are non-stationary states which exhibit no oscillations in $\langle\hat{x}\rangle$ or $\langle\hat{x}^2\rangle$, so the feedback control is ineffective in removing further energy from the system. It was later showed showed that the inclusion of nonlinearities and measurement backaction was able to perturb the system out of dark states [84].

3.6.2 Choice of feedback control: Energy damping

More recent studies of feedback cooling have instead opted for an *energy-damping* control [2, 43], where the control potential damps out oscillations in the *atomic density*, rather than moments thereof. We will now show why this works. Consider the total Hamiltonian with feedback:

$$\hat{H} = \hat{H}_{\text{ca}} + \hat{V}_c, \qquad \langle E_0\rangle = \langle\hat{H}_{\text{ca}}\rangle \tag{3.31}$$

where $\hat{H}_{\text{ca}}$ and $\hat{V}_c$ are the cold-atom and feedback Hamiltonians, respectively. Using Ehrenfrest's theorem with Heisenberg's equation of motion for $\langle E_0\rangle$, we find:

$$\begin{aligned}
\partial_t\langle E_0\rangle &= \frac{i}{\hbar}\left\langle\left[\hat{H},\hat{H}_{\text{ca}}\right]\right\rangle \\
&= \frac{i}{\hbar}\left\langle\left[\hat{V}_c,\hat{H}_{\text{ca}}\right]\right\rangle \\
&= \frac{i}{\hbar}\left\langle\left[\hat{V}_c,\hat{H}-\hat{V}_c\right]\right\rangle \\
&= -\frac{i}{\hbar}\left\langle\left[\hat{H},\hat{V}_c\right]\right\rangle
\end{aligned} \tag{3.32}$$

Now, assume we choose our control potential to be of the form:

$$V_c(x,t) = -k_{\text{fb}}\nabla\cdot\langle\hat{j}(x,t)\rangle \equiv k_{\text{fb}}\partial_t\langle\hat{\rho}(x,t)\rangle \tag{3.33}$$

where $\hat{j}(x)$ is the particle current which obeys the continuity equation:

$$\hat{j}(x) = \frac{\hbar}{2mi}\left[\hat{\psi}^\dagger(x)(\nabla\hat{\psi}(x)) - (\nabla\hat{\psi}^\dagger(x))\hat{\psi}(x)\right], \qquad \nabla\cdot\hat{j}(x) + \partial_t\hat{\rho}(x) = 0 \tag{3.34}$$

Finally, substituting the control potential into Eq. 3.32 yields:

$$\begin{aligned}\frac{dE_0}{dt} &= -\frac{i}{\hbar}\left\langle\left[\hat{H}, \int dx\, \hat{\psi}^\dagger(x)\Big(-k_{\text{fb}}\nabla\cdot\big\langle\hat{j}(x)\big\rangle\Big)\hat{\psi}(x)\right]\right\rangle \\ &= -\int dx\, k_{\text{fb}}\frac{\partial\langle\hat{\rho}(x)\rangle}{\partial t}\left\langle\frac{i}{\hbar}\left[\hat{H}, \hat{\psi}^\dagger(x)\hat{\psi}(x)\right]\right\rangle \\ &= -k_{\text{fb}}\int dx\left(\frac{\partial\langle\hat{\rho}(x)\rangle}{\partial t}\right)^2 \leq 0 \end{aligned} \tag{3.35}$$

Hence, as long as there exist density fluctuations (which is guaranteed in the presence of measurement backaction [84]), energy damping is always able to extract energy from the system. In the discrete spatial mode basis, the feedback potential looks like:

$$\hat{V}_{\text{fb}}(\boldsymbol{x}, t) = \sum_n c_n(t)\hat{a}^\dagger(\boldsymbol{x}_n)\hat{a}(\boldsymbol{x}_n) \qquad \text{where} \qquad c_n(t) \propto \partial_t\langle\hat{N}_n\rangle \tag{3.36}$$

So we need to estimate the time-derivative of the atomic density in the spatial mode $\boldsymbol{x}_n$ from our noisy measurement signal. Note that at all times, the coefficients must satisfy $\sum_n c_n(t) = 0$ due to number conservation. In our two mode system, this implies $c_1(t) = -c_2(t)$ such that the feedback term is proportional to $\hat{J}_z$:

$$\hat{H}_{\text{fb}} = k_{\text{fb}}\partial_t(\hat{J}_{z_{\text{est}}})\hat{J}_z \tag{3.37}$$

Henceforth, we refer to feedback of this form as 'two-mode energy damping'.

3.7 Comparisons: New TWA and Exact SSE

3.7.1 Backaction in Conjugate Observables

We first look at the backaction due to a single measurement of $\hat{J}_z$. The variances of the conjugate observables ($\hat{J}_x$ and $\hat{J}_y$) post measurement as well as the the discrepancy between the actual and estimated $\hat{J}_z$ is plotted in Fig. 3.5 below, across a range of different measurement strengths.

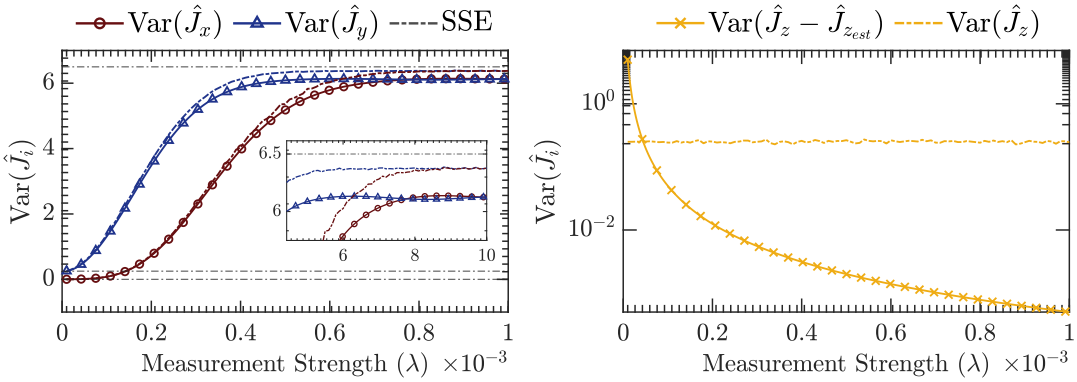

Figure 3.5: Variances of the unconditional conjugate pseud-ospin observables after a $\hat{J}_z$ measurement of a CSS on the equator over various measurement strengths (λ). (ai) Variances of $\hat{J}_x$ and $\hat{J}_y$ post measurement. TWA and SSE quantities are plotted in solid and dashed lines, respectively. (aii) The variance of the discrepancy between the actual and estimated $\hat{J}_z$ values.

As expected, the variances in the conjugate observables increase monotonically for stronger measurement strengths due to greater backaction, but remain unchanged for the measured observable $\hat{J}_z$: This is the hallmark of a QND measurement. The agreement between the TWA and exact method diverge for stronger measurements, but both are bounded above by the variance of $\hat{J}_x$ and $\hat{J}_y$ for the $n = 0$ $\hat{J}_z$ eigenstate[16] equal to $N(N+1)/2$.

This behaviour is expected, as stronger measurements increasingly project the state towards a $\hat{J}_z$ number eigenstate, whose Wigner functions exhibits negativity and hence can not be accurately sampled. Furthermore, the discrepancy tends to a constant value, which we attribute to the underlying incompatibility arising from the number conservation (and lack thereof) of the SU(2) subspace and TWA sampling, as described in Section 3.5.1. In our comparisons, we will take this discrepancy as an upper bound for the residuals between the TWA and SSE solutions, as we expect the error due to sampling (and negativity) to be most prominent for badly behave states. Fortunately, we see in (aii) that accurate estimates may still be made at weak measurement strengths, where Wigner sampling remains accurate.

[16] See this by computing $\langle \hat{J}_x^2 \rangle = \langle \hat{J}_y^2 \rangle = (\langle \hat{J}^2 \rangle - \langle \hat{J}_z \rangle^2)/2 = (N/2(N/2+1) - m^2)/2$.

3.7.2 Feedback Dynamics: Initial Coherent Spin State (CSS)

Now we look at the evolution of an initial CSS undergoing periodic $\hat{J}_z$ measurements subject to two-mode energy damping. The first three moments of the pseudo-spin variables, as well as dynamics in the absence of feedback are plotted below in Fig. 3.6 for an initial CSS where $\langle \hat{a}^\dagger \hat{a} \rangle_{\rho_{CA}} = 20$, and $\langle \hat{b}^\dagger \hat{b} \rangle_{\rho_{CA}} = 80$.

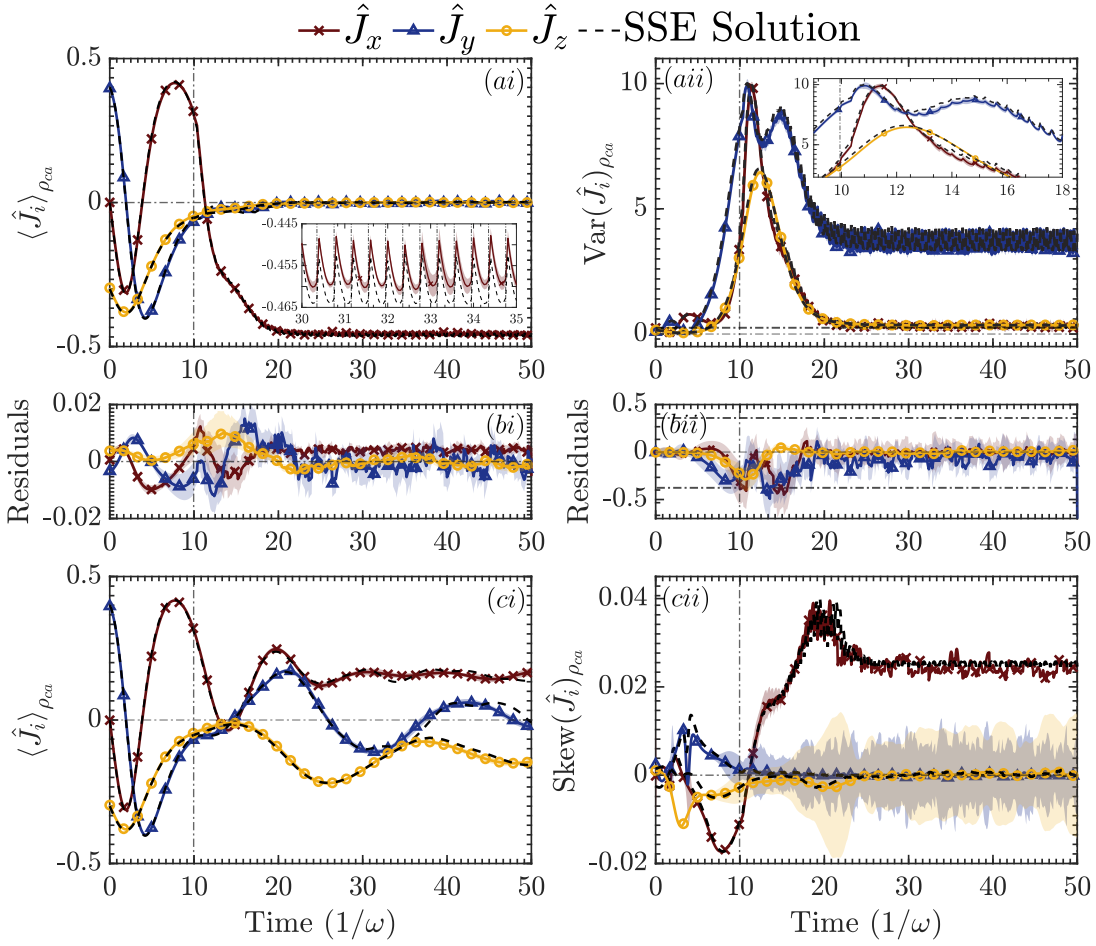

Figure 3.6: Dynamics of pseudospin observables for an initial CSS with $\langle \hat{a}^\dagger \hat{a} \rangle_{\rho_{CA}} = 20$, and $\langle \hat{b}^\dagger \hat{b} \rangle_{\rho_{CA}} = 80$ undergoing two-mode energy damping. All simulations were performed with parameters $\chi = 0.01, \kappa = 0.09, \lambda = 0.8 \times 10^{-4}$, and $k_{fb} = 0.1$. Feedback is turned on at the vertical dashed line corresponding to $t_{on} = t_{max}/5$. A total of 5000 Wigner trajectories and 3000 SSE trajectories were used, and a total of 100 measurements are made. The TWA solution is plotted in solid lines with markers, and the SSE solution is plotted with black dashed lines. (ai) Expectation values of the pseudospin observables. The inset zooms into the steady state behaviour, with each dashed line indicating a new measurement. (aii) Variance of the pseudospin observables. The inset shows the steady state behaviour of the $\hat{J}_x$ variance. The dashed lines indicate times of measurement: See that oscillations in variance peak at times of measurement, which is expected due to backaction. (bi), (bii) Residuals between the TWA and SSE solution for the first two moments, respectively. The shaded regions are 2σ-bootstrapped confidence intervals and are bounded by the SU(2) sampling error. (cii) Evolution of the pseudospin variables in the absence of feedback provided for comparison. (ci) The skewness of the pseudospin observables.

There are three sources of error between our comparisons. First is the sampling error due to the finite number of Wigner trajectories. Past some (empirically determined) threshold, increasing the number of trajectories only decreases the standard error in the mean dynamics, and *not* the accuracy of TWA. We refer to this as *Wigner sampling* error[17]. The second is due to the truncation of higher-order derivative terms within the TWA which we refer to as *truncation* error. The final error is associated with forcibly normalising the phase-space variable amplitudes, which arises due to the fundamental incompatibility between the number conserving SU2 subspace and Wigner sampling. We refer to this as *SU(2) sampling*.

We observe excellent agreement between the two solutions across both the first, second, and third order moments of the pseudospin variables in both the transient and steady state regimes. The residuals peak soon after the onset of feedback, which we initially attributed to the fact that the 'initial' state (in terms of Wigner trajectories) at t_{on} differs slightly from that of the exact solution due to truncation. However, we tried turning on feedback at $t_{\text{on}} = 0$, where there should be no truncation error, but observed similar results. Hence, we attribute this discrepancy to SU(2) sampling error.

Once feedback is turned on, the residuals rapidly diminish until the steady state is reached. This is expected, as the Wigner function of the steady state (computed directly from the density matrix) is entirely positive, and hence well represented by Wigner trajectories. Overall, no systematic discrepancy is observed in the residuals, and they all lie within the upper bound imposed by the SU(2) sampling error[18]. The initial, steady-state, and an intermediary Wigner function (constructed from the exact density matrix) and trajectories are plotted on the Bloch sphere in Fig 3.7 below.

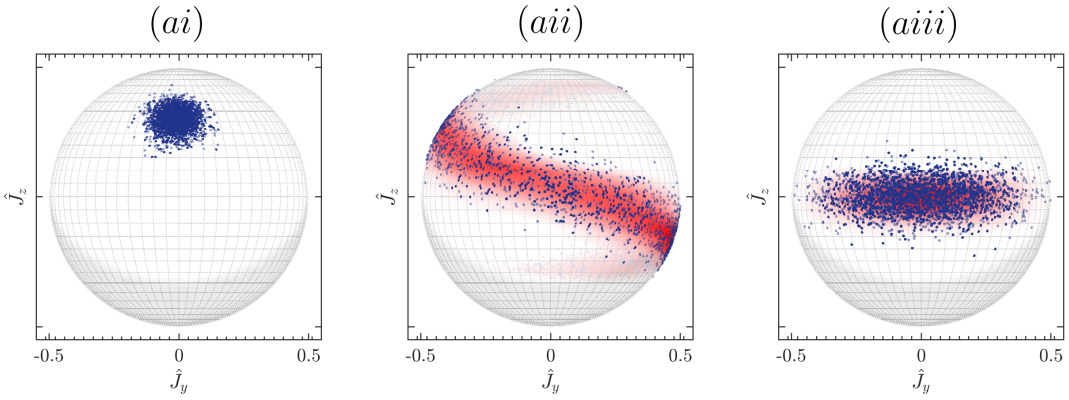

Figure 3.7: A CSS undergoing two-mode energy damping represented on the Bloch sphere at different times in terms of both Wigner trajectories and the SU(2) Wigner function. (ai) The initial state at $t = 0$. (aii) The state momentarily after feedback is turned on. (aiii) The steady-state. Note that this is *not* the ground eigenstate, but close to it.

[17]We will also use this to refer to scenarios where the Wigner function exhibits negativity, and hence may not be well represented with trajectories.

[18]Or contain the bound within the Wigner sampling confidence interval.

3.7.3 Feedback Dynamics: Incoherent Initial State (Infinite Temperature)

Next, we look at energy damping of an initially incoherent state. This is the closest analogue to the multi-mode feedback cooling of a BEC. We use the infinite temperature mixture as described in Section 3.2.2, where $\langle \hat{a}^\dagger \hat{a} \rangle_{\rho_{CA}} = \langle \hat{b}^\dagger \hat{b} \rangle_{\rho_{CA}} = 50$. The parameters used are the same as those in the case of the CSS, above. The same set of pseudospin variables are plotted in Fig. 3.8 below.

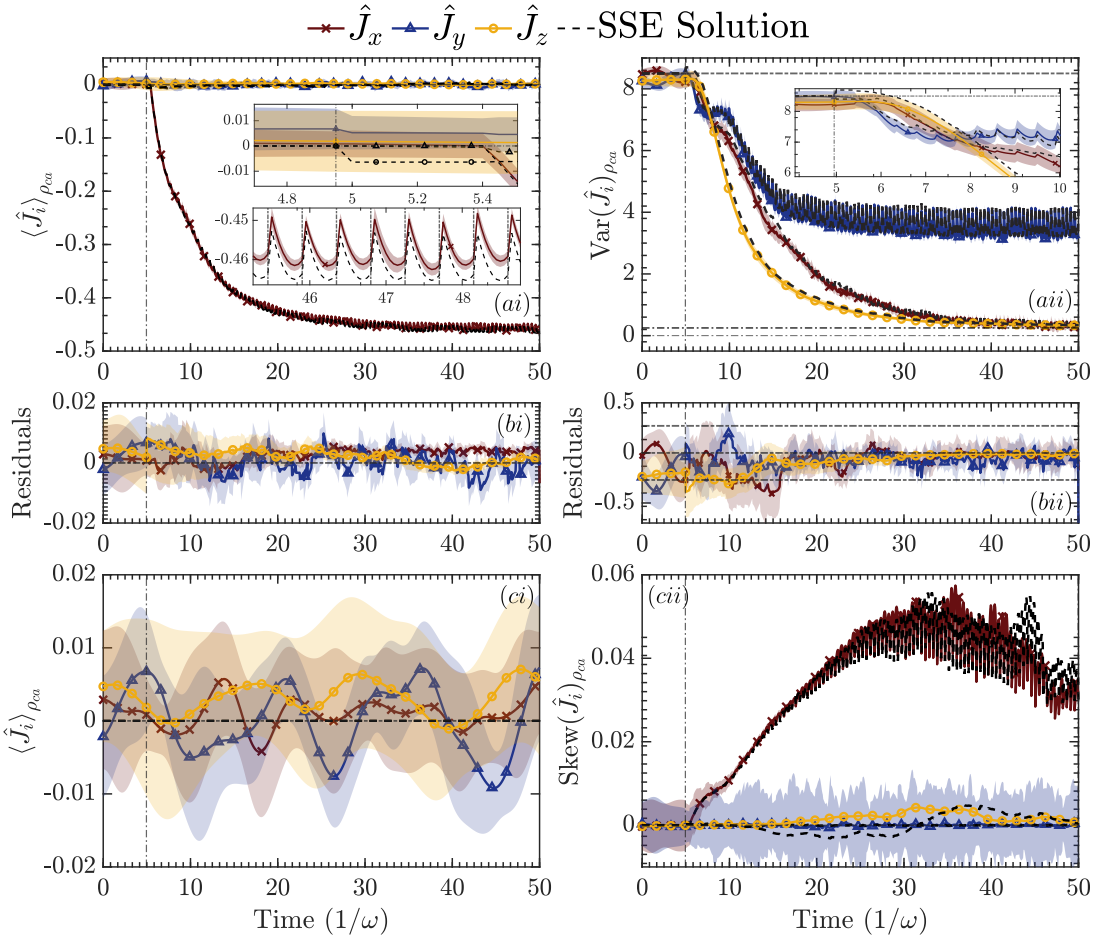

Figure 3.8: Dynamics of pseudospin observables for an initially incoherent infinite-temperature state with $\langle \hat{a}^\dagger \hat{a} \rangle_{\rho_{CA}} = 50$, and $\langle \hat{b}^\dagger \hat{b} \rangle_{\rho_{CA}} = 50$ undergoing two-mode energy damping. All simulations were performed with parameters $\chi = 0.01$, $\kappa = 0.09$, and $\lambda = 0.8 \times 10^{-4}$. Feedback is turned on at the vertical dashed line corresponding to $t_{on} = t_{max}/5$. A total of 5000 Wigner trajectories and 3000 SSE trajectories were used, and a total of 100 measurements are made. The TWA solution is plotted in solid lines with markers, and the SSE solution is plotted with black dashed lines. (ai) Expectation values of the pseudospin observables. (aii) Variance of the pseudospin observables. The first inset highlights the the initial discrepancy in the means due to SU(2) sampling error. (bi), (bii) Residuals between the TWA and SSE solution for the first two moments, respectively. The shaded regions are 2σ-bootstrapped confidence intervals, and are bounded by the SU(2) sampling error. (cii) Evolution of the pseudospin variables in the absence of feedback provided for comparison. The TWA solution fails to remain constant due to sampling error; the confidence interval is of the same magnitude as the oscillations, as expected. (ci) The skewness of the pseudospin observables.

Once again, we observe that the solutions exhibit excellent agreement with each other, with the residuals exhibiting no systematic discrepancy, and remain within the bounds of the SU(2) sampling error. It is especially promising to see that the agreement is maintained throughout the entirety of the transient region, as this is where we expect to observe the development of any phase coherence within the system. In multi-mode feedback cooling, the transient period contains the phase transition across the critical temperature, where the state transitions between an incoherent mixture and a condensed mode; we are hoping to be able to model this transition. In this two-mode model, this would look the growth of the two-mode condensate fraction, which we compute below.

In comparison to the CSS, the sampling error of the initial state is increased. This is expected, as the Wigner function of the infinite temperature states is constant everywhere. In order to capture the uniform density, a much greater number of trajectories is required. Otherwise, the sampling error manifests in initial oscillations of the moments, in contrast to the exact solution, where all moments remain constant until the onset of feedback. We conclude this section by looking at the system energy and two-mode condensate fraction, plotted in Fig. 3.9 below.

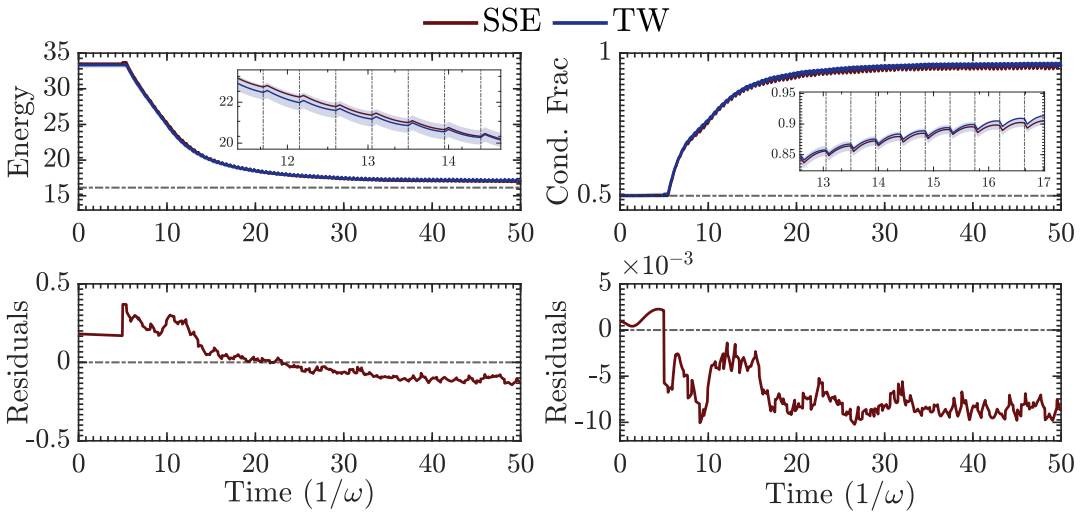

Figure 3.9: Time series plots of the system energy and two-mode condensate fraction for a system undergoing two-mode energy damping. The same parameters from Fig. 3.8 are used. The exact SSE and TW solutions are plotted in red and blue, respectively. (ai) Time series of the energy. The ground state energy of the system is plotted with a dashed line, and the vertical lines in the inset indicate measurements. (bi) Time series of the two-mode condensate fraction. For a two-mode system, it is bounded between $1/2 \leq f_{\text{cond}} \leq 1$. (bi)-(bii) The residuals between the two solutions for the energy and condensate fraction, respectively.

In (ai), we see that two-mode energy damping is very successful at extracting energy from the system; the steady-state energy approaches that of the ground-state energy. The heating due to measurement backaction is visible in the inset: The energy suddenly increases[19] after every measurement (dashed lines), before continuously decreasing due to feedback. The growth of the two-mode condensate fraction is illustrated in (bii). We see that the predictions of the TW and exact solutions agree well, which is a promising

[19]The discontinuous 'jump' is a consequence of instantaneous measurement.

sign that our method is able to correctly capture the dynamics of the appearance of phase coherence, as occurs in the BEC phase transition. In the inset, we see that the condensate fraction decreases after every measurement: This behaviour directly reflects the decohering nature of measurement. The feedback acts to *purify* the state, as it attempts to drive all conditional states towards the same attractor. No systematic discrepancy is observed in the residuals for either the energy or condensate fraction. In both cases, they tend to a roughly constant small value, which is consistent with what we expect from the SU(2) sampling error.

3.7.4 The Importance of Backaction and Noise

In the master equation, the state of the light is treated with a series of reservoir approximations [44] and traced out. We will now look at the the consequence of explicitly retaining the state of the light. First recall the uncertainty principle for the pseudospin observables:

$$\sigma_x \sigma_y \geq \frac{1}{2} |\langle \hat{J}_x \rangle| \tag{3.38}$$

Where σ_y and σ_z are the standard deviations of $\hat{J}_y$ and $\hat{J}_z$, respectively. The ratio $\sigma_x \sigma_y / |\langle \hat{J}_x \rangle|$, system energy, and steady state in terms of Wigner trajectories are plotted in Fig. 3.10 below.

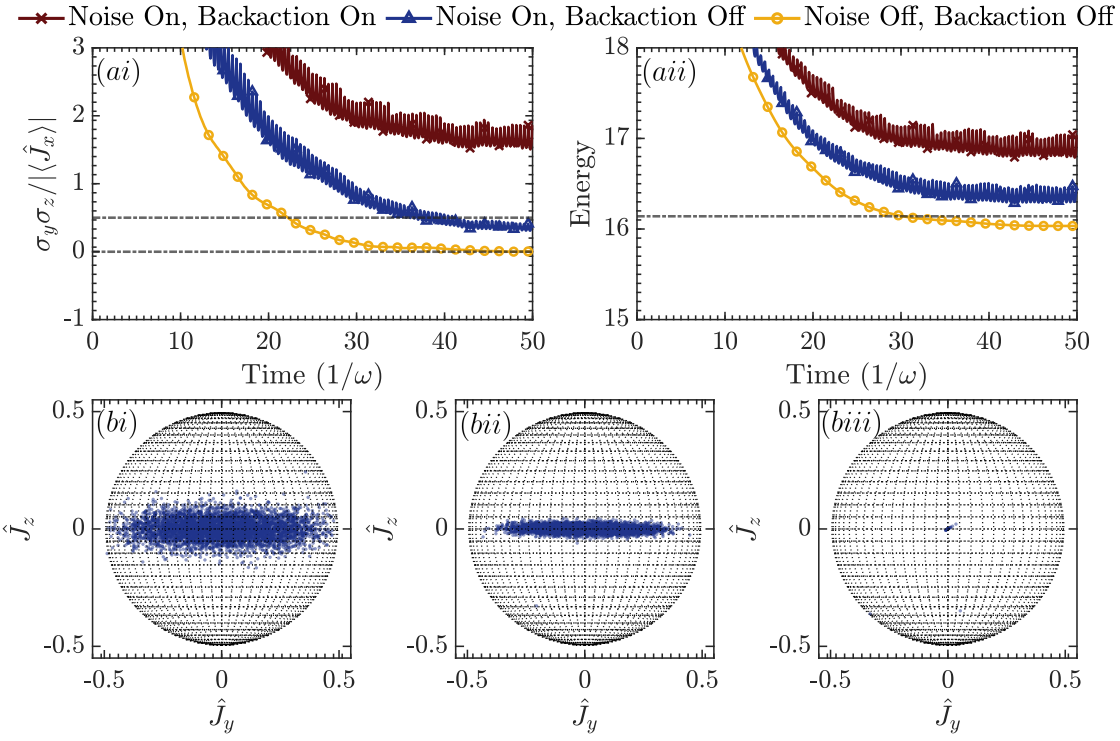

Figure 3.10: An investigation into the dependence of various quantities on the presence of light noise and measurement backaction.(ai) The ratio $\sigma_x \sigma_y / |\langle \hat{J}_x \rangle|$ from the uncertainty relation. The dashed line represents the Heisenberg bound of $1/2$. (aii) The system energy plotted in time. The dashed line represents the ground state energy. (bi)-(bii) The steady state of the system represented with Wigner trajectories. From left to right: Light noise and backaction on, light noise on, light noise and backaction off. Confidence intervals are not visible.

From 3.38, the ratio $\sigma_x\sigma_y/|\langle\hat{J}_x\rangle|$ is bounded below by $1/2$. In (ai), we see that the bound is ultimately violated if the backaction and/or noise in the light is turned off. This is a promising observation, as it indicates that the statistics and validity of the atomic state is guaranteed by our treatment of the light and measurement backaction. The steady state is visualised through Wigner trajectories in (bi)-(bii). Clearly, the 'state' in the absence of light noise and backaction is ill-defined as it approaches a singular point.

3.7.5 Dependence on Measurement Strength and Frequency

We have verified that our approach exhibits excellent agreement with an exact integration of the SSE. For feedback cooling, the key parameters of interest are the steady state excitation energy per particle and condensate fraction. The excitation energy per particle is defined as:

$$\Delta E_{\text{ss}} = \frac{E_{\text{ss}} - E_0}{N} \tag{3.39}$$

where E_{ss} and E_0 are the steady state and ground state energies of the system, respectively. Note that we only use ΔE_{ss} in place of E_{ss} when comparing systems with different particle numbers as they have different E_0, and use E_{ss} in all other cases. We use the Penrose-Onsager definition of condensate fraction [85], defined as the largest normalised eigenvalue (λ) of the one body density matrix (OBDM):

$$f_{\text{cond}} = \frac{\max_\lambda\left\{\rho^{\text{1B}}_{nm}\right\}}{\text{Tr}\{\rho^{\text{1B}}_{nm}\}} \qquad \text{where} \qquad \rho^{\text{1B}}_{nm} = \langle\hat{a}_n^\dagger\hat{a}_m\rangle = \text{Tr}\left\{\hat{a}_n^\dagger\hat{a}_m\hat{\rho}\right\} \tag{3.40}$$

Here, $\hat{a}_n$ denotes the annihilation operator for the n'th mode in the spectral basis[20]. In the two-mode reduction, the analogous one-body density matrix is given by:

$$\rho^{\text{1D}}_{\text{2M}} = \left\langle\begin{bmatrix}\hat{N}_{a_1} & \hat{J}_+\\ \hat{J}_- & \hat{N}_{a_2}\end{bmatrix}\right\rangle \qquad \text{where} \qquad \hat{J}_+ = \hat{a}_1^\dagger\hat{a}_2, \qquad \hat{J}_- = \hat{a}_2^\dagger\hat{a}_1 \tag{3.41}$$

The two-mode 'condensate fraction' is somewhat trivial and bounded below by $f_{\text{cond}} = 1/2$[21]. Regardless, it still represents an increase in coherence, and should still increase under successful feedback cooling even in the two-mode limit.

We have already seen in Eq. 3.21 that measurement scrambles the phases of across different modes of the atomic state[22], generating a phase-gradient across different atomic modes which corresponds to heating [86]. The steady-state of feedback cooling is reached when the cooling rate due to feedback is counterbalanced by the measurement-induced heating rate. We expect the steady-state energy and cooling rate to depend on three parameters: The measurement strength (λ), measurement frequency[23], and gain parameter (k_{fb}). We will now provide a qualitative demonstration of this dependence. The energy and two-mode condensate fraction are illustrated below in Fig. 3.11 for a range of different measurement strengths and rates.

[20] For feedback cooling, we use the harmonic oscillator eigenbasis of Hermite-Gauss modes.

[21] See this from the definition of f_{cond} in (3.44): For a M-mode system, the maximally mixed OBDM must have identical diagonal entries equal to $1/M$ due to trace-normalisation.

[22] We say 'scramble' as the imprinted phase is due to the spatial variance of the light intensity, which is therefore stochastic in a given realisation.

[23] Measurement frequency is equivalently parameterised by the total number of measurements made during the feedback period (N_{meas}).

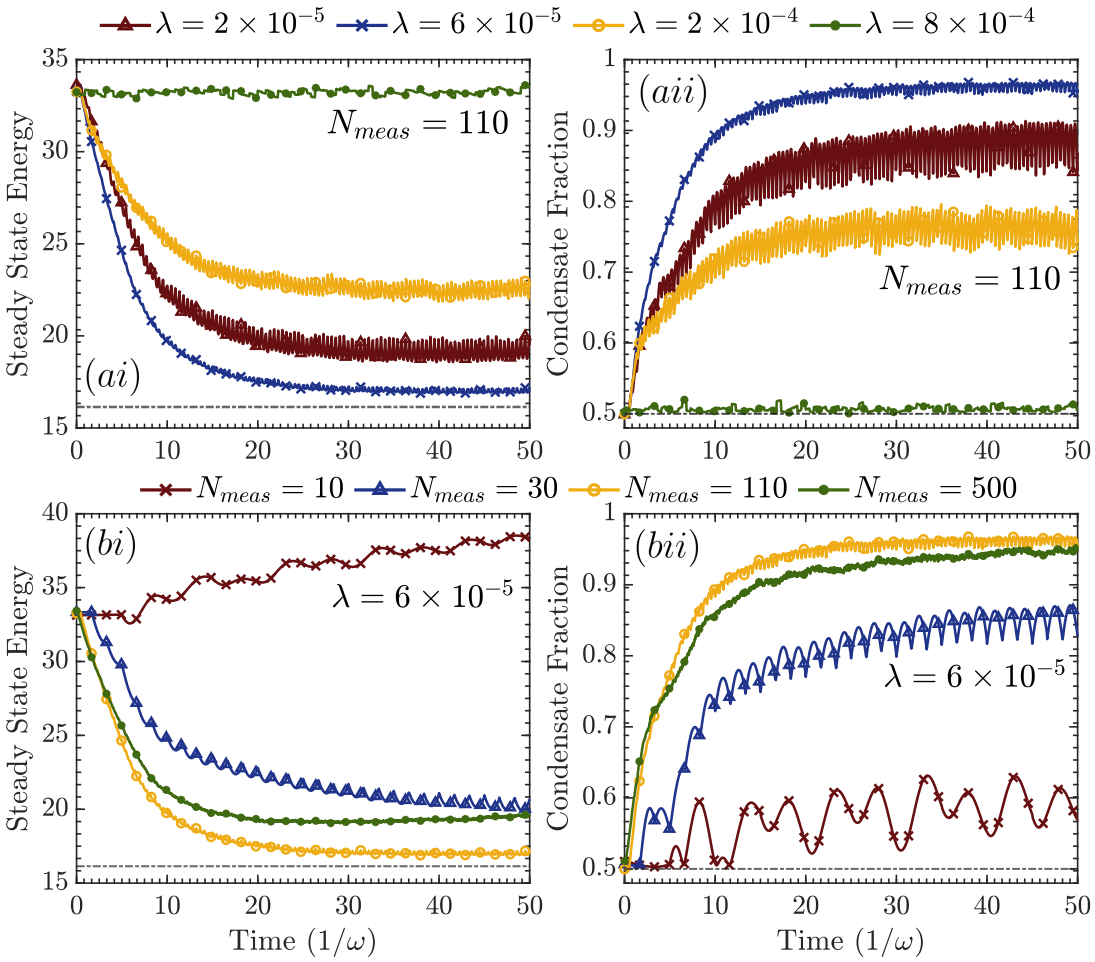

Figure 3.11: Time series of energy and two-mode condensate fraction for different measurement strengths and frequencies obtained using our TWA approach. All simulations were performed for an initially incoherent state. The same parameters as Fig. 3.6 and 3.7 are used, with the exception that feedback is turned on at $t_{on} = 0$. (ai), (aii) System energy and two-mode condensate fraction with the optimal measurement rate of $N_{meas} = 110$ for different measurement strengths. (bi), (bii) Energy and condensate fraction with the (fixed) optimal measurement strength of $\lambda = 6 \times 10^{-5}$ for different measurement rates. In (ai) and (bi), the ground state energy is plotted with a dashed line.

We see that the steady state energy generally increases with measurement strength. Physically, this trend reflects that the larger backaction (and hence heating) induced by stronger measurements quickly outweighs the increased energy extraction due to the improved feedback quality derived from a more accurate $\hat{J}_z$ estimate. On the contrary, too weak a measurement strength ($\lambda = 2 \times 10^{-5}$) and the measurement signal becomes increasingly noisy, leading to inaccurate estimates, ineffective feedback, and ultimately a higher steady state energy. There is therefore an optimal measurement rate that balances feedback efficiency and heating rate.

We arrive at similar conclusions for the dependence on measurement rate: Too low, and finite differences no longer produce accurate estimates for the derivative signal, drastically degrading the feedback quality. To some extent, one would sensibly expect

the optimal measurement rate to depend on the natural timescale of atomic dynamics. For higher measurement rates, we encounter the familiar SNR limitation described in Section 3.2. Naturally, there may exist many pairs (or in general, combinations) of viable parameters which lead to similar steady states. This is illustrated in Fig. 3.9 below, where the steady-state energy and condensate fraction are plotted across the entire parameter landscape. This is also how we previously identified the 'optimal' parameters.

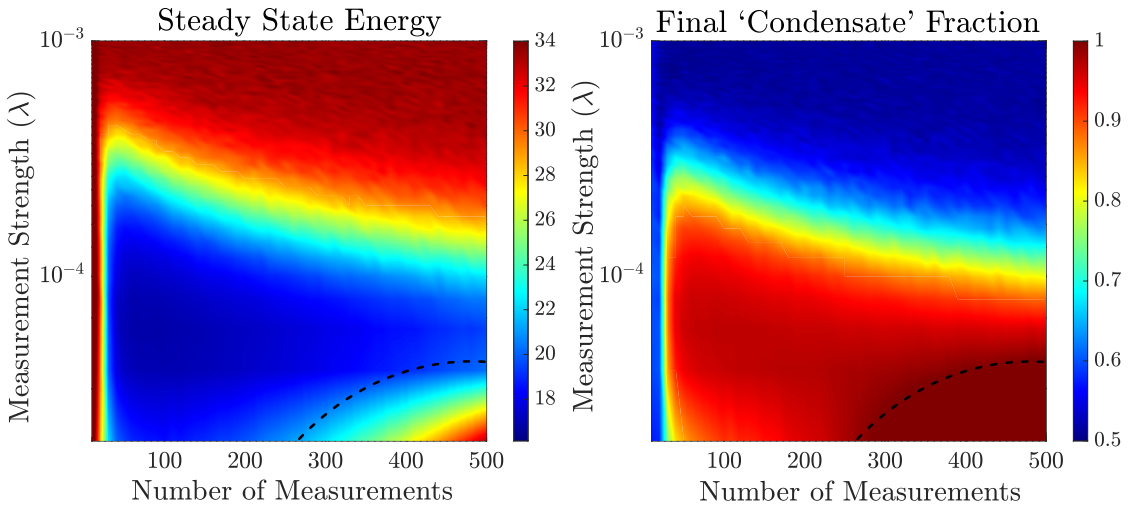

Figure 3.12: Steady state energy and final condensate fraction over a range of measurement strengths and rates. A small subset of the simulations (outlined with a black dashed line) did not converge as they required excessively many timesteps.

Indeed, there is clearly a wide range of parameter combinations which lead to similar steady states. We note three points of interest: Firstly, the steady-state energy and condensate fraction are inversely proportional, and essentially map injectively between each other. Hence, the steady-state is generally a good proxy for the condensate fraction. Secondly, we did not scan over the gain parameter (k_{fb}), though we expect it to affect the cooling efficiency. Finally, we note that for the most part, our conclusions should qualitatively generalise to the multi-mode case: The interplay between the SNR of the measurement signal, accuracy of the estimate and feedback quality, backaction heating, as well as their dependence on measurement parameters are intrinsic and independent of system choice and geometry.

3.8 Chapter Summary

We conclude by addressing the questions posed at the beginning of this chapter, before discussing the limitations of the two-mode system as well as avenues for further investigation.

3.8.1 Does our approach accurately represent the *unconditional* dynamics of a state subject to measurement and feedback?

Yes. The unconditional dynamics of various two-mode observables under periodic measurement and feedback predicted by our approach exhibits near-perfect agreement with the exact solution. This agreement is observed across both low and higher order moments, and all residuals were bounded by SU(2) and Wigner sampling error. Notably, we showed that the decoherence due to measurement backaction is correctly captured by modeling the quantum noise of the light.

The fundamental question to ask is whether our approach is scalable to multi-mode systems. As we saw in Section 3.6.2, there is little variety in the types of feedback accessible in two-modes. Naturally, the introduction of more modes leads to more vastly more freedom for choices of feedback, which may very well lead to complex dynamics. However, we are currently unable to see how an increase in the complexity of feedback dynamics could break our method, other than demanding that more Wigner trajectories are required to accurately represent the state.

3.8.2 Is our approach able to capture the transition from an incoherent mixture to high purity state? What are its regimes of validity?

Yes. We performed our simulations with both pure and incoherent initial states and computed the two-mode condensate fraction. For the maximally mixed initial state, we observed the two-mode condensate fraction grow from its minimal value of $f_{\text{cond}} = 0.5$ to $f_{\text{cond}} = 0.97$ under two-mode energy damping. Our method closely matched the exact solution at *all* times. However, as the minimal condensate fraction is bounded by $f_{\text{cond}} = 1/M$ where M is the number of modes in the system, one may instinctively ask whether this approach generalises to maximally mixed states of higher dimensions.

We are inclined to say **yes**. Though it is plausible that phase transitions in multi-mode systems appear more 'dramatic' than the one we observed in two-modes, there is nothing to suggest that the physical development of coherence behaves differently in systems of different dimension.

3.8.3 What is the correspondence between our approach and NPW?

Unsure, though we have ideas. As the primary difference between our approach and NPW is the neglect of the conditional state, a good starting point would be to simulate the same two-mode energy damping scheme with NPW and investigate how its predictions depend on the number of fictitious trajectories simulated. Though NPW models continuous weak measurements, this is no obstacle for our approach, as we may simply sample a new pulse of light on every timestep.

Chapter 4

QND Theory of Feedback Cooling

In Chapter 3, we benchmarked our new simulation technique against an exact solution for a two-mode system subject to periodic measurement and feedback, and found excellent agreement across all orders of moments. In this chapter, we generalise the QND-esque framework of measurement to describe an atomic ensemble undergoing phase-contrast imaging, which is currently the standard experimental procedure for non-destructive measurements [87]. A single-mode light field is used in the two-mode system. Here, the light requires a multi-mode description as the dispersive scattering of light during the measurement is spatially dependent. The scattering mixes the spatial modes of the light, and the resolution of the estimate is also limited by the diffraction limit of the propagating light. In addition, we also model the loss during each measurement pulse due to a finite fraction of the atoms being excited and subsequently spontaneously emitting into the vacuum.

In Section 4.1, we introduce the experimental apparatus and measurement procedure. In Section 4.2, we perform a microscopic derivation of the interaction Hamiltonian which describes phase-contrast imaging. In Section 4.3, we apply the instantaneous treatment of measurement as introduced in Chapter 3 to derive input-output equations for the atomic and light fields under measurement. The effects of spontaneous emission are incorporated through the 'beamsplitter' model introduced by Kristokakis [78] *et al.* . We make the transformation to Wigner phase-space variables and introduce a series of physically motivated approximations on the light. Finally, we conclude with a further dimensional reduction to 1D in order to obtain tractable equations for preliminary simulations, which are presented in Chapter 5.

This chapter primarily contains original work built upon Chapter 5 of [88]. Specifically, the QND treatment of phase-contrast imaging is new, as is our approach of keeping the light in.

4.1 Experimental Apparatus: Phase-Contrast Imaging

A schematic diagram of the experimental apparatus is provided in Fig. 4.1 below.

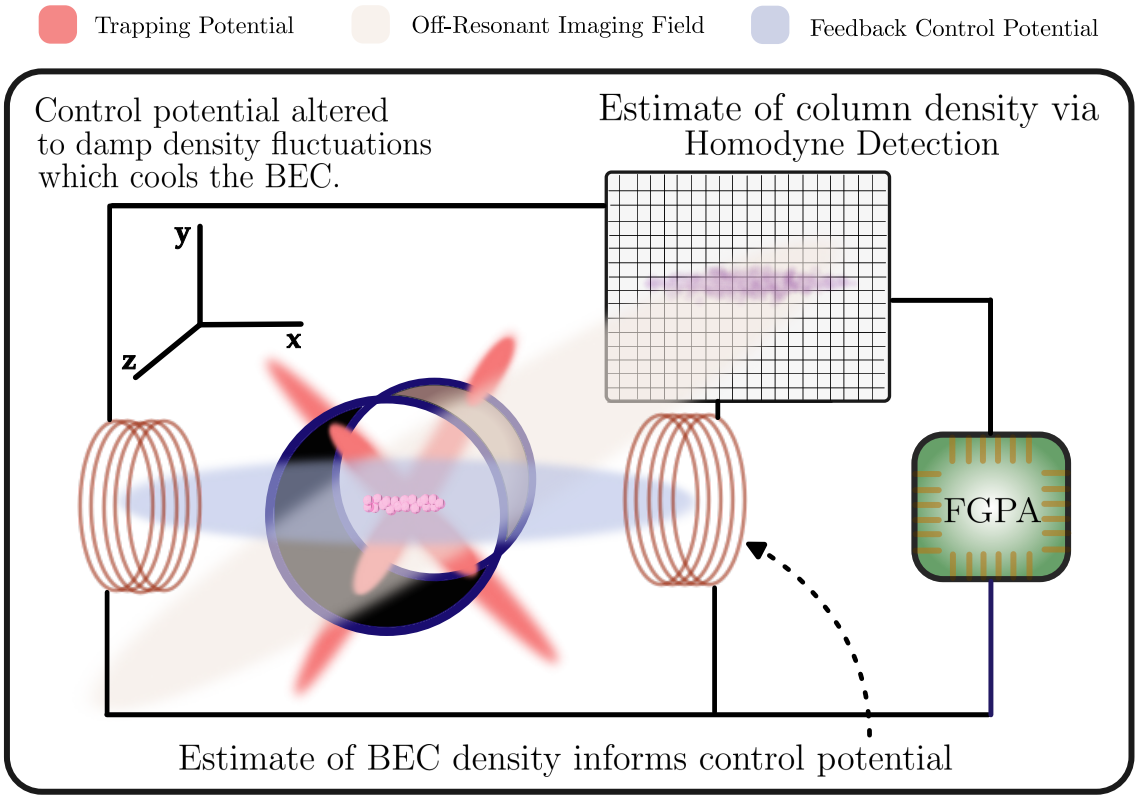

Figure 4.1: Schematic diagram of feedback cooling scheme. The atomic cloud is confined in trapping potential (red) and imaged through an off-resonant light field (beige) via phase-contrast imaging. The imaging axis is along z, while the imaged density lies in the $x-y$ (transverse) plane, which is derived from a measurement of the phase ($\hat{Y}(\boldsymbol{x})$) quadrature of the light via homodyne-detection. The detector array is two-dimensional. The density estimate is sent to a Field Programmable Gate Array (FPGA), where a time derivative for the atomic density is computed and used to update the feedback control potential (blue).

The atomic ensemble is magnetically confined in a trapping potential and imaged along the longitudinal (z) axis. An estimate of the transverse density profile $\boldsymbol{x} = (x, y)$ is derived from a measurement of the light's phase quadrature via Homodyne detection. Though the detector array is two-dimensional, one may integrate over the y-dimension to obtain the one-dimensional column density. In practice, the control potential could be engineered by patterning an optical trap with a Digital Micro-mirror Device (DMD), which was successfully demonstrated by Gauthier *et al.* in [89] to produce custom high-resolution (within 5% of the diffraction limit imposed by their optics and apparatus) optical potentials employed to trap BECs. In Fig. 4.1, we have crudely used a set of coils to represent generation of the control potential.

The consequences of experimental imperfections such as time-delay of the feedback loop are discussed in Chapter 6.

4.2 Deriving the Interaction Hamiltonian for Phase-Contrast Imaging

Our starting point will be the interaction Hamiltonian derived by Szigeti *et al.* in [43], and we will briefly outline the key steps within the derivation. Under the electric-dipole approximation, which is justified when the wavelength of the light is significantly greater than the Bohr radius of atom [12], the atom-light interaction Hamiltonian may be written as:

$$\hat{H}_I = -\int d^3\boldsymbol{x}\, \hat{\psi}_g^\dagger(\boldsymbol{x})\Big[\boldsymbol{d}_{eg}\cdot\hat{\boldsymbol{E}}(\boldsymbol{x},t)\Big]\hat{\psi}_e(\boldsymbol{x}) - \int d^3\boldsymbol{x}\, \hat{\psi}_g^\dagger(\boldsymbol{x})\Big[\boldsymbol{d}_{eg}\cdot\hat{\boldsymbol{E}}(\boldsymbol{x},t)\Big]\hat{\psi}_e(\boldsymbol{x}) \tag{4.1}$$

where $\boldsymbol{d}_{ij}$ is the transition electric dipole vector between the i'th and j'th levels of the atom, defined as:

$$\boldsymbol{d}_{ij} = \langle i|\hat{\boldsymbol{x}}|j\rangle \tag{4.2}$$

We assume that only the ground (g) and one excited (e) state are accessible to the atom (coupled via transition frequency ω_0)[1], corresponding to the field operators $\hat{\psi}_g(\boldsymbol{r})$ and $\hat{\psi}_e(\boldsymbol{r})$, respectively. The quantised electric field operator is as follows:

$$\hat{\boldsymbol{E}}(\boldsymbol{x}) = i\int d^3\boldsymbol{p}\sum_\lambda^2 \sqrt{\frac{\hbar\omega(\boldsymbol{p})}{2(2\pi)^3\varepsilon_0}}\Big\{\hat{a}_\lambda(\boldsymbol{p})e^{i\boldsymbol{p}\cdot\boldsymbol{x}/\hbar} - \hat{a}_\lambda^\dagger(\boldsymbol{p})e^{-i\boldsymbol{p}\cdot\boldsymbol{x}/\hbar}\Big\}\boldsymbol{\epsilon}_\lambda(\boldsymbol{p}) \tag{4.3}$$

where $\boldsymbol{\epsilon}_\lambda(\boldsymbol{p})$ is a polarisation unit vector, and $\hat{a}_\lambda(\boldsymbol{p})$ is the annihilation operator for a photon with momentum $\boldsymbol{p}$ and polarisation λ [43].

4.2.1 Dimensional Reduction to 2D

We would like apply the Markovian approximation to the electromagnetic field in order to treat it using reservoir approximations [44]. However, this requires there to be many more modes of the electromagnetic field (reservoir) when compared to the atomic field (system). This criterion may be satisfied by assuming the atomic cloud is tightly trapped along the imaging axis, and hence only occupies a single spatial mode, permitting a dimensional reduction of our field operators:

$$\hat{\psi}_g(\boldsymbol{x}) \approx g(z)\hat{\psi}_g(\boldsymbol{x}), \qquad \hat{\psi}_e(\boldsymbol{x}) \approx g(z)e^{ik_0 z}\hat{\psi}_e(\boldsymbol{x}) \tag{4.4}$$

where $\boldsymbol{x} = (x, y)$. The factor $\exp(ik_0 z)$ arises from the momentum kick imparted by the exciting photon ($k_0 = \omega_0/c$), and we have chosen a Gaussian ansatz[2] for the spatial mode along the reduced dimension:

$$|g(z)|^2 = \frac{1}{R_z\sqrt{\pi}}\exp\left(-\frac{z^2}{R_z^2}\right) \tag{4.5}$$

[1] For ^{87}Rb, these are the $3S_{1/2}$ and $3P_{3/2}$ hyperfine levels.

[2] The non-interacting ground state of the harmonic trapping potential is a Gaussian. In the strongly interacting regime, a Thomas-Fermi profile may be more appropriate. However, a Gaussian is easier to work with, and won't lead to qualitatively different results.

where R_z is the characteristic width of the Gaussian mode[3]. Importantly, note that after the dimensional reduction, there are now an infinite number of electromagnetic modes along z for a single atomic mode, so we may treat the z component of the electromagnetic field as a reservoir. Next, we recast Eq. 4.3 into $\boldsymbol{k}$-space and separate out the transverse and longitudinal components of the field using the dispersion relation $\omega = c|\boldsymbol{k}|$. Taking the forward scattering limit[4], the field may be expressed as:

$$\hat{\boldsymbol{E}}(\boldsymbol{x}) = i \int d^2\boldsymbol{k}_\perp \int d\omega \sum_\lambda^2 \sqrt{\frac{\omega^2}{2(2\pi)^3 \epsilon_0 c^2 k_z}} \Big[\hat{a}(\boldsymbol{k}_\perp, \omega) e^{i\boldsymbol{k}_\perp \cdot \boldsymbol{x}} e^{ik_z z} + \text{h.c}\Big] \boldsymbol{\epsilon}_\lambda(\boldsymbol{k}_\perp, \omega) \tag{4.6}$$

where $\boldsymbol{k}_\perp = (k_x, k_y)$, and $\hat{a}(\boldsymbol{k}_\perp, \omega)$ annihilates a forward traveling photon with transverse momentum $\boldsymbol{k}_\perp$ and frequency ω. At this point, we may substitute the above into Eq. 4.1, and after transforming into the interaction picture and making a series of approximations, Szigeti *et al.* arrive at the final interaction Hamiltonian:

$$\hat{H}_I = -i\frac{\hbar}{\sqrt{t_p}} \int d^2\boldsymbol{k}_\perp \sqrt{\gamma(\boldsymbol{k}_\perp)} \Big(\hat{b}^\dagger(\boldsymbol{k}_\perp) \int d^2\boldsymbol{x}\, \hat{\psi}_g^\dagger(\boldsymbol{x}) \hat{\psi}_e(\boldsymbol{x}) e^{-i\boldsymbol{k}_\perp \cdot \boldsymbol{x}} + \text{h.c} \Big) \tag{4.7}$$

where $\gamma(\boldsymbol{k}_\perp)$ is the coupling strength (function) defined by:

$$\gamma(\boldsymbol{k}_\perp) \approx \frac{d_{eg}^2 k_0}{2(2\pi)^2 \epsilon_0 \hbar} \frac{1}{2\pi} \exp\left(-\frac{R_z^2}{8} \frac{|\boldsymbol{k}_\perp|^4}{k_0^2} \right) \tag{4.8}$$

Note that the optical operators ($\hat{b}(\boldsymbol{k}_\perp)$) in Eq. 4.7 have been transformed back into the temporal domain, where the following flux (continuous) and particle-like (discrete) optical operators have been defined:

$$\hat{b}(\boldsymbol{k}_\perp, t) = \frac{1}{\sqrt{2\pi}} \int_{\omega_0 - \vartheta}^{\omega_0 + \vartheta} d\omega\, \hat{a}(\boldsymbol{k}_\perp, \omega) e^{-i(\omega - \omega_L)}, \qquad \hat{b}(\boldsymbol{k}_\perp, t) = \frac{\Pi(t/t_p)}{\sqrt{t_p}} \hat{b}(\boldsymbol{k}_\perp) \tag{4.9}$$

where $\hat{b}(\boldsymbol{k}_\perp, t)$ is a flux-like operator, in the sense that one would have to integrate over the finite pulse duration t_p to obtain the particle-like annihilation operator $\hat{b}(\boldsymbol{k}_\perp)$. This is encoded in $\Pi(t/t_p)$, which is a top-hat function that is only non-zero during the pulse duration.

4.2.2 Adiabatic Elimination of the Excited State

On the timescale of the measurement process (t_p), very few atoms will populate the excited state, and it may be adiabatically eliminated. Again, we briefly outline the procedure here and refer to [43] for a detailed derivation. Starting with Heisenberg's equations of motion for $\hat{\psi}_e(\boldsymbol{x})$, one obtains:

$$\begin{aligned} \partial_t \hat{\psi}_e(\boldsymbol{x}) &= \frac{i}{\hbar}\Big[\hat{H}_A + \hat{H}_I, \hat{\psi}_e(\boldsymbol{x})\Big] \\ &= -(H_A(\boldsymbol{x}) + \hbar\omega_0)\hat{\psi}_e(\boldsymbol{x}) - \frac{i\hbar}{\sqrt{t_p}} \hat{\psi}_g(\boldsymbol{x}) \int d^2\boldsymbol{k}_\perp \sqrt{\gamma(\boldsymbol{k}_\perp)} \hat{b}(\boldsymbol{k}_\perp) e^{i\boldsymbol{k}_\perp \cdot \boldsymbol{x}} \end{aligned} \tag{4.10}$$

[3]The width is generally wider than the width of the non-interacting Gaussian ground state due to repulsive interactions. In practice, we may use variational methods to obtain a more accurate estimate for R_z.

[4]This assumes that most of the light scattering off the atoms propagates forwards such that the backwards scattering is negligible, which is true for our experimental geometry.

where $\hat{H}_A(\boldsymbol{x})$ is the self-Hamiltonian of the atomic field. Transforming into the rotating frame of the laser, taking the large detuning limit (which is the operating regime for dispersive imaging), and finally assuming the excited state population is roughly static on the measurement timescale (i.e $\partial_t \hat{\psi}(\boldsymbol{x}) \approx 0$), we may approximately solve for $\hat{\psi}(\boldsymbol{x})$:

$$\hat{\psi}_e(\boldsymbol{x}) \approx -\frac{i}{\Delta\sqrt{t_p}}\hat{\psi}_g(\boldsymbol{x}) \int d^2\boldsymbol{k}_\perp \sqrt{\gamma(\boldsymbol{k}_\perp)}\hat{b}(\boldsymbol{k}_\perp)e^{i\boldsymbol{k}_\perp\cdot\boldsymbol{x}} \tag{4.11}$$

where Δ is the laser detuning. **From here, we are no longer following Szigeti *et al.* .** Substituting the above into Eq. 4.7, we arrive at the following interaction Hamiltonian:

$$\hat{H}_I = -\frac{2\hbar}{\Delta t_p}\int d^2\boldsymbol{x}\, \hat{n}(\boldsymbol{x}) \int d^2\boldsymbol{x}' \hat{b}(\boldsymbol{x}')\Gamma^*(\boldsymbol{x}-\boldsymbol{x}') \int d^2\boldsymbol{x}''\, \hat{b}(\boldsymbol{x}'')\Gamma(\boldsymbol{x}-\boldsymbol{x}'') \tag{4.12}$$

where we have defined the atomic density operator as $\hat{n}(\boldsymbol{x}) = \hat{\psi}_g^\dagger(\boldsymbol{x})\hat{\psi}_g(\boldsymbol{x})$ as well as the function:

$$\Gamma(\boldsymbol{x}-\boldsymbol{x}') = \frac{1}{2\pi}\int d^2\boldsymbol{k}_\perp \sqrt{\gamma(\boldsymbol{k}_\perp)}e^{i\boldsymbol{k}_\perp\cdot(\boldsymbol{x}-\boldsymbol{x}')} \tag{4.13}$$

The form of Eq. 4.12 lends itself to physical interpretation. We see that the atomic density, $(\hat{n}(\boldsymbol{x}))$ is convolved with the function $\Gamma(\boldsymbol{x})$ during its interaction with the optical field. As $\gamma(\boldsymbol{k}_\perp)$ takes the form of a sharply peaked Gaussian in $\boldsymbol{k}_\perp$-space, convolution with its real space counterpart is analogous to a 'blurring' of the input density. This blurring arises from the diffraction of light during its propagation: Light rays do not remain perfectly parallel during propagation[5] and diffract by an amount proportional to the distance propagated. In our case, this is the width (R_z) of the atomic ensemble along the imaging axis.)

4.2.3 Incorporating Spontaneous Emission

A finite fraction of atoms will be lost during every measurement pulse due to spontaneous emission. For a continuous measurement, the fractional loss increases as an exponential function of pulse duration, and is dependent on the spontaneous emission rate of the excited state [90]. As we are modeling instantaneous measurement, the fractional loss may be equivalently recast in terms of the average photon number in each pulse [77]:

$$f = 1 - \exp(-\eta), \quad \eta \approx \frac{\sigma_0\Gamma^2}{4\Delta^2}\beta_0^2 \tag{4.14}$$

where σ_0 is the resonant absorption cross-section for the atom, Γ is the linewidth of the excited state, Δ is the the detuning of the optical field from the resonant transition frequency, and β_0^2 is the photon number density across the cross-sectional area of the atomic field. If the light is treated as a coherent state, β_0 is simply the coherent state amplitude.

For a single measurement pulse, we replace a fraction of the atomic field with coupling to vacuum noise. This treatment follows the 'beamsplitter model' as introduced by Furderer *et al.* [77], and is thoroughly discussed by Kritsotakis *et al.* in [78]. Intuitively, stronger measurement leads to greater loss, so it is instructive to recast the measurement strength in terms of η. Re-expressing the coupling function in terms of the excited state linewidth

[5] As this would violate the uncertainty relation for $\Delta k \Delta x$, where k is the wavevector of the light.

(Γ) as well as the diffraction limit (r_d):

$$\Gamma = \frac{1}{4\pi\epsilon_0}\frac{4d_{ge}^2 k_0^3}{3\hbar}, \qquad r_d = \sqrt{\frac{R_z\lambda}{2\pi}} \tag{4.15}$$

substituting into interaction Hamiltonian in Eq. 4.7 produces:

$$\hat{H}_I = -\frac{\hbar\lambda_{2D}}{t_p\beta_0}\int d^2\boldsymbol{x}\,\hat{n}(\boldsymbol{x})\int d^2\boldsymbol{x}'\hat{b}(\boldsymbol{x}')f^*(\boldsymbol{x}-\boldsymbol{x}')\int d^2\boldsymbol{x}''\,\hat{b}(\boldsymbol{x}'')f(\boldsymbol{x}-\boldsymbol{x}'') \tag{4.16}$$

where we have defined the dimensionless measurement strength:

$$\lambda_{2D} = \frac{3}{2\sqrt{2\pi}}\frac{r_d^3}{R_z^2}\sqrt{\frac{\eta}{\sigma_0}} \tag{4.17}$$

and the 'blurring' kernels:

$$f(\boldsymbol{x}) = \mathcal{F}^{-1}\{f(\boldsymbol{k}_\perp)\}, \qquad f(\boldsymbol{k}_\perp) = \frac{\sqrt{r_d}}{(2\pi^3)^{1/4}}\exp\left(-\frac{r_d^4}{16}|\boldsymbol{k}_\perp|^4\right) \tag{4.18}$$

We have chosen scaling such that $f(\boldsymbol{k}_\perp)$ obeys the normalisation $\int d\boldsymbol{k}_\perp\,|f(\boldsymbol{k}_\perp)|^2 = 1/r_d{}^6$.

4.3 Implementing Measurement

We are now fully equipped to derive the equations describing the measurement. Following the procedure of Section 3.5, we write Heisenberg's equations of motion for the atomic and field operator under the interaction Hamiltonian[7]:

$$\begin{aligned}
\partial_t\hat{\psi}(\boldsymbol{x}) &= -\frac{i}{\hbar}\left[\hat{H}_I,\hat{\psi}(\boldsymbol{x})\right] & \partial_t\hat{b}(\boldsymbol{x}) &= \frac{i}{\hbar}\left[\hat{H}_I,\hat{b}(\boldsymbol{x})\right]\\
&= -\frac{i\lambda_{2D}}{t_p\beta_0}\hat{\psi}(\boldsymbol{x})\hat{\mathcal{B}}(\boldsymbol{x}) & &= -\frac{i\lambda_{2D}}{t_p\beta_0}\hat{\mathcal{A}}(\boldsymbol{x})\\
\implies \hat{\psi}_{\text{out}}(\boldsymbol{x}) &= \hat{\psi}_{\text{in}}(\boldsymbol{x})\exp\left(-\frac{i}{\beta_0}\hat{\mathcal{B}}(\boldsymbol{x})\right) & \hat{b}_{\text{out}}(\boldsymbol{x}) &= \hat{b}_{\text{in}}(\boldsymbol{x}) - i\frac{\lambda_{2D}}{\beta_0}\hat{\mathcal{A}}(\boldsymbol{x})
\end{aligned} \tag{4.19}$$

where we have defined:

$$\begin{aligned}
\hat{\mathcal{B}}(\boldsymbol{x}) &= \int d^2\boldsymbol{x}'\hat{b}_{\text{in}}^\dagger(\boldsymbol{x}')f^*(\boldsymbol{x}-\boldsymbol{x}')\int d^2\boldsymbol{x}''\,\hat{b}_{\text{in}}(\boldsymbol{x}'')f(\boldsymbol{x}-\boldsymbol{x}'')\\
\hat{\mathcal{A}}(\boldsymbol{x}) &= \int d^2\boldsymbol{x}'\int d^2\boldsymbol{x}''\,f^*(\boldsymbol{x}'-\boldsymbol{x})f(\boldsymbol{x}'-\boldsymbol{x}'')\hat{n}_{\text{in}}(\boldsymbol{x}')\hat{b}_{\text{in}}(\boldsymbol{x}'')
\end{aligned} \tag{4.20}$$

We see from Eq. 4.19 that $\hat{\mathcal{B}}(\boldsymbol{x})$ plays the role of measurement backaction and imparts a spatially dependent phase shift to the atomic field. We will refer to this term as the backaction phase.

Once again applying the same logic of Section 3.5, we may integrate Eqs. 4.19 directly and replace the operators with Wigner variables $\psi(\boldsymbol{x})$ and $\beta(\boldsymbol{x})$. These are now multi-mode phase-space variables for the atomic and light fields defined on a continuous spatial basis.

[6] By Parseval's theorem, $f(x)$ obeys the same normalisation.

[7] Note that we have dropped the subscript g in the field operator.

The operator valued quantities in Eq. 4.20 are analogously mapped to functions of the phase-space variables, may be further simplified. Firstly, if the light is described by a coherent state, we may write:

$$\hat{b}(\hat{\boldsymbol{x}}) = \beta_0\delta^2(\boldsymbol{x}) + \hat{v}(\boldsymbol{x}) \to \beta(\boldsymbol{x}) = \beta_0 + \epsilon(\boldsymbol{x}) \tag{4.21}$$

That is, the light is well modeled as complex quantum vacuum noise $\epsilon(\boldsymbol{x})$ with mean correlations $\overline{\epsilon(\boldsymbol{x})\epsilon^*(\boldsymbol{x}')} = \delta(\boldsymbol{x}-\boldsymbol{x}')/2$ on top of a spatially constant background field with amplitude β_0, where $|\epsilon(\boldsymbol{x})| \ll |\beta_0|$. On inspection, substitution of Eq. 4.21 into Eq. 4.20 leads to the term:

$$\beta^*_{\text{in}}(\boldsymbol{x}')\beta_{\text{in}}(\boldsymbol{x}'') = \beta_0^2 + \beta_0(\epsilon^*(\boldsymbol{x}') + \epsilon(\boldsymbol{x}'')) + \epsilon^*(\boldsymbol{x}')\epsilon(\boldsymbol{x}'') \tag{4.22}$$

Recalling that $\mathcal{B}(x)$ is the backaction phase, see that the first term on the RHS of Eq. 4.22 leads to a constant phase-shift that is independent of the measurement process, so we will discard it as we did for the two-mode case in Section 3.5. The final term, $\epsilon^*(\boldsymbol{x}')\epsilon(\boldsymbol{x}'')$, is infinitesimally small and may also be discarded. Secondly, we note that $\mathcal{A}(\boldsymbol{x})$ comprises our measurement signal and forms our estimate of the atomic spatial density. As $|\beta_0| \gg |\epsilon(\boldsymbol{x})|$, it is reasonable to neglect the noise term in $\mathcal{A}(\boldsymbol{x})$. Physically, we are simply saying that the dominant contribution to our measurement signal arises from the large coherent amplitude of the light, rather than the vacuum noise.

Under these simplifications as well as repeated application of the convolution theorem, we arrive at the following expressions for the backaction phase:

$$\mathcal{B}(\boldsymbol{x}) = \beta_0\mathcal{G}(\boldsymbol{x}), \quad \mathcal{G}(\boldsymbol{x}) = \frac{\sqrt{r_d}}{(2\pi^3)^{1/4}}\int d^2\boldsymbol{x}'\ (\epsilon^*(\boldsymbol{x}') + \epsilon(\boldsymbol{x}'))f(\boldsymbol{x}-\boldsymbol{x}') \tag{4.23}$$

For the quadrature measurement, we have:

$$\begin{aligned}\mathcal{Y}_{\text{out}}(\boldsymbol{x}) &= i(\beta_{\text{out}}(\boldsymbol{x}) - \beta^*_{\text{out}}(\boldsymbol{x})) \\ &= i(\epsilon(\boldsymbol{x}) - \epsilon^*(\boldsymbol{x})) + 2\lambda_{\text{2D}}n_{\text{inf}}(\boldsymbol{x})\end{aligned} \tag{4.24}$$

where we have constructed the 'inferred' density, $n_{\text{inf}}(\boldsymbol{x})$ out of $\mathcal{A}(\boldsymbol{x})$:

$$n_{\text{inf}}(\boldsymbol{x}) = \frac{\mathcal{A}(\boldsymbol{x})}{\beta_0} = \frac{\sqrt{r_d}}{(2\pi^3)^{1/4}}\int d^2\boldsymbol{x}'\ f^*(\boldsymbol{x}'-\boldsymbol{x})n_{\text{in}}(\boldsymbol{x}') \tag{4.25}$$

The 'inferred' density refers to the best possible estimate of the atomic density, limited only by the diffraction induced blurring of the light. Realistically, the measurement signal is also corrupted by the quantum noise of the light (which manifests as the real noise $i(\epsilon(\boldsymbol{x}) - \epsilon^*(\boldsymbol{x}))$ in Eq. 4.24) and so our actual estimate is given by:

$$n_{\text{est}}(\boldsymbol{x}) = \frac{\mathcal{Y}_{\text{out}}(\boldsymbol{x})}{2\lambda_{\text{2D}}} \tag{4.26}$$

Finally, the resolution of our estimate is also constrained by the resolution of the PCI apparatus. We model this by further convolving n_{est} with a a Gaussian point-spread kernel with width set by the PCI resolution. Finally, we conclude with how the atomic

fields are transformed by the measurement:

$$\psi_{\text{out}}(\boldsymbol{x}) = \sqrt{e^{-\eta}}\psi_{\text{in}}(\boldsymbol{x})e^{-i\lambda_{2\text{D}}\mathcal{G}(\boldsymbol{x})} + \sqrt{1-e^{-\eta}}v(\boldsymbol{x}) \tag{4.27}$$

where $v(\boldsymbol{x})$ is a complex vacuum noise obeying the same correlations as $\epsilon(\boldsymbol{x})$. In other words, spontaneous emission is incorporated by replacing the fraction of the atomic field lost due to spontaneous emission during each measurement with vacuum noise.

4.4 Dimensional Reduction to 1D

For preliminary investigations of feedback cooling, it is beneficial to further reduce the dimensionality of the system. Physically, this corresponds to tight trapping along another dimension (y). The process is largely analogous to that of Section 4.2.1, with the addition that we make a flat, top-hat ansatz with length l_y for the optical intensity along the reduced dimension:

$$\hat{\psi}(\boldsymbol{x}) \approx h(y)\hat{\psi}(x), \qquad \hat{b}(\boldsymbol{x}) \approx u(y)\hat{b}(x) \tag{4.28}$$

where:

$$|h(y)|^2 = \frac{1}{R_y\sqrt{\pi}}\exp\left(-\frac{y^2}{R_y^2}\right), \qquad u(y) = \frac{1}{\sqrt{l_y}}\Pi\left(\frac{y}{l_y}\right) \tag{4.29}$$

We will simply provide the final reduced equations and the 1D parameters. Notably, the blurring kernel ($g_{1\text{D}}(x)$) is rescaled in order to preserve the previous normalisation:

$$g_{1\text{D}}(x) = \mathcal{F}^{-1}\{g_{1\text{D}}(k_x)\}, \quad g_{1\text{D}}(k_x) = G_0\exp\left(-\frac{r_d^4}{16}k_x^4\right), \quad G_0 = \sqrt{\frac{2^{1/4}}{\Gamma[1/4]}} \tag{4.30}$$

The prefactors have been chosen such that $g_{1\text{D}}(x)$ retains the normalisation to $1/r_d$. The inferred and actual estimate of the density become:

$$\begin{aligned} n_{\text{inf}}^{1\text{D}}(x) &= G_0\int dx'\, g_{1\text{D}}^*(x-x')n_{\text{in}}^{1\text{D}}(x') \\ n_{\text{est}}^{1\text{D}}(x) &= \frac{\mathcal{Y}_{\text{out}}^{1\text{D}}(x)}{2\sqrt{l_y}\lambda_{1\text{D}}} \end{aligned} \tag{4.31}$$

The backaction and output atomic field:

$$\begin{aligned} \mathcal{G}_{1\text{D}}(x) &= G_0\sqrt{l_y}\int dx'\,(\epsilon_{1\text{D}}^*(x') + \epsilon_{1\text{D}}(x'))g_{1\text{D}}(x-x') \\ \psi_{\text{out}}^{1\text{D}}(x) &= \sqrt{e^{-\eta}}\psi_{\text{in}}^{1\text{D}}(x)e^{-i\lambda_{1\text{D}}\mathcal{G}_{1\text{D}}(x)} + \sqrt{1-e^{-\eta}}v_{1\text{D}}(x) \end{aligned} \tag{4.32}$$

Finally, the one-dimensional interaction strength has been rescaled to to:

$$\lambda_{1\text{D}} = \frac{\Gamma(1/4)}{(\sqrt{2}\pi)^{3/2}}\frac{r_d}{l_y}\lambda_{2\text{D}}. \tag{4.33}$$

Physically, one may interpret the 1D density estimate as the integrated column density of the original two-dimensional estimate, which generally leads to an increased signal-to-noise ratio for the measurement signal.

Chapter 5

Multi-Mode Feedback Cooling in 1D

In Chapter 4, we derived the interaction Hamiltonian which describes phase-contrast imaging and applied it to model feedback cooling. In this chapter, we conduct preliminary investigations into feedback cooling using the one-dimensional equations derived in Section 4.4. Crucially, we simulate cooling for a finite-temperature atomic gas at thermal equilibrium, which we sample via the Stochastic Projected Gross-Pitaevskii Equation (SPGPE) [91]. We demonstrate successful cooling of an incoherent thermal state with low initial condensate fraction to condensed mode. Importantly, our simulations did *not* incorporate the losses due to spontaneous emission. This is a crucial omission from any experimentally realistic model. However, as spontaneous emission primarily constrains the final size of the BEC and not the underlying physics of the measurement and feedback procedure, its omission should not drastically alter our conclusions on regarding the feasibility of feedback cooling itself. We revisit the idea of spontaneous emission in Chapter 6, where we discuss avenues for further investigation.

This chapter contains both background theory and original work. We introduce the numerical methods needed to implement our simulations in Section 5.1. In Section 5.2, we review the Stochastic Projected Gross-Pitaevskii Equation (SPGPE), which is a formalism capable of describing atomic ensembles at finite temperature. Our results are contained in Section 5.3, and Section 5.4 is a chapter summary. All simulations were implemented with MATLAB and XMDS2 [92] on the GADI supercomputer at the NCI facility.

5.1 Feedback Cooling in 1D: Numerical Techniques

5.1.1 Optimal Basis Choice

Let us look at our equation of motion for the phase-space variable $\psi(\boldsymbol{x})$:

$$\partial_t \psi(\boldsymbol{x}) = i\Bigg\{\overbrace{\left(-\frac{1}{2}\nabla^2 + \frac{1}{2}\boldsymbol{x}^2\right)\psi(\boldsymbol{x})}^{\text{Diagonal in H.G basis}} + \underbrace{g|\psi(\boldsymbol{x})|^2\psi(\boldsymbol{x}) + k_{\text{fb}} f(\boldsymbol{x},t)\psi(\boldsymbol{x})}_{\text{Diagonal in } \boldsymbol{x} \text{ basis}}\Bigg\} \tag{5.1}$$

where we have used $f(\boldsymbol{x},t)$ to denote an arbitrary feedback potential. There are two sensible basis choices:

- The discrete position basis (sometimes referred to as the plane wave basis), where the wavefunction is defined at every point on an evenly spaced spatial lattice. In this case, the modes of the system are the discrete lattice points. Using a Fast Fourier Transform, the kinetic energy term may be computed in $\boldsymbol{k}$-space where it is diagonal.
- The Hermite-Gauss (HG) basis, which are the eigenstates of the harmonic trapping potential. The wavefunction is projected onto a finite set of M HG basis functions and stored as a vector of expansion coefficients, i.e: $\Psi(\boldsymbol{x}) = \sum_n^M c_n \phi_n(\boldsymbol{x})$ where $\phi_n(\boldsymbol{x})$ is the n'th HG mode, and the vector of c_n coefficients represents the wavefunction. In this cases, the modes of the system refer to the HG basis modes.

The position basis is arguably the most natural choice, as both the measurement and feedback terms are defined in the same basis. However, in the presence of noise or strongly interacting regimes where it plausible that the state undergoes violent dynamics over short timescales, the number of timesteps required for numerical convergence rapidly increases. In the latter case, the wavefunction may also contain high frequency components arising from rapidly changing dynamics, and so a larger number of grid points are required to accurately represent the state. This is less of a problem in the spectral basis as higher order HG modes are naturally oscillatory, so fewer modes required to represent high-frequency components. The interaction and feedback terms may be computed exactly using the method of Gaussian quadrature, which we explain in Section 4.5.4.

5.1.2 Spectral Basis: Mode Projection

A key component of our simulations is *projection*. Specifically, assume that the field is represented by a finite number of modes (M), i.e $\Psi(\boldsymbol{x}) = \sum_n^M c_n \phi_n(\boldsymbol{x})$. At all times, we impose an energy cutoff (ϵ_{cut}) such that the occupation of modes with energy greater than the cutoff is zero:

$$n_i = \begin{cases} n_i, & \text{if } \epsilon_i \leq \epsilon_{\text{cut}}. \\ 0, & \text{if } \epsilon_i > \epsilon_{\text{cut}}.. \end{cases} \tag{5.2}$$

Here, n_i and ϵ_i are the occupation and energies of the i'th mode, respectively. Formally, we implement this procedure via a projection operator defined in the following way:

$$\mathcal{P}\{f(\boldsymbol{x})\} = \sum_{n\in\mathbf{C}}^{n_{\text{cut}}} \phi_n(\boldsymbol{x}) \int d^3\boldsymbol{x}'\, \phi_n^*(\boldsymbol{x}') f(\boldsymbol{x}') \tag{5.3}$$

We will explain the purpose of the projection in Section 5.2. The projection is natural in the HG basis as each mode possess a well defined energy (in the harmonic potential). In the position basis, the projection may be implemented in $\boldsymbol{k}$-space by setting all momentum modes with $|\boldsymbol{k}| > |\boldsymbol{k}_{\text{cut}}|$. However, the appropriate choice for $\boldsymbol{k}_{\text{cut}}$ is not clear: One could plausibly determine $\boldsymbol{k}_{\text{cut}}$ by computing the kinetic energy associated with a certain wavevector. However, this approach neglects the contribution due to the potential energy.

5.1.3 Spectral Basis: Hermite-Gauss Quadratures

In terms of the spectral HG coefficients (c_n), the time evolution of Eq. 5.1 is given by:

$$\partial_t c_n(t) = -i\mathcal{P}\Big\{\epsilon_n c_n(t) + g\int d^2\boldsymbol{x}\,|\psi(\boldsymbol{x})|^2\psi(\boldsymbol{x})\phi_n^*(\boldsymbol{x})\Big\} \tag{5.4}$$

Here, ϵ_n is the energy of the n'th HG mode. Though the nonlinear interaction term may look discouraging at first, it may be exactly computed using Gaussian quadrature rules. A quadrature rule is a method to approximate an integral as a weighted sum of the integrand evaluated at specific quadrature points. The choice of quadrature rule is generally determined by the form of the integral, and a comprehensive review may be found in Chapter 8 of [93]. Specifically, we are interested in *Gaussian* quadrature, which approximates integrals of the form $\int_{-\infty}^{\infty} d\boldsymbol{x}\, e^{-\boldsymbol{x}^2} f(\boldsymbol{x})$. Applying directly to the nonlinear term, we have the following:

$$\mathcal{F}_n = \int d\boldsymbol{x}\,|\psi(\boldsymbol{x})|^2\psi(\boldsymbol{x})\phi_n^*(\boldsymbol{x}) \approx \sum_{k=1}^{M} w_k^{4f}\left|\psi\left(\frac{\boldsymbol{x}_k}{\sqrt{2}}\right)\right|^2\psi\left(\frac{\boldsymbol{x}_k}{\sqrt{2}}\right)\phi_n^*\left(\frac{\boldsymbol{x}_k}{\sqrt{2}}\right) \tag{5.5}$$

where $\boldsymbol{x}_k$ are the zeros of the M'th physicists[1] Hermite function ($H_M(\boldsymbol{x})$), and w_k^{4f} are (four-field) Hermite-Gauss quadrature weights evaluated at the zeros:

$$w_k^{4f} = \frac{\pi}{2}\frac{2^{M+1}M!}{H_{M+1}(\boldsymbol{x}_k)^2}e^{\boldsymbol{x}_k^2} \tag{5.6}$$

We have explicitly denoted the weights with the superscript $(4f)$ as we have used a *four-field* quadrature rule, in the sense that the integrand in Eq. 5.4 may be written as a sum of products of four HG basis functions[2]. In general, the pre-factor and exponential term in the weights vary for different n-field quadratures, as will the points at which the integrand is evaluated[3]. Finally, if the number of Hermite-Gauss quadrature points (M) is chosen such that $M \geq 2N - 3/2$, where N is the number of modes used to represent the field, the error in the quadrature rule vanishes such that the sum in Eq. 5.5 becomes exact. Again, refer to Chapter 8 of [93] for a proof of this property.

[1] Note: Hermite functions are commonly expressed in two different ways: The *Physicist's* and *Probabilist's* Hermite functions. As we are more a physicist than a probabilist, we use the former convention.

[2] See this by expanding out the field $\psi(\boldsymbol{x})$ in the spectral basis.

[3] For example, say we use the same number of quadrature points for a two, three, and four field quadrature rule. The integrand for each rule is evaluated at $\boldsymbol{x}_k$, $\sqrt{2/3}\boldsymbol{x}_k$, and $\boldsymbol{x}_k/\sqrt{2}$, respectively.

5.1.4 Ground State Finder: Imaginary Time Propagation

We will often want to find the ground state of the system in order to characterise the steady-state of our simulations. In general, this is analytically impossible in the presence of interactions[4]. For strongly interacting regimes where the kinetic energy is negligible in comparison to the interaction energy, the Thomas-Fermi profile is generally a good approximation [12] to the true ground state. Alternatively, we may use a simple numerical algorithm called imaginary time propagation to efficiently compute the ground state. Consider a state expressed in the eigenstate basis of the cold-atom Hamiltonian, i.e $\Psi(\boldsymbol{x}) = \sum_n c_n \Phi_n(\boldsymbol{x})$. If we rotate into imaginary time: $t \to i\tau$, Hamiltonian evolution now looks like the following:

$$\Psi(\boldsymbol{x}, \tau) = \sum_n \exp(-\epsilon_n c_n) \Phi_n(\boldsymbol{x}) \tag{5.7}$$

where ϵ_n is the eigenenergy of the n'th eigenstate. For a positive-definite Hamiltonian ($\epsilon_n > 0 \, \forall n$), all modes other than the ground state rapidly decay to zero. Hence, the ground state is obtained by evolving for a short duration in imaginary time, renormalising every timestep to prevent the norm decaying to zero.

5.2 The Stochastic Projected Gross-Pitaevskii Equation (SPGPE)

The Stochastic Projected Gross-Pitaevskii Equation (SPGPE) is a formalism to describe quantum dynamics of finite-temperature atomic ensembles [91, 94, 95]. The equations of motions are unravellings of the functional Wigner phase-space distribution, and the underlying master equation is derived from a microscopic theory of quantum system interacting with a thermal reservoir. The full theory realises a grand-canonical ensemble description for the quantum system, and consists of two energy regions:

- A C-field region[5] to describe behaviour of low-energy modes below a specified single-particle energy cutoff (ϵ_{cut}). At all times, the projector ($\mathcal{P}\{\star\}$) is used to ensure the field remains within the C-region. All modes below the cutoff have number occupation of order unity such that the presence of quantum fluctuations are less impactful, and so the bosonic field is well modeled using classical-field techniques [95].
- An I-field incoherent region consisting of all modes above the energy cutoff. This region acts as a thermal reservoir for the C-region, with whom it interacts through particle and energy exchange processes.

A complete description of the SPGPE is not only well beyond the scope of this thesis, but also entirely unnecessary. Hence, we briefly introduce the complete SPGPE and focus on the concepts we need; namely, the simple-growth SPGPE and the self-consistent projection process. For an excellent review of the SPGPE and C-field methods, refer to [49].

[4] The time-independent Schrodinger equation is an eigenvalue equation. However, the stationary GPE is *not*, as it is a self-consistent equation.

[5] Historically, the *C in* C-field has typically referred to classical or coherent fields.

5.2.1 The Complete SPGPE

The SPGPE only describes the dynamics of the quantum system restricted to the C-field region, which self-consistently guaranteed by the projector. Strictly, the energy cutoff (ϵ_{cut}) should be chosen such that modes near the cutoff have mean occupation[6] $\langle n \rangle \approx 1$. However, this is often not possible for reasons which we explain in Section 6.1, and it is often sufficient to choose $\epsilon_{\text{cut}} \approx 2 - 3\mu$, where μ is the chemical potential of the system at equilibrium [96]. In dimensionless form, the complete SPGPE may be decomposed into the sum of three terms:

$$(\mathbf{S})d\psi = d\psi|_H + d\psi|_\gamma + (\mathbf{S})d\psi|_\epsilon \tag{5.8}$$

where:

$$\begin{aligned} d\psi_H &= \mathcal{P}\{-i\mathcal{L}\psi dt\}, \\ d\psi_\gamma &= \mathcal{P}\{\gamma(\mu - \mathcal{L})\psi dt + dW_\gamma(\mathbf{r}, t)\} \\ (\mathbf{S})d\psi|_\epsilon &= \mathcal{P}\{-iV_\epsilon(\mathbf{r}, t)\psi dt + i\psi dU(\mathbf{r}, t)\} \end{aligned} \tag{5.9}$$

The first component ($d\psi_H$) is Hamiltonian evolution, while the remaining components are generally referred to as the *number-damping* ($d\psi_\gamma$) and *energy-damping* ($(\mathbf{S})d\psi|_\epsilon$) terms, respectively [97]. We will examine the various parameters shortly. Each term corresponds to a different physical process:

- Hamiltonian evolution ($d\psi_H$): This is simply evolution generated by the cold-atom Hamiltonian. The operator $\mathcal{L}$ is shorthand for $\mathcal{L}\psi = (H_{\text{sp}} + g|\psi|^2\psi)$, where H_{sp} is the single-particle harmonic oscillator Hamiltonian. By itself, it forms a micro-canonical description.
- Number damping ($d\psi_\gamma$): Describes the process where two particles in the thermal **I**-region scatter and ejects a low-energy particle into the C-field region. This process transfers both energy and particle (number), so it furnishes a grand-canonical description.
- Energy damping ($(\mathbf{S})d\psi|_\epsilon$): Describes the scattering between a particle in the **I** and C-regions, transferring energy between the two regions but *not* number. Hence, it realises a canonical description.

The complete SPGPE evolves arbitrary initial states to samples of thermal equilibrium. We may choose the number of particles in the ensemble by specifying the temperature (T) and chemical potential (μ). The 'growth rate' (γ) in the number-damping term controls how quickly states evolve to equilibrium, while the energy damping term is required for investigations of dynamics far from equilibrium. The energy-damping term is also numerically challenging to implement due to the multiplicative noise term[7]. As we simply wish to obtain samples of thermal equilibrium to serve as initial states for our feedback cooling simulations, it is sufficient to only simulate the Hamiltonian and number-damping terms[8]. In the literature, this is commonly referred to as the simple-growth SPGPE [94].

[6] As quantum fluctuations occupy on average half a quanta of energy per mode.

[7] Generally integrated with the weak-vector semi-implicit Euler algorithm, ;see [47].

[8] Simulations which omit *either* the number or energy damping terms will still approach thermal equilibrium, though this will be a canonical or grand canonical equilibrium, respectively. If the energy-damping term is omitted, the transient dynamics will be inaccurate, but this is irrelevant for our needs.

5.2.2 The Simple-Growth SPGPE

If the energy-damping term is omitted, we are left with the simple-growth SPGPE:

$$\begin{aligned} d\psi|_{H+\gamma} &= d\psi_H + d\psi_\gamma \\ &= -i\mathcal{P}\{(\mathcal{L}-\mu)\psi dt\} \\ &+ \mathcal{P}\{\gamma(\mu-\mathcal{L})\psi dt + dW_\gamma(\boldsymbol{x},t)\} \end{aligned} \tag{5.10}$$

where γ is the growth rate, and $dW_\gamma(\boldsymbol{x},t)$ is a complex Wiener noise with mean correlations:

$$\langle dW_\gamma^*(\boldsymbol{x},t)dW_\gamma(\boldsymbol{x}',t)\rangle = 2\gamma\tilde{T}\delta_C(\boldsymbol{x},\boldsymbol{x}')dt \tag{5.11}$$

where:

$$\delta_{\mathbf{C}}(\boldsymbol{x},\boldsymbol{x}') = \sum_{n\in\mathbf{C}}\phi_n(\boldsymbol{x})\phi_n^*(\boldsymbol{x}') \tag{5.12}$$

is a delta function represented in the truncated Hermite-Gauss basis, and $\tilde{T} = k_BT/\hbar\omega_0$ is defined as the dimensionless temperature. In practice, it is often more efficient and numerically sample the growth noise in the spectral basis:

$$dW_\gamma(\boldsymbol{x},t) = \sum_n dU_{\gamma,n}\phi_n(\boldsymbol{x}), \qquad \text{where} \qquad \left\langle dU_{\gamma,n}^* dU_{\gamma,m}\right\rangle = 2\gamma\tilde{T}dt\delta_{nm} \tag{5.13}$$

For our purposes, the parameters $\tilde{T}$ and μ are effectively proxies for the particle number and condensate fraction at thermal equilibrium. Hence, we vary them until we obtain the desired thermal state.

5.3 Successful Cooling from an Incoherent Thermal State

This section contain preliminary results which demonstrate successful cooling of a thermal state in quasi-1D geometries. We note that the parameters we use are not reflective of a real experiment. This is primarily due to fact that the reduction of thermodynamic quantities such as the chemical potential from 3D into 1D theory is not necessarily well defined [91], even if the system satisfies all the conditions for dimensional reduction such as extremely tight trapping in the reduced dimensions. Nevertheless, the primary goal of our simulations is to capture the phase transition between an incoherent mixture to condensed mode under the presence of feedback and effects of measurement backaction. As T and μ are only varied to obtain different initial states, their values should affect subsequent dynamics of feedback. Simulations of the simple-growth SPGPE are performed in the spectral basis, while simulations of feedback cooling use the discrete position basis[9].

5.3.1 An Example of the Measurement Process

The atomic density at different points of the measurement process is shown below in Fig. 5.1. in both 1D and 2D geometries.

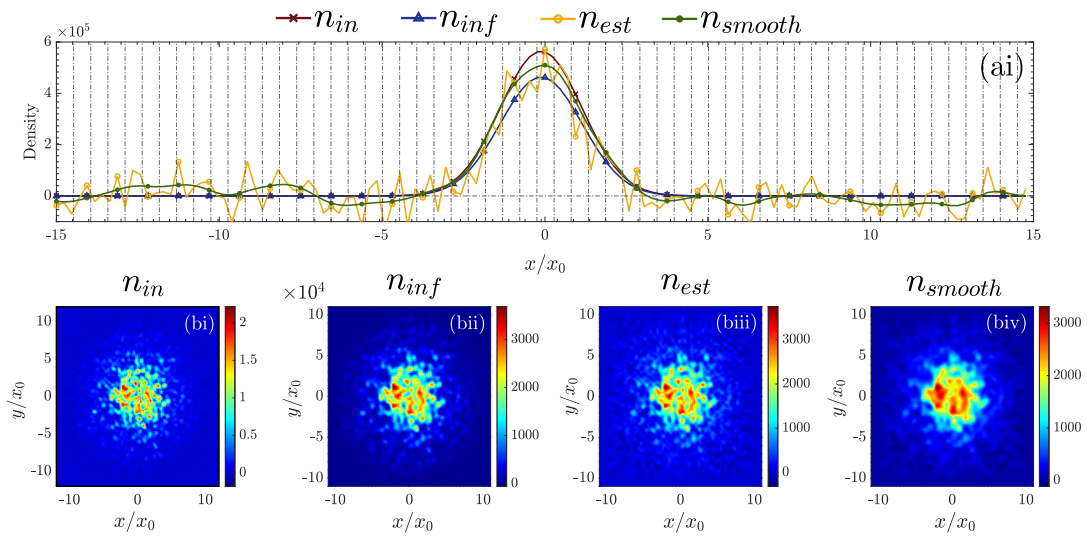

Figure 5.1: Plots of the atomic density profile at different stages of the measurement process in both 1D (*ai*) and 2D (*bi*)-(*biv*) geometries. A Gaussian state, and a single sample of a thermal state were used in the 1D and 2D cases, respectively. In both cases, the real atomic density is denoted n_{in}, the diffraction limited inferred density as n_{inf}, the noisy density estimate as n_{est}, and the final density estimate which has been smoothed due to the finite resolution of the PCI apparatus, which we set as equal to the diffraction limit) as n_{smooth}. In the 1D case (*ai*), increments of the detector resolution have been plotted with dashed vertical lines.

As expected, the blurring due to the diffraction of light as well as the finite PCI resolution primarily affects spatial modes with high frequency components in the the atomic

[9]We tried simulating feedback cooling in the spectral basis, but technicalities regarding both the projection of the measurement backaction as well as the implementation using XMDS meant that we were unable to do so in this thesis.

density[10]. By itself, we expect feedback cooling to be less effective for these modes. In practice, this is not a major limiting factor. as oscillations in these modes couple into lower frequency modes through interatomic scattering.

5.3.2 Initial State: SPGPE Thermal State

The density profile for a 1D thermal state obtained by evolving the Simple-Growth SPGPE to thermal equilibrium is plotted below in Fig. 5.2.

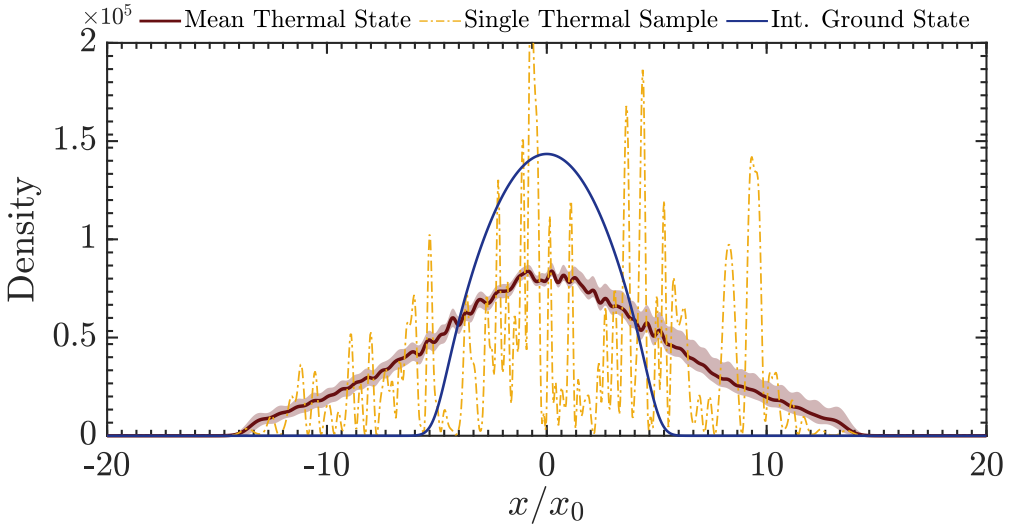

Figure 5.2: Density profiles of a thermal state obtained by evolving the Simple-Growth SPGPE to thermal equilibrium. The mean density, computed by averaging over an ensemble of 768 Wigner trajectories is plotted in red with bootstrapped 2σ- confidence intervals. The density corresponding to a single trajectory is plotted with a dashed yellow line, while the zero-temperature interacting ground-state is plotted in blue. We set the dimensionless chemical potential and temperature at equilibrium as $\mu = 5$ and $\tilde{T} = 400000$, respectively, leading to a condensate fraction of $f_{\text{frac}} = 4.4\%$ and particle number $N = 1.1 \times 10^6$.

As expected, the thermal state is significantly broader than the zero-temperature ground state. Note that when we simulate feedback cooling, initial states for individual Wigner trajectories are single samples of the mean thermal state; an example of such is plotted with a dashed yellow line. As thermodynamic quantities are ill-defined in 1D, we simply vary the temperature and chemical potential parameters at equilibrium until the thermal state has the desired particle number condensate fraction. In our simulations, these were $N = 1.1 \times 10^6$ and $f_{\text{frac}} = 4.4 \pm 0.2\%$, respectively. In addition, the choice of energy cutoff for projection is also ambiguous in 1D. However, existing studies have shown that a mode cutoff corresponding to $n = 100$ is generally a safe choice [10, 96].

We verified the implementation by repeating the simulation with different growth rates (γ) for initial states with different particle numbers. If implemented correctly, we should observe that the particle number and condensate fraction of the equilibrium state is independent of both the initial number (N) and growth rate (γ). This is indeed what

[10]Specifically, the components which have a high enough spatial frequency (k), such that $1/k$ is smaller than either the diffraction limit or PCI resolution.

we observe in Fig. 5.3 below, which illustrates the evolution of the particle number and condensate fraction at different growth rates, for initial states with different particles numbers ($N = 1.7 \times 10^6$ or $N = 7.0 \times 10^4$). For higher growth rates, both parameters approach a constant value (corresponding to thermal equilibrium) faster, as expected.

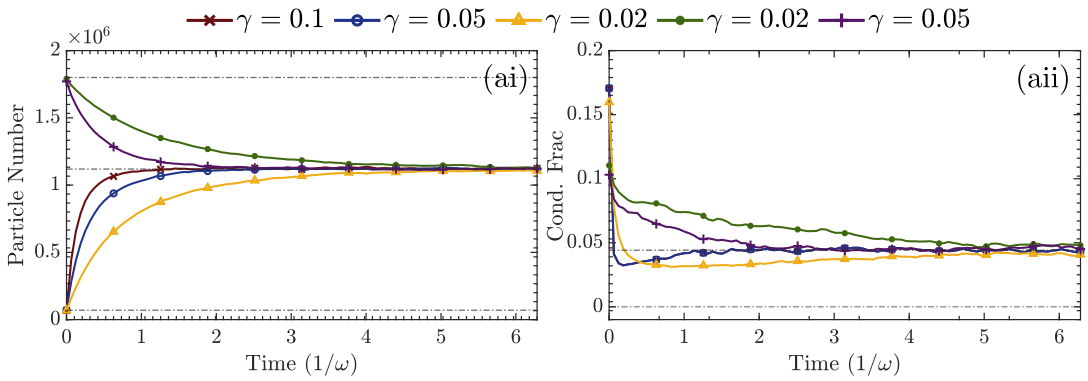

Figure 5.3: Evolution of the particle number and condensate fraction time for different initial states evolved to thermal equilibrium via the Simple-Growth SPGPE with different growth rates. Particle numbers (N) of the initial states were chosen as $N = 1.7 \times 10^6$ or $N = 7.0 \times 10^4$. The values of both parameters eventually converge (at equilibrium). The condensate fraction is computed from the OBDM using the definition provided in Section 3.7.

5.3.3 Results: Comparisons of the Initial and Final States

Finally, we are ready to investigate the application of feedback cooling to an atomic gas. We jump straight to the case of a finite-temperature thermal state, as the cooling of zero-temperature states has been extensively studied in prior work [2, 43]. We simulate feedback cooling of the same thermal state as shown in Fig. 5.2 (initial condensate fraction $f_{\text{cond}} = 4.4 \pm 0.2\%$) for a total of 768 Wigner trajectories under the equations of Section 4.4. We use the following experimental parameters:

$$\begin{array}{cccc} \lambda_{1D} = 7.4 \times 10^{-6} & R_z = 20.0\ \mu m & R_y = 50.0\ \mu m & l_y = 200\ \mu m \\ g = 0.0001 & N_{\text{meas}} = 35000 & k_{\text{fb}} = 5.0 \times 10^{-5} & N = 1.1 \times 10^6 \end{array} \quad (5.14)$$

The density profiles of the initial and final atomic states are plotted in Fig. 5.4, where we observe that an initially incoherent thermal state is successfully cooled to a condensed mode after 40 trap cycles of cooling. Notably, the condensed mode is not the zero-temperature ground state, which was computed through using the imaginary time propagation algorithm of Section 5.1.4 and plotted in yellow. In principle, it is possible to determine the steady-state temperature by fitting the eigenvectors extracted from the OBDM. When represented in the spatial basis, its eigenvectors correspond to the atomic wavefunctions of the condensed and uncondensed modes. We did not perform this analysis, but note that this result suggests that our choice of measurement parameters may be sub-optimal. In (bi), we see that the density begins to slightly oscillate once the feedback is turned off as expected from a non-stationary state, while the development of phase coherence across the spatial extent of the atomic cloud as it is cooled is clearly visible in (ci).

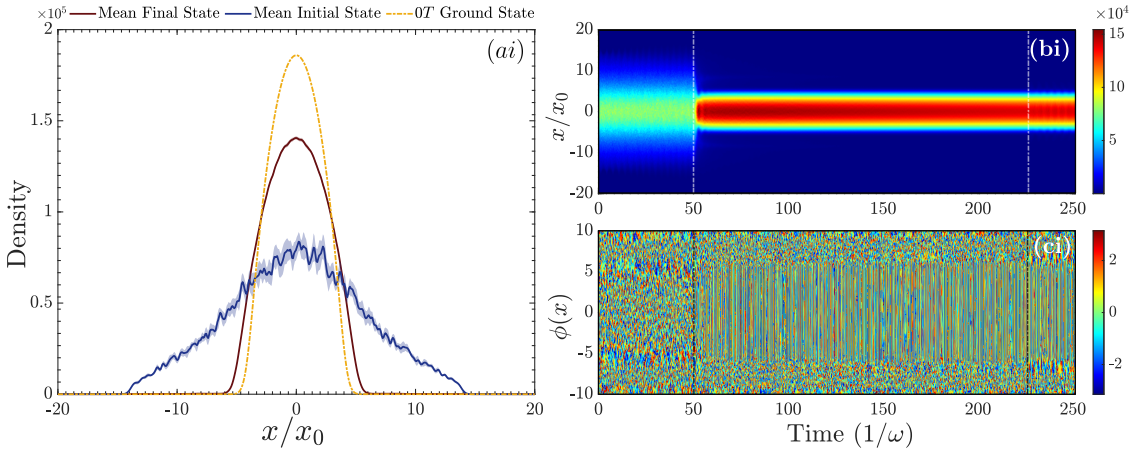

Figure 5.4: (ai) Plots of the initial and final atomic densities after feedback cooling. The initial state was an incoherent thermal state with condensate fraction $f_{\text{frac}} = 4.4 \pm 0.2\%$ and is plotted in blue. The steady-state after feedback cooling prior to turning of feedback is plotted in red, while the zero temperature ground state is plotted with a dashed line in yellow. Bootstrapped 2σ-confidence intervals are shaded for the initial and final states, though it is not visible for the latter. Both densities are unconditional, obtained from averaging over 384 Wigner trajectories. (bi) Time evolution of the mean atomic density. Feedback is turned on and off at the vertical lines. (bi) Time evolution of the mean phase across the spatial extent of the atomic state. Feedback is turned on and off at the vertical lines.

5.3.4 Results: Condensate Fraction and Steady State Energy

Finally, we look at the evolution of the condensate fraction and system energy, plotted in Fig. 5.5 below. We used the same parameters and initial thermal state as before, with the exception that feedback is no longer turned off prior to the end of the simulation.

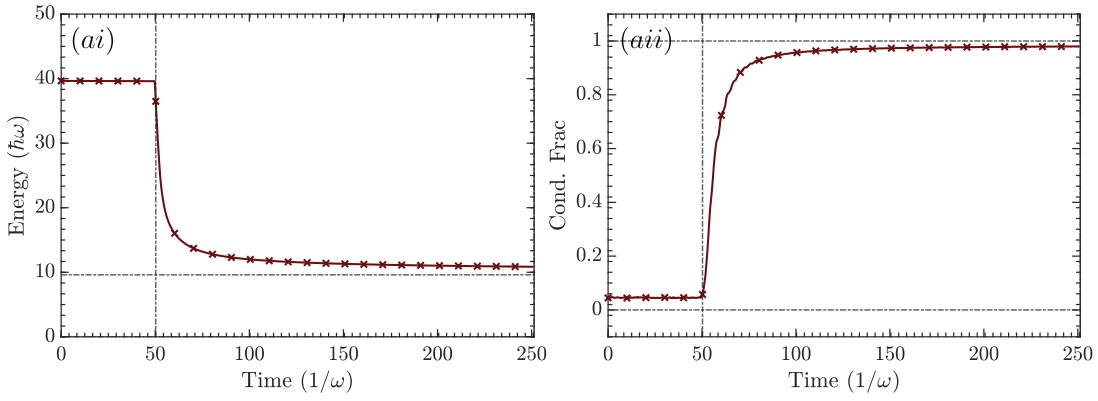

Figure 5.5: (ai) Time evolution of the system energy under feedback cooling. The dashed horizontal line represents the energy of the zero-temperature ground state. (bi) Time evolution of the condensate fraction. In both cases, feedback is turned on at the time indicated by the dashed vertical line.

In (ai), we see that the energy of the system is rapidly reduced from its initial value upon the onset of feedback cooling. The steady state energy is slightly higher than that of the zero-temperature ground state, consistent with the density profiles observed in Fig.

5.4 (ai). In general, states with higher energy tend to be broader the increased energy corresponds to stronger interatomic repulsion. In (aii), we observe the growth of the condensate fraction from $f_{\text{frac}} = 4.4 \pm 0.2\%$ to $f_{\text{frac}} = 98.0 \pm 0.2\%$, signifying the formation of a highly pure BEC.

5.4 Chapter Summary

In this chapter, we have used our approach to successfully simulate of feedback cooling applied to a finite temperature (1D) thermal gas, and observed an increase in the condensate fraction from $f_{\text{frac}} = 4.4 \pm 0.2\%$ to $f_{\text{frac}} = 98.0 \pm 0.2\%$. This is the first instance where feedback cooling has been applied to finite-temperature states with low initial condensate fraction; unpublished work by Taylor *et al.* [27] modeled finite-temperature initial states with appreciable initial condensate fraction ($f_{\text{cond}} \approx 70\%$), while subsequent work by Goh. *et al.* was heavily restricted to small BECs ($N \approx 10^4$) and could not be scaled to greater particle numbers or higher dimensions [10]. Both studies used the NPW particle-filter, which is known to encounter serious numerical instabilities when attempting to model conditional dynamics of high-temperature states that populate a large number of low-occupation modes. These limitations emphasise the attractiveness of our method: By disregarding conditional dynamics, we are able to completely sidestep the insurmountable barrier posed by undersampling of conditional quantum states. As a result, our method offers a truly scalable analogue for simulation of conditioned quantum systems when *only* the unconditional dynamics are of interest[11].

With regards to the conclusions of our simulations, we were unable to generate initial states with near-zero condensate fraction, which is typically the case of experimentally realistic thermal gases [12]. However, we emphasise that this was **not** due to limitations of our approach, but rather a consequence of the dimensional reduction to 1D, which we discuss in the next chapter.

[11] Which is always the case for feedback cooling.

Chapter 6

Experimental Considerations, Outlook, and Conclusions

In Chapter 5, we presented preliminary simulations of feedback cooling applied to a finite-temperature atomic gas in 1D and observed successful cooling from an incoherent thermal state to a condensed mode. This chapters serves to discuss shortcomings of our results, propose avenues for further investigation, and provide a summary of the work done in this thesis. In Section 6.1, we discuss the fundamental restrictions imposed by the dimensional reduction 1D, which motivates the need for higher dimensional simulation. In Section 6.2, we explain the significance of incorporating the spontaneous emission process into our simulation, leading to a discussion on the optimisation of feedback parameters and experimental imperfections. Finally, we conclude in Section 6.4 with a summary of the work undertaken throughout this thesis.

6.1 Restrictions of Dimensional Reduction

In Section 5.3, we said that dimensional reduction to 1D leads to ambiguities in the choice of projection cutoff and thermodynamic quantities. We now take a closer look at these ambiguities. Firstly, recall that on average, quantum fluctuations contribute half a quantum of energy[1] per mode [49]. Hence, modes with mean occupancy $\langle n \rangle < 1$ are dominated by quantum fluctuations. In the formalism of the SPGPE, these modes are unable to be described by C-field methods, so the energy cutoff (ϵ_{cut}) is typically chosen such that at thermal equilibrium, modes near the cutoff give an average occupation of $\langle n \rangle \approx n_{\text{cut}}$, where $n_{\text{cut}} = 1 \sim 3$ [95, 96]. Inverting the Bose-Einstein distribution yields the following expression for ϵ_{cut}:

$$\epsilon_{\text{cut}} = \ln\left(1 + \frac{1}{n_{\text{cut}}}\right) k_B T + \mu \tag{6.1}$$

In practice, the choice of ϵ_{cut} may be verified by ensuring that no notable discrepancy is observed in repeated simulations which employ a slightly different cutoff in the vicinity of ϵ_{cut}. Strictly, the condition above applies primarily to 3D geometries: In 1D (and even 2D), the ϵ_{cut} that satisfies the condition is often unreasonably large. We illustrate this point by plotting the distribution of mode occupancies for the same 1D thermal state used in prior simulations, in Fig. 6.1 below.

[1] In TW, this is captured through the noise in the initial state sapling.

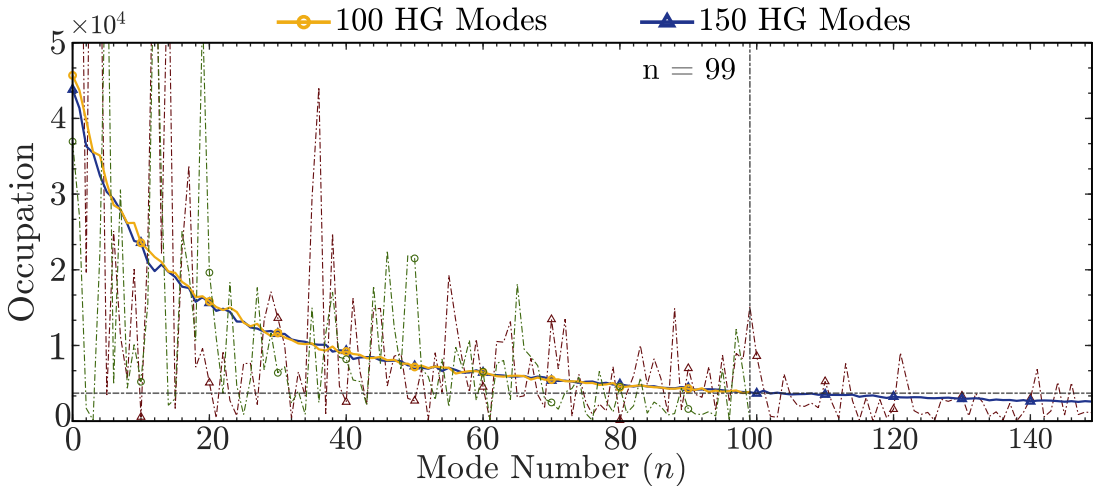

Figure 6.1: Occupation numbers of different Hermite-Gauss modes for a 1D thermal gas at thermal equilibrium, obtained by evolving the simple-growth SPGPE. Mean occupancies are given by an average over 1000 Wigner trajectories and are plotted with solid lines. The occupancy for a single Wigner trajectory is plotted with dashed lines. The horizontal line corresponds to 10% of occupation of the maximally populated $n = 0$.

Fig. 6.1 shows that the mode occupation decreases monotonically with mode number, which is an expected prediction of Boltzmann statistics [31]. At $n = 99$, the occupation is 10% of that for the maximally populated $n = 0$ mode. Past this point, the decrease in occupation becomes very slow. For example, in comparison to $n = 99$, the occupation of $n = 149$ has decreased by $\approx 4\%$. Following this trend, the condition of $\langle n \rangle \approx 1$ will only be satisfied for ridiculously large n.

This extremely gradual decay of the occupation is colloquially referred to as a 'long thermal tail', and is physically reflective of finite size effects, in the sense that the tail only approaches zero in the thermodynamic limit [98]. These effects are exacerbated in 1D (and 2D) geometries, as the dimensional reduction ultimately compresses thermodynamics of 3D into a lower dimensional subspace with less degrees of freedom; physically, one can envision a lower dimensional system embedded in a 3D thermal reservoir. The upshot is that we are unable to make comments or predictions about experimentally realistic 3D geometries solely from investigating dimensionally reduced quasi-1D and 2D systems [91]. Hence, simulations of feedback cooling must eventually be performed in 3D.

There are some technicalities associated with 3D simulation: Firstly, we would only be able to perform simulations in the spectral basis, as a position basis implementation would require an infeasibly large number of grid points to represent the full 3D state. As the measurement is performed in the spatial basis, the backaction applied to the atomic state would have to be projected onto the spectral basis. However, projecting the backaction onto the truncated spectral basis could lead to norm violation in the subsequent dynamics, and it is currently unclear to us whether manual renormalisation is the correct solution. Secondly, we are also unsure how measurement backaction looks in along the imaging axis, as our derivations of PCI in Section 4.2 only modeled the electric field operator within the imaging plane.

6.2 Effects of Spontaneous Emission and Parameter Dependence

Crucially, our simulations did not incorporate losses due to spontaneous emission, which is hypothesised to be the predominant factor in the efficacy of feedback cooling [86]. By incorporating spontaneous emission loss, we are able to investigate bounds on the final achievable condensate size and fraction[2].

In Section 3.7, we claimed that there exists sets of optimal feedback cooling parameters such that the backaction induced heating is efficiently suppressed by the cooling rate due to feedback. Hence, an investigation into the dependence of the final state energy and condensate fraction on the measurement parameters would provide valuable insight on how feedback cooling schemes may be optimised. For example, one possibility is dynamic feedback, where the measurement parameters are adjusted during the cooling procedure. As we saw in Section 5.3, both the position and momentum variances of the atomic state decrease during the cooling process. As a result, the timescale of density fluctuations increases as the steady state is approached, and it is plausible that sufficiently accurate derivative estimates could still be obtained with less frequent measurements. Similar logic could be applied to the gain parameter, in the sense that smaller density fluctuations could be damped out with weaker control potentials. The inclusion of spontaneous emission leads to more unknowns. For example: Is minimisiation of the spontaneous emission loss is a sufficient condition for achieving efficient feedback? How does its efficacy depend on the total particle number, which is an inherently dynamic parameter in the presence of spontaneous emission.

We note that our simulations did not account for the presence of time-lag in the control loop, which is an unavoidable experimental imperfection. However, this would be sufficiently simple to model, as we could simply offset the times at which the feedback potential is updated.

6.3 Conclusions

We have developed an alternative approach for the simulation of conditioned quantum systems built upon the existing phase-space simulation technique known as the Truncated Wigner Approximation [49]. In summary, our approach *only* captures unconditional dynamics, and a consequence of such is its excellent scalability to multi-mode systems. In Chapter 3, we investigated the validity of our method by modeling feedback cooling in a two-mode system, whose low-dimensionality permitted comparisons against an exact solution. Specifically, we modeled the two-mode analogue of feedback cooling through energy damping, and observed excellent agreement across multiple orders of pseudo-spin observables between the two methods. We discussed whether the success of our method generalises to multi-mode systems, and proposed ideas on how we could establish its correspondence with existing methods, such as the Number-Phase Wigner particle filter [60]. In Chapter 4, we derived the interaction Hamiltonian for phase-contrast imaging, and described the measurement process under the formalism of Quantum Non-Demolition measurements. In Chapter 5, we used our approach to model feedback cooling of a finite-temperature atomic gas in 1D, where we observed successful

[2]Of course, this is assuming a 3D simulation with experimentally realistic parameters.

cooling, characterised by the growth of the condensate fraction from $f_{\text{frac}} = 4.4 \pm 0.2\%$ to $f_{\text{frac}} = 98.0 \pm 0.2\%$ over a period of 40 trap cycles. To the best of our knowledge, this is the first instance in which feedback cooling of a finite-temperature atomic gas with low initial condensate fraction has been successfully modeled under a quantum-field description. Finally, we discussed how our results are inherently limited by the dimensional reduction to 1D, and identified potential technicalities in extending our simulations to 3D. We argued that the key priority of future investigations is to incorporate the effects of spontaneous emission loss into our simulations as it is the primary constraint on the efficacy of feedback cooling [86]. Luckily, no further modifications are required for implementing spontaneous emission, as the mechanism is built into our equations. Other avenues for future work were also suggested, such as investigating the dependence of the cooling efficacy on the feedback parameters, as well as dynamic extensions to the standard feedback cooling scheme of energy damping.

Our results mark a triumph in the continued effort of investigating feedback cooling as an alternative procedure for efficient production of large-scale BECs. On a broader level, we are optimistic that our approach will prove useful in other applications within the field of quantum control, where existing algorithms for numerical simulation of conditional quantum systems are often computationally expensive and unscalable to higher dimensional systems.

Bibliography

[1] J. Zhang, Y.-x. Liu, R.-B. Wu, K. Jacobs, and F. Nori, "Quantum feedback: theory, experiments, and applications", Physics Reports **679**, 1–60 (2017).

[2] M. R. Hush, S. S. Szigeti, A. R. R. Carvalho, and J. J. Hope, "Controlling spontaneous-emission noise in measurement-based feedback cooling of a Bose–Einstein condensate", New Journal of Physics **15**, 113060 (2013).

[3] J. Mehra and H. Rechenberg, *The Historical Development of Quantum Theory* ().

[4] M. H. Anderson, J. R. Ensher, M. R. Matthews, C. E. Wieman, and E. A. Cornell, "Observation of Bose-Einstein Condensation in a Dilute Atomic Vapor", Science **269**, 198–201 (1995).

[5] L. Pezzè, A. Smerzi, M. K. Oberthaler, R. Schmied, and P. Treutlein, "Quantum metrology with nonclassical states of atomic ensembles", Reviews of Modern Physics **90**, 035005 (2018), arXiv:1609.01609 [quant-ph].

[6] S. S. Szigeti, O. Hosten, and S. A. Haine, "Improving cold-atom sensors with quantum entanglement: Prospects and challenges", Applied Physics Letters **118**, 140501 (2021), arXiv:2010.09168 [cond-mat, physics:physics, physics:quant-ph].

[7] A. M. Rey, B. L. Hu, E. Calzetta, A. Roura, and C. W. Clark, "Nonequilibrium dynamics of optical-lattice-loaded Bose-Einstein-condensate atoms: Beyond the Hartree-Fock-Bogoliubov approximation", Physical Review A **69**, 033610 (2004).

[8] G. M. Tino, "Testing gravity with cold atom interferometry: results and prospects", Quantum Science and Technology **6**, 024014 (2021).

[9] S. S. Szigeti, S. J. Adlong, M. R. Hush, A. R. R. Carvalho, and J. J. Hope, "Robustness of system-filter separation for the feedback control of a quantum harmonic oscillator undergoing continuous position measurement", Physical Review A **87**, 013626 (2013).

[10] M. L. Goh, Z. Mehdi, R. L. Taylor, R. J. Thomas, A. S. Bradley, M. R. Hush, J. J. Hope, and S. S. Szigeti, *Feedback cooling Bose gases to quantum degeneracy*, 2022, arXiv:2206.05069 [cond-mat, physics:quant-ph].

[11] F. Dalfovo, S. Giorgini, L. P. Pitaevskii, and S. Stringari, "Theory of Bose-Einstein condensation in trapped gases", Reviews of Modern Physics **71**, 463–512 (1999).

[12] C. J. Pethick and H. Smith, *Bose–Einstein Condensation in Dilute Gases*, 2 edition (Cambridge University Press, Cambridge ; New York, 2008).

[13] W. Ketterle and N. J. V. Druten, "Evaporative Cooling of Trapped Atoms", in *Advances In Atomic, Molecular, and Optical Physics*, Vol. 37, edited by B. Bederson and H. Walther (Academic Press, 1996), pp. 181–236.

[14] V. Vuletić and S. Chu, "Laser Cooling of Atoms, Ions, or Molecules by Coherent Scattering", Physical Review Letters **84**, 3787–3790 (2000).

[15] K. Davis, M.-O. Mewes, and W. Ketterle, "An analytical model for evaporative cooling of atoms", Applied Physics B Laser and Optics **60**, 155–159 (1995).

[16] J. O. Andersen, "Theory of the weakly interacting Bose gas", Reviews of Modern Physics **76**, 599–639 (2004).

[17] P. B. Wigley, P. J. Everitt, A. van den Hengel, J. W. Bastian, M. A. Sooriyabandara, G. D. McDonald, K. S. Hardman, C. D. Quinlivan, et al., "Fast machine-learning online optimization of ultra-cold-atom experiments", Scientific Reports **6**, 25890 (2016).

[18] R. Combescot, M. Y. Kagan, and S. Stringari, "Collective mode of homogeneous superfluid Fermi gases in the BEC-BCS crossover", Physical Review A **74**, 042717 (2006).

[19] G. Gauthier, I. Lenton, N. M. Parry, M. Baker, M. J. Davis, H. Rubinsztein-Dunlop, and T. W. Neely, "Direct imaging of a digital-micromirror device for configurable microscopic optical potentials", Optica **3**, 1136–1143 (2016).

[20] G. Gauthier, T. A. Bell, A. B. Stilgoe, M. Baker, H. Rubinsztein-Dunlop, and T. W. Neely, "Dynamic high-resolution optical trapping of ultracold atoms", Advances in Atomic, Molecular and Optical Physics **70**, 1–101 (2021).

[21] M. R. Andrews, M.-O. Mewes, N. J. Van Druten, D. S. Durfee, D. M. Kurn, and W. Ketterle, "Direct, Nondestructive Observation of a Bose Condensate", Science **273**, 84–87 (1996).

[22] P. B. Wigley, P. J. Everitt, K. S. Hardman, M. R. Hush, C. H. Wei, M. A. Sooriyabandara, P. Manju, J. D. Close, et al., "Non-destructive shadowgraph imaging of ultra-cold atoms", Optics Letters **41**, 4795–4798 (2016).

[23] C. Brif, R. Chakrabarti, and H. Rabitz, "Control of quantum phenomena: past, present and future", New Journal of Physics **12**, 075008 (2010).

[24] P. Bushev, D. Rotter, A. Wilson, F. Dubin, C. Becher, J. Eschner, R. Blatt, V. Steixner, et al., "Feedback Cooling of a Single Trapped Ion", Physical Review Letters **96**, 043003 (2006).

[25] J. Guo, R. Norte, and S. Gröblacher, "Feedback Cooling of a Room Temperature Mechanical Oscillator close to its Motional Ground State", Physical Review Letters **123**, 223602 (2019).

[26] S. A. Haine, A. J. Ferris, J. D. Close, and J. J. Hope, "Control of an atom laser using feedback", Physical Review A: Atomic, Molecular, and Optical Physics **69**, 013605 (2004).

[27] R. Taylor, "Applications of quantum control: scaling of quantum computers and BEC-based quantum sensors", `10.25911/MWX0-XM85` (2021).

[28] M. Gajdacz, A. J. Hilliard, M. A. Kristensen, P. L. Pedersen, C. Klempt, J. J. Arlt, and J. F. Sherson, "Preparation of Ultracold Atom Clouds at the Shot Noise Level", Physical Review Letters **117**, 073604 (2016).

[29] M. E. Peskin and D. V. Schroeder, *An Introduction To Quantum Field Theory* (Avalon Publishing, 1995).

[30] W. Pauli, "Über den Zusammenhang des Abschlusses der Elektronengruppen im Atom mit der Komplexstruktur der Spektren", Zeitschrift für Physik **31**, 765–783 (1925).

[31] K. Huang, *STATISTICAL MECHANICS, 2ND ED* (2008).

[32] W. Hofstetter, J. I. Cirac, P. Zoller, E. Demler, and M. D. Lukin, "High-Temperature Superfluidity of Fermionic Atoms in Optical Lattices", Physical Review Letters **89**, 220407 (2002).

[33] Bose, "Plancks Gesetz und Lichtquantenhypothese", Zeitschrift fur Physik **26**, 178–181 (1924).

[34] E. Merzbacher, *Quantum Mechanics* (Jones & Bartlett Publishers, 1961).

[35] M. Egorov, B. Opanchuk, P. Drummond, B. V. Hall, P. Hannaford, and A. I. Sidorov, "Measurement of s-wave scattering lengths in a two-component Bose-Einstein condensate", Physical Review A **87**, 053614 (2013).

[36] E. P. Gross, "Structure of a quantized vortex in boson systems", Nuovo Cimento **20**, 454–477 (1961).

[37] M. R. Andrews, C. G. Townsend, H.-J. Miesner, D. S. Durfee, D. M. Kurn, and W. Ketterle, "Observation of Interference Between Two Bose Condensates", Science **275**, 637–641 (1997).

[38] A. Smerzi, S. Fantoni, S. Giovanazzi, and S. R. Shenoy, "Quantum Coherent Atomic Tunneling between Two Trapped Bose-Einstein Condensates", Physical Review Letters **79**, 4950–4953 (1997).

[39] R. Dum, J. I. Cirac, M. Lewenstein, and P. Zoller, "Creation of Dark Solitons and Vortices in Bose-Einstein Condensates", Physical Review Letters **80**, 2972–2975 (1998).

[40] K.-P. Marzlin, W. Zhang, and E. M. Wright, "Vortex Coupler for Atomic Bose-Einstein Condensates", Physical Review Letters **79**, 4728–4731 (1997).

[41] H. Bruus and K. Flensberg, *Many-Body Quantum Theory in Condensed Matter Physics: An Introduction* (OUP Oxford, 2004).

[42] H. M. Wiseman and G. J. Milburn, *Quantum Measurement and Control* (Cambridge University Press, Cambridge, 2009).

[43] S. S. Szigeti, M. R. Hush, A. R. R. Carvalho, and J. J. Hope, "Continuous measurement feedback control of a Bose-Einstein condensate using phase-contrast imaging", Physical Review A: Atomic, Molecular, and Optical Physics **80**, 013614 (2009).

[44] C. W. Gardiner and P. Zoller, *Quantum noise*, Springer Series in Synergetics (Springer, Berlin, Germany, 2010).

[45] H.-P. Breuer and F. Petruccione, *The Theory of Open Quantum Systems* (Oxford University Press, 2002).

[46] G. Lindblad, "On the generators of quantum dynamical semigroups", Communications in Mathematical Physics **48**, 119–130 (1976).

[47] C. W. Gardiner, *Handbook of Stochastic Methods for Physics, Chemistry, and the Natural Sciences* (Springer-Verlag, 1985).

[48] E. Wigner, "On the Quantum Correction For Thermodynamic Equilibrium", Physical Review **40**, 749–759 (1932).

[49] P. Blakie†, A. Bradley†, M. Davis, R. Ballagh, and C.W. Gardiner, "Dynamics and statistical mechanics of ultra-cold Bose gases using c-field techniques", Advances in Physics **57**, 363–455 (2008), eprint: `https://doi.org/10.1080/00018730802564254`.

[50] H.-W. Lee, "Theory and application of the quantum phase-space distribution functions", Physics Reports **259**, 147–211 (1995).

[51] R. P. Rundle and M. J. Everitt, "Overview of the Phase Space Formulation of Quantum Mechanics with Application to Quantum Technologies", Advanced Quantum Technologies **4**, 2100016 (2021).

[52] P. Deuar and P. Drummond, "Gauge P-representations for quantum-dynamical problems: Removal of boundary terms", Physical Review A **66**, 10.1103/PhysRevA.66.033812 (2002).

[53] A. Gilchrist, C. W. Gardiner, and P. D. Drummond, "Positive P representation: Application and validity", Physical Review A **55**, 3014–3032 (1997).

[54] A. Sinatra, C. Lobo, and Y. Castin, "The truncated Wigner method for Bose-condensed gases: limits of validity and applications1", Journal of Physics B: Atomic, Molecular and Optical Physics **35**, 3599 (2002).

[55] A. Polkovnikov, "Phase space representation of quantum dynamics", Annals of Physics **325**, 1790–1852 (2010), arXiv:0905.3384 [cond-mat, physics:hep-th, physics:quant-ph].

[56] A. Mandilara, E. Karpov, and N. J. Cerf, "Extending Hudson's theorem to mixed quantum states", Physical Review A **79**, 062302 (2009).

[57] M. K. Olsen and A. S. Bradley, "Numerical representation of quantum states in the positive-P and Wigner representations", Optics Communications **282**, 3924–3929 (2009), arXiv:0906.3905 [cond-mat, physics:quant-ph].

[58] S. Nolan, "Non-classical states in ultra-cold atoms for robust, high precision metrology", 10.14264/uql.2018.793 (2018).

[59] M. R. Hush, A. R. R. Carvalho, and J. J. Hope, "Scalable quantum field simulations of conditioned systems", Physical Review A: Atomic, Molecular, and Optical Physics **80**, 013606 (2009).

[60] M. R. Hush, A. R. R. Carvalho, and J. J. Hope, "Number-phase Wigner representation for scalable stochastic simulations of controlled quantum systems", Physical Review A: Atomic, Molecular, and Optical Physics **85**, 023607 (2012).

[61] Kushner, "On the dynamical equations of conditional probability density functions, with applications to optimal stochastic control theory",

[62] M. Arulampalam, S. Maskell, N. Gordon, and T. Clapp, "A Tutorial on Particle Filters for Online Nonlinear/Non-Gaussian Bayesian Tracking", Signal Processing, IEEE Transactions on **50**, 174–188 (2002).

[63] F. Gustafsson, F. Gunnarsson, N. Bergman, U. Forssell, J. Jansson, R. Karlsson, and P.-J. Nordlund, "Particle filters for positioning, navigation, and tracking", IEEE Transactions on Signal Processing **50**, 425–437 (2002).

[64] M. R. Hush, "Efficient simulation of controlled large quantum systems", 10.25911/5d514d3164727 (2012).

[65] R. L. Stratonovich, "Conditional Markov Processes", Theory of Probability & Its Applications **5**, 156–178 (1960).

[66] K. Jacobs, "Wave-function Monte Carlo method for simulating conditional master equations", Physical Review A **81**, 042106 (2010).

[67] T. A. Brun and H.-S. Goan, "Realistic simulations of single-spin nondemolition measurement by magnetic resonance force microscopy", Physical Review A **68**, 032301 (2003).

[68] G. Kitagawa, "Monte Carlo Filter and Smoother for Non-Gaussian Nonlinear State Space Models", Journal of Computational and Graphical Statistics **5**, 1–25 (1996), JSTOR: 1390750.

[69] G. Lindblad, "On the generators of quantum dynamical semigroups", Communications in Mathematical Physics **48**, 119–130 (1976).

[70] B. Yurke, S. L. McCall, and J. R. Klauder, "SU(2) and SU(1,1) interferometers", Physical Review A **33**, 4033–4054 (1986).

[71] U. Chabaud, P.-E. Emeriau, and F. Grosshans, "Witnessing Wigner Negativity", Quantum **5**, 471 (2021), arXiv:2102.06193 [quant-ph].

[72] G. J. Milburn, J. Corney, E. M. Wright, and D. F. Walls, "Quantum dynamics of an atomic Bose-Einstein condensate in a double-well potential", Physical Review A **55**, 4318–4324 (1997).

[73] K. W. Mahmud, H. Perry, and W. P. Reinhardt, "Quantum phase-space picture of Bose-Einstein condensates in a double well", Physical Review A **71**, 023615 (2005).

[74] D. Jaksch and P. Zoller, "The cold atom Hubbard toolbox", Annals of Physics **315**, 52–79 (2005), arXiv:cond-mat/0410614.

[75] A. Sinatra, C. Lobo, and Y. Castin, "The truncated Wigner method for Bose-condensed gases: limits of validity and applications1", Journal of Physics B: Atomic, Molecular and Optical Physics **35**, 3599 (2002).

[76] A. A. Norrie, R. J. Ballagh, and C. W. Gardiner, "Quantum turbulence and correlations in Bose-Einstein condensate collisions", Physical Review A **73**, 043617 (2006).

[77] L. Fuderer, J. J. Hope, and S. A. Haine, *A hybrid method of generating spin-squeezed states for quantum-enhanced atom interferometry*, https://arxiv.org/abs/2308.07693v1, 2023.

[78] M. Kritsotakis, J. A. Dunningham, and S. A. Haine, "Spin squeezing of a Bose-Einstein condensate via a quantum nondemolition measurement for quantum-enhanced atom interferometry", Physical Review A **103**, 023318 (2021).

[79] M. Kritsotakis, S. S. Szigeti, J. A. Dunningham, and S. A. Haine, "Optimal matter-wave gravimetry", Physical Review A **98**, 023629 (2018).

[80] H. M. Wiseman and G. J. Milburn, "Quantum-Theory of Optical Feedback Via Homodyne Detection", Physical Review Letters **70**, 548–551 (1993).

[81] D. Noll, D. Nishimura, and A. Macovski, "Homodyne detection in magnetic resonance imaging", IEEE Transactions on Medical Imaging **10**, 154–163 (1991).

[82] P. van der Straten and H. Metcalf, *Atoms and Molecules Interacting with Light: Atomic Physics for the Laser Era*, 1st edition (Cambridge University Press, Cambridge, 2016).

[83] H. M. Wiseman, "Using feedback to eliminate back-action in quantum measurements", Physical Review A **51**, 2459–2468 (1995).

[84] S. D. Wilson, A. R. R. Carvalho, J. J. Hope, and M. R. James, "Effects of measurement backaction in the stabilization of a Bose-Einstein condensate through feedback", Physical Review A **76**, 013610 (2007).

[85] O. Penrose and L. Onsager, "Bose-Einstein Condensation and Liquid Helium", Physical Review **104**, 576–584 (1956).

[86] Z. Mehdi, S. A. Haine, J. J. Hope, and S. S. Szigeti, *Fundamental Limits of Feedback Cooling Ultracold Atomic Gases*, 2023, arXiv:2306.09846 [cond-mat, physics:quant-ph].

[87] M. R. Andrews, M.-O. Mewes, N. J. van Druten, D. S. Durfee, D. M. Kurn, and W. Ketterle, "Direct, Nondestructive Observation of a Bose Condensate", Science **273**, 84–87 (1996), JSTOR: 2890049.

[88] S. S. Szigeti, "Controlled Bose-condensed sources for atom interferometry", 10.25911/5d514a57ce679 (2013).

[89] G. Gauthier, I. Lenton, N. M. Parry, M. Baker, M. J. Davis, H. Rubinsztein-Dunlop, and T. W. Neely, "Direct imaging of a digital-micromirror device for configurable microscopic optical potentials", Optica **3**, 1136–1143 (2016).

[90] J. J. Hope and J. D. Close, "Limit to Minimally Destructive Optical Detection of Atoms", Physical Review Letters **93**, 180402 (2004).

[91] A. S. Bradley, S. J. Rooney, and R. G. McDonald, "Low-dimensional stochastic projected Gross-Pitaevskii equation", Physical Review A **92**, 033631 (2015).

[92] G. R. Dennis, J. J. Hope, and M. T. Johnsson, "XMDS2: Fast, scalable simulation of coupled stochastic partial differential equations", Computer Physics Communications **184**, 201–208 (2013).

[93] F. B. Hildebrand, *Introduction to Numerical Analysis: Second Edition*, Second edition (Dover Publications, 2013).

[94] S. J. Rooney, P. B. Blakie, and A. S. Bradley, "Stochastic projected Gross-Pitaevskii equation", Physical Review A **86**, 053634 (2012).

[95] S. J. Rooney, P. B. Blakie, and A. S. Bradley, "Numerical method for the stochastic projected Gross-Pitaevskii equation", Physical Review E: Statistical Physics, Plasmas, Fluids, and Related Interdisciplinary Topics **89**, 013302 (2014).

[96] Z. Mehdi, A. Bradley, J. Hope, and S. Szigeti, "Superflow decay in a toroidal Bose gas: The effect of quantum and thermal fluctuations", SciPost Physics **11**, 080 (2021).

[97] R. G. McDonald, "Anomalous Dissipation in Bose Gases: Analytic Theory of Energy Damping", Thesis (University of Otago, 2019).

[98] W. J. Mullin, "Bose-Einstein condensation in a harmonic potential", Journal of Low Temperature Physics **106**, 615–641 (1997).